Doctoral Dissertation

Numerical study on the increase in lightning activity preceding downbursts using a meteorological model coupled with a bulk lightning model

雷を直接計算する気象モデルを用いたダウンバーストに先行する雷活動の激化に関する数値的研究

Makoto Kondo

近藤 誠

Division of Earth and Planetary Dynamics, Department of Natural History Sciences,

Graduate School of Science, Hokkaido University

北海道大学大学院理学院自然史科学専攻

地球惑星ダイナミクス講座

2025 年 3 月

Abstract

Mixed-phase clouds largely characterize severe weathers such as heavy rain, lightning, downbursts, and so on. They contain cloud microphysical processes involving both liquid and solid particles. In this doctoral dissertation, the mechanism for the increase in lightning activity preceding downbursts associated with mixed-phase clouds was investigated by using a meteorological model coupled with a bulk lightning model (BLM) that explicitly calculates lightning processes. The validity of cloud microphysics schemes in the model was also evaluated through comparison with in-situ ground-based measurement and satellite observation.

In Chapters 2 and 3, the evaluation of bulk cloud microphysics schemes used in the model was conducted through comparison with observational data. Three bulk microphysics schemes—two 1-moment bulk schemes that predict mass and diagnose number concentration of hydrometeors, and a 2-moment bulk scheme that predicts both mass and number concentration of hydrometeors—were evaluated through comparison with the observation data of a disdrometer measurement and Himawari-8 satellite. The evaluations were conducted for a snowfall event in Hokkaido. We here applied a newly developed method based on the machine learning algorithm to the data. The results of the evaluations clarified that the 2-moment bulk scheme better reproduced the particle size–fall velocity distribution observed by the disdrometer, in addition to the radiance and brightness temperatures retrieved from a satellite.

In Chapter 3, the evaluation for a 2-moment bulk scheme was extended to snowfall events during a winter season in Hokkaido. To analyze the measurement data for the whole winter, a method to automatically classify precipitation particle types was

developed with an aid of machine learning algorithms. The method was developed by applying self-organizing maps to the particle size–fall velocity relationship data, which were estimated using the expectation-maximization algorithm based on particle size–fall velocity distribution data measured by disdrometers. This novel approach enables the automatic classification of precipitation particles without any prior data, and additionally, the 2-moment bulk scheme was evaluated by utilizing this approach.

In Chapter 4, the rapid increase in lightning activity preceding the downbursts in multi-cell convective clouds was investigated using the 2-moment bulk scheme, which was validated in Chapters 2 and 3. The model successfully simulated the rapid increase in lightning activity preceding a downburst. Our analysis elucidated that the transition in the convective cells from tilting to upright under specific conditions of vertical wind shear and cold pool strength is critical for the occurrence of the rapid increase in the lightning activity.

The insights of this doctoral dissertation would contribute to deeply understanding of the dominant cloud microphysical processes in mixed-phase clouds that characterize the severe weathers. These insights are expected to improve the warning for downbursts and to sophisticate meteorological models. In the future, further understanding of mixed-phase clouds is anticipated through meteorological models and extensive observational data.

日本語要旨

混相雲は、豪雨、雷、ダウンバーストなどのシビア現象に大きく寄与し、その発達消滅といった成長プロセスは、液体および固体粒子の両方が関与する雲の微物理過程の影響を受けている。本博士論文では、混相雲によってもたらされるシビア現象の一つであるダウンバーストに先行する雷活動激化が発生するメカニズムを、雷過程を直接計算するバルク雷モデル（BLM）を結合した気象モデルを用いて調査した。また、モデル内の雲微物理スキームの妥当性を、地上観測データおよび衛星観測との比較を通じて評価した。第 2 章および第 3 章では、モデルで使用されているバルク雲微物理スキームの評価を実施した。この評価は、観測データとの比較を通して行うとともに、評価を実施するために機械学習に基づく地上観測データの解析手法を開発した。評価は 3 つのバルク微物理スキーム：水物質の質量を予報し、数濃度を診断する 2 つの 1 モーメントバルクスキームと、水物質の質量と数濃度の両方を予報する 2 モーメントバルクスキームに対して実施し、ディスドロメータ観測とひまわり 8 号による衛星の観測データとの比較を通して評価した。北海道における降雪事象を対象にした評価の結果、2 モーメントバルクスキームは、他の 2 つのスキームと比較して、ディスドロメータで観測された粒径-落下速度分布、ならびに放射輝度と輝度温度をより良く再現することを明らかにした。第 3 章では、2 モーメントバルクスキームの評価を、北海道における冬季の降雪事象全体に拡張した。冬季全体の観測データを解析するために、機械学習を活用して降水粒子の自動分類手法を開発した。この手法は、ディスドロメータで測定された粒径-落下速度分布データに、期待値最大化アルゴリズムを適用して推定し、推定された粒径-落下速度関係式に自己組織化マップを適用し、降水粒子の種類を分類する。この新しい手法より、先見情報なしに降水粒子の種類を自動で分類することが可能になった。この手法を用いて 2 モーメントバルクスキームの評価を行い、2 モーメントバルクスキームの妥当性を検証・確認した。第 4 章では、マルチセル対流雲におけるダウンバーストに先行する雷活動の急激な増加を、第 2 章および第 3 章で雲微物理スキームが評価された 2 モーメントバルクスキームを使用して調査した。具体的には理想化実験により、ダウンバーストに先行する雷活動の急激な増加を再現することに成功した。雷活動の急激な増加が発生するメカニズムを明らかにするために、雲の微物理特性と対流セルの傾斜に

焦点を当てた解析を行った。解析の結果から、特定の風の鉛直シアとコールドプール強度の条件下で対流セルが傾斜した対流から直立した対流に移行することが、ダウンバーストに先行する雷活動の急激な増加をもたらすメカニズムの一つであることを明らかにした。本博士論文で得られた知見は、シビア現象に寄与する混相雲における主要な雲微物理過程の理解を深めることに貢献する。さらにこれらの知見は、ダウンバーストに対する警報の精度向上および気象モデルの高度化に寄与すると期待される。将来的には、より広範な観測データを用いて評価された気象モデルを通じて、混相雲のさらなる理解が進むことが期待される。

Table of contents

Chapter 1. General Introduction

Clouds, which are composed of liquid water particles and/or ice particles, play an important role in Earth's energy balance and the water cycle. They are classified into three types as liquid-phase, ice-phase, and mixed-phase clouds according to the thermodynamic phase of these particles. Liquid-phase clouds consist solely of liquid particles, ice-phase clouds are composed only of ice particles, and the mixed-phase clouds contain both liquid and ice particles. The mixed-phase clouds are widely distributed from the tropics to the polar region (Zhang et al., 2010; Wang et al., 2013; Lawson and Getteman, 2014). Because the radiative properties of mixed-phase clouds vary with the liquid-to-ice ratio (Korolev et al., 2003), elucidating how liquid and solid particles are mixed within the cloud is especially essential to Earth's energy balance (Morrison et al., 2011).

The particles in liquid-phase, ice-phase, and mixed-phase clouds grow through various cloud microphysical processes (Pruppacher and Klet, 1997, Morrison et al., 2020). Mixed-phase clouds, as shown in Fig. 1.1, exhibit interactions between liquid and ice particles, such as riming growth through collisions between solid particles and supercooled water droplets (List, 1961; 2014). Riming significantly contributes to the growth of solid particles (Harimaya and Kanemura, 1995).

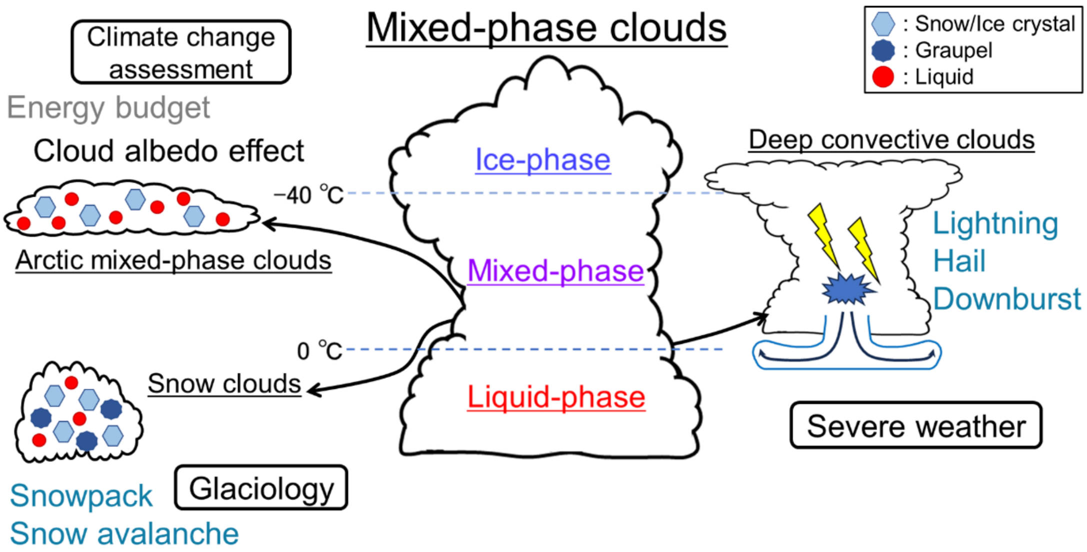

Fig. 1.1. A schematic diagram for mixed-phase clouds and their related phenomena.

Riming growth is active in mixed-phase convective clouds (Rutledge and Hobbs, 1984), and the high-density ice particles formed through riming largely affect the precipitation distribution due to their faster fall speeds compared to other ice particles (Magono et al., 1966; Woods et al., 2007). Additionally, these particles can grow beyond the size at which typical liquid particles would break up, and therefore, rimed particles contribute to heavy rainfall (Rutledge and Hobbs, 1984; Hou et al., 2016). As well as heavy rainfall, the high-density ice particles such as graupel and hail formed through riming growth can intensify downdrafts through drag force and latent heat cooling by melting and sublimation. The intensified downdrafts sometimes exceed 3.66 m/s at 91.4 m altitude categorized as downbursts (Fujita and Byers, 1977; Fujita, 1985; Wakimoto, 1985; Wilson et al., 1984; Hjelmfelt, 1988; Fujita, 1992; Wilson and Wakimoto, 2001), which causes damage to human society, such as power line failures, wind loads on structures, and aviation accidents (e.g., Abd-Elaal et al., 2018; Solari, 2020).

Mixed-phase clouds can also be characterized by hydrometeors with electric charge, i.e., electrified hydrometeors. It is considered that the charge separation occurs via collision processes of solid particles (Takahashi, 1978). Laboratory experiments have shown that collision and rebound between ice and graupel particles in mixed-phase clouds lead to charge separation called riming electrification mechanism (Takahashi, 1978; Saunders et al., 1991). Consistency of the riming electrification with charge distribution in convective clouds has been confirmed through previous studies by radiosonde and remote sensing observations (Takahashi et al., 1999, 2019; Rust, 1989; MacGorman and Rust, 1998). Thus, the riming electrification is considered a primary mechanism for charge separation in thunderstorms (Barthe et al., 2012; Phillips et al., 2020; Sato et al., 2019).

Because the riming growth and the riming electrification, which are distinctive microphysical processes that only occur in mixed-phase clouds, induce the occurrence of severe weather phenomena such as heavy rain, hailstorm, severe wind, downburst and lightning, these cloud microphysical processes characteristic of deep convective clouds that cause these severe weather events are important for the prevention of disasters. For disaster prevention, lightning activity has been focused on from 1990s by the observational studies. It has been reported that lightning activity rapidly increases preceding the occurrence of severe weather phenomena, such as heavy rain, hail, and downbursts (Goodman et al., 1988; Williams et al., 1999; Schultz et al., 2009, 2011). This rapid increase in lightning activity preceding severe weather is known as the lightning jump, and it has been utilized as an indicator of severe weather events (Schultz et al., 2009, 2011; Farnell and Rigo, 2020; Gatlin and Goodman, 2010, Erdmann and Poelman, 2023).

Although riming growth and charge separation can occur in updrafts of deep convective clouds, no lightning discharges are observed in areas with rimed particles (hail), known as "lightning holes." Additionally, several studies have shown that downbursts can occur without a lightning jump. For example, Jessup and Burke (2018) found that while lightning activity peaked before downbursts in 6 out of 11 cases, it did not always precede the event. These findings highlight the need for further research into the characteristics of mixed-phase areas, where riming growth and riming electrification are most active. Therefore, to advance our understanding of cloud microphysical processes such as riming growth and riming electrification, as well as the relationship between severe weather phenomena and lightning jumps, it is essential to elucidate the physical processes within mixed-phase clouds with lightning.

Many previous studies for understanding cloud microphysical processes in mixed-phase clouds have been conducted by various approaches such as observational, experimental, and numerical studies. To understand them, it is essential to analyze the area with the coexistence of liquid-phase and solid-phase particles and the cloud microphysical processes, across the entire mixed-phase cloud.

Observational studies can be classified into two approaches based on the methods employed: in-situ observations and remote-sensing observations. In-situ observations such as disdrometers (Matrosov et al., 2022) and sondes (Takahashi et al., 2019; Suzuki et al., 2023; Hara et al., 2024) allow for the direct observation of liquid and ice particles and enable the collection of physical quantities such as particle size, fall velocity, particle number, and shape with low uncertainty. However, capturing observations of the entire cloud and cloud microphysical process by the approaches remains challenging. Remote sensing observations using ground-based radar can classify and detect hydrometeors and measure particle size within clouds (Park et al., 2009; Dolan et al., 2013; Kouketsu et al., 2015; Kikuchi et al., 2020; Asai et al., 2021; Yoshimi et al., 2021). Additionally, radar observations combined with lightning observations have greatly contributed to the understanding of severe weather events and the occurrence of lightning jumps (e.g., Schultz et al., 2015; 2017). However, they cannot capture the coexistence of liquid-phase and solid-phase particles, which is essential for the characterization of mixed-phase clouds. Laboratory experiments by cloud chamber allow for relatively precise control of environmental conditions and enable the analysis of growth rates of cloud microphysical processes related to mixed-phase clouds (List, 1990; Oraltay and Hallett, 1989; Fukuta and Takahashi, 1999), However, because the cloud chamber size is limited and the residence time of particles is generally much shorter than that in real clouds (Chang et al. 2016; List et al.1986). In addition, the boundaries of the cloud chamber may influence the results. Thus, it is difficult to capture microphysical properties for the entire cloud by laboratory experiments.

In numerical studies, cloud microphysics schemes are based on the fundamental formulation and parameterization of cloud microphysical processes derived from observational, laboratory experimental, and theoretical studies (Morrison et al., 2020). Numerical simulation of mixed-phase clouds using cloud microphysics schemes allows the discussion of the coexistence of solid- and liquid-phase particles and the cloud microphysical processes in the mixed-phase area with dense three-dimensional information, which has been challenging in observational and laboratory experimental studies. Bulk lightning models can simulate lightning processes such as the charge separation processes based on riming electrification (Takahashi, 1978; Fierro et al., 2013). This allows for the analysis of updraft regions, where observations are challenging, and where riming growth and riming electrification are highly active. However, the cloud microphysics schemes commonly implemented in meteorological models rely on empirical assumptions, and have uncertainty, particularly in the representation of ice-phase cloud microphysical processes (Tapiador et al., 2019). Therefore, validation through comparison with observational data is required before we try to obtain the scientific knowledge according to the results of numerical simulations.

Cloud microphysics schemes have improved in accuracy through evaluations and improvements based on comparisons with observations (e.g., Roh and Satoh, 2014; Iguchi et al., 2012). For evaluation through comparison between observations and numerical simulation, the in-situ measurement data, which provides detailed information on individual particles, is beneficial. In particular, disdrometer data provide observations of particle size, fall velocity, and number concentration. These cloud microphysical information are key factors in determining particle characters related to cloud microphysical processes such as collision processes. The data are well-suited for evaluating cloud microphysics schemes (Molthan et al., 2016; Kondo et al., 2021). To utilize disdrometer data for evaluating mixed-phase cloud microphysical processes, observing high-density ice particles such as graupel growing through riming is required. Furthermore, extracting the characteristics of these observations focused on the riming process is essential in the evaluation.

For the model evaluation, it is necessary to observe rimed particles that are produced by riming growth. However, in tropical or summer convective clouds, even if rimed particles are produced, they tend to melt before reaching the ground. In such clouds capturing rimed particles is almost impossible by ground-based in-situ observations. Therefore, ground-based in-situ observations of rimed particles are feasible primarily during snowfall from mixed phase clouds events such as those in Hokkaido because the ground surface is below 0 °C and supercooled water particles can exist in clouds. Snowfall associated with boundary-layer convective clouds is driven by cold air outbreaks from Siberian air masses. Because it contains both graupel and snow particles, the snowfall events are suitable for the acquisition of mixed-phase cloud properties by disdrometer observations.

This doctoral dissertation aims to elucidate the mechanism of the increase in lightning activity preceding the downbursts by using a meteorological model coupled with a bulk lightning model that explicitly calculates lightning processes (Chapter 4). To evaluate the cloud microphysics scheme in the meteorological model, we compared the results of the model with observation data including disdrometer data (Chapter 2) for a single case. We also developed a method to extract mixed-phase cloud characteristics by classifying graupel and snow particles from size-fall velocity observation data to extend the evaluation for one winter season (Chapter 3). Chapter 5 provides a comprehensive summary of this doctoral dissertation.

Chapter 2. Evaluation of cloud microphysical schemes for winter snowfall events in Hokkaido: A case study of snowfall by winter monsoon

2.1. Introduction

Cloud covers broad areas of the Earth and plays important roles in its energy and water cycles. In mixed-phase and ice-phase clouds, a variety of solid particles are formed through microphysical processes such as deposition, aggregation, and riming, depending on the atmospheric conditions (Bailey and Hallett 2004; Kikuchi et al. 2013); thus, the cloud microphysical properties tend to be complex. The microphysics of solid particles are commonly characterized by mass–diameter (*m*-*D*) and terminal velocity–diameter (*v*-*D*) relationships, as well as the density and size distribution (Locatelli and Hobbs 1974; Mitchell 1996). The representation of the complex properties of solid hydrometeors in numerical models has been highly simplified in general (Tapiador et al. 2019) and remains as one of the major challenges in accurately representing mixed-phase and ice-phase clouds (Morrison et al. 2020).

Bulk microphysical schemes (e.g., Kessler 1969; Lin et al. 1983) are widely used to simulate cloud microphysics in global-scale models with explicit representation of cloud microphysics (Tomita et al. 2005; Satoh et al. 2014; Chern et al. 2016) and weather prediction models (Ferrier 1994, Morrison et al. 2005; Seifert and Beheng 2006; Saito et al. 2006; Thompson et al. 2008; Milbrandt et al. 2012). In these bulk microphysical schemes, *v*-*D* relationships are prescribed, although these relationships show large variability in the atmosphere (Locatelli and Hobbs 1974). As such, the prescribed *v*-*D* relationships are major factors in the uncertainty in cloud microphysical schemes, as reported in numerous studies (e.g., Woods et al. 2007; Iguchi et al. 2012).

This has prompted a number of studies that validated *v*, *D* and their relationships (i.e., *v*-*D* relationships) assumed by various models through comparisons with in situ observations by aircraft and ground-based measurements (e.g., Molthan and Colle 2012; Molthan et al. 2016). In particular, ground-based measurement by disdrometers such as the Particle Size Velocity disdrometer (PARSIVEL; Löffler-Mang and Joss 2000), the Laser Precipitation Monitor (LPM; Angulo-Martínez et al. 2018), and the two-dimensional video disdrometer (2DVD; Kruger and Krajewski 2002) have largely contributed to the evaluation of the *v*-*D* relationship of microphysical schemes. However, Katsuyama and Inatsu (2020) pointed out that the commonly used disdrometer introduces bias in the size–velocity distribution for solid precipitation measurements, that is rarely addressed, because the disdrometer does not observe the number concentration of precipitation particles directly. In addition, these disdrometers are usually expensive. Recently, Katsuyama and Inatsu (2021) developed a low-cost, portable volume scanning video disdrometer (VSVD) which can directly observe the number concentration, based on the work by Muramoto and Shiina (1989); the VSVD showed better performance in size–velocity observations than the conventional disdrometers. This implies that evaluations focusing on the *v*-*D* relationship using the results of the new disdrometer provide knowledge to improve cloud microphysical schemes.

Here, we evaluated bulk cloud microphysical schemes using measurement data from the new disdrometer targeting a snowfall event in Hokkaido, Japan, in an attempt to improve the representation of cloud microphysics schemes.

2.2. Data and Methods

2.2.1. Model

The meteorological model used in this study was Scalable Computing for Advanced Library and Environment (SCALE; Nishizawa et al. 2015; Sato et al. 2015) version 5.3.3. The two-moment bulk microphysical scheme of Seiki and Nakajima (2014; SN14), the one-moment bulk scheme of Tomita (2008; T08), and the improved version of one-moment bulk scheme of Roh and Satoh (2014; RS14) were used. In this study, we propose a one-moment bulk scheme based on RS14, with a modified *v-D* relationship and intercept parameter for the size distribution formed by graupel, as shown in Table 2.1. The modification of the *v-D* relationship assumes that *v* increases gradually with *D* compared to RS14. The reduction of the intercept parameter assumes that graupel is diagnosed as a low number concentration compared to RS14. The turbulence and radiation processes were calculated using the Mellor–Yamada Nakanishi–Niino level 2.5 scheme (Nakanishi and Niino 2004) and MSTRN-X (Sekiguchi and Nakajima 2008), respectively. The bucket land model and single-layer urban canopy model (Kusaka et al. 2001) were used for calculating temperature and soil moisture in non-urban and urban areas, respectively. The bulk coefficient of the surface flux was determined based on Beljaars and Holslag (1991) and Wilson (2001).

Table 2.1. Modification of the experimental parameters.

Parameter	**RS14 with modifications introduced in this study**	**RS14**
Intercept parameter of size distribution of graupel [m^{-4}]	4.0×10^6 (same value of T08)	4.0×10^8
v-D relationship of graupel	Lump graupel (Locatelli and Hobbs, 1974)	Graupel (Grabowski, 1998)
m-D relationship of graupel	Lump graupel (Locatelli and Hobbs, 1974)	Lump graupel (Locatelli and Hobbs, 1974)

2.2.2. Experimental setup

Simulations were conducted 33 hours from 0000 Coordinated Universal Time (UTC) on 12 February 2018, when snowfall occurred during a north-west winter monsoon over Hokkaido. The snowfall by the winter monsoon commonly occurs off the west coast of Japan including Hokkaido (Magono et al. 1966). Thus, the knowledge obtained from this case can be applied for most of the snowfall events in winter over Japan. The calculation domain covered an area of 900 × 900 km^2, with a grid interval of 1 km, as shown by the gray-shaded area in Fig. 2.1. The model top height was 19,528 m, and the model layer was divided into 57 layers. The layer thickness was increased from 40 m (at the model bottom) to 650.5 m (at the model top). The results of the model were output every 30 minutes. The pressure, horizontal wind field, temperature, specific humidity, mixing ratio of hydrometeors, soil moisture, and skin temperature of a 3-hourly Mesoscale ANLysis (MANL) provided by the Japan Meteorological Agency (JMA: JMA, 2019) were used for the initial and boundary conditions. RSTAR-7 (Nakajima and Tanaka 1986, 1988) implemented in Joint Simulator for Satellite Sensors (Joint-Simulator: Hashino et al. 2013) was used to calculate the 0.64 μm radiance and the 13.3-μm equivalent blackbody temperature (TBB) from the output of SCALE. For the calculation of Joint-Simulator, the information about the size distribution of the hydrometeor is required. The size distribution assumed in each scheme was also used in Joint-Simulator. For 1-moment schemes, the mono-disperse distributions with median diameter of 16 μm for cloud water and 80 μm for cloud ice were adopted.

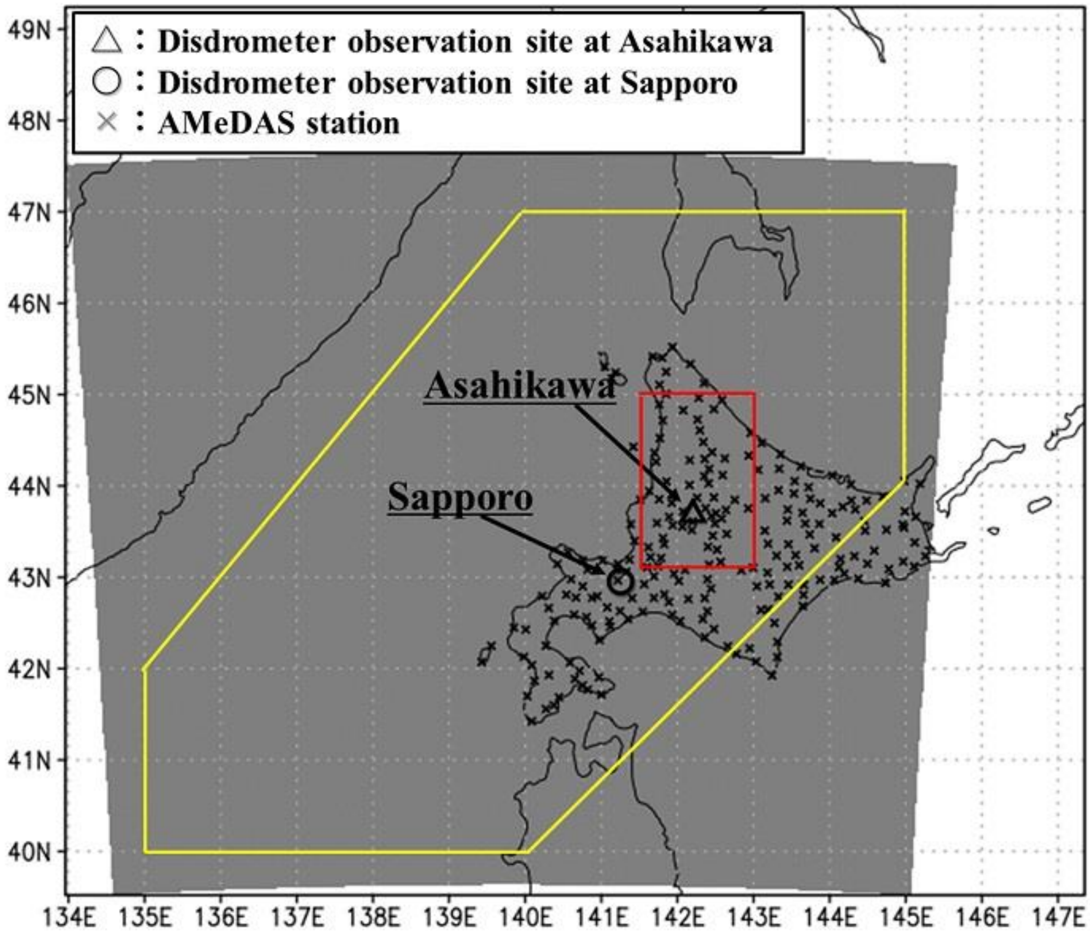

Fig. 2.1. Geographical map of the study's target area. Shading shows the domain for model calculations. Yellow and red box is the analysis area for the comparison with Himawari-8 satellite data and that of vertical mass profile among models, respectively. Cross marks denote the Automated Meteorological Data Acquisition System (AMeDAS) stations in Hokkaido operated by the Japan Meteorological Agency (JMA). Circles and triangles represent disdrometer observation sites at Sapporo and at Asahikawa installed by the authors, respectively.

2.2.3. Observational data

Observational data from the Himawari-8 geostationary satellite (Bessho et al. 2016; Yamamoto et al. 2020), Automated Meteorological Data Acquisition System (AMeDAS) operated by JMA, the radar/raingauge-analyzed precipitation product produced by Japan Meteorological Agency (JMA) (Makihara et al. 1996), and VSVDs

(Katsuyama and Inatsu, 2021) installed at Sapporo (43.0830° N, 141.3367° E, ○ point of Fig. 2.1) and Asahikawa (43.7870° N, 142.3465° E, △ point of Fig. 2.1) were used for the evaluation of the model. The 0.64 μm radiance and 13.3 μm TBB of Himawari-8 was used to confirm the validity of the horizontal cloud distribution and the cloud top height simulated by the model. The total amount of precipitation from 1500 UTC on 12 February to 0900 UTC on 13 February 2018 observed at 220 AMeDAS sites (shown as × points in Fig. 2.1) and radar/raingauge-analyzed precipitation were used to evaluate the simulated precipitation amount. Disdrometer data was used to evaluate the number of hydrometeor particles, particle size, and terminal velocity distribution (PSVD) from Asahikawa and Sapporo from 2100 UTC 12 to 0000 UTC 13 and from 1500 UTC 12 to 0930 UTC 13 February 2018, respectively.

2.2.4. Comparison of the microphysical properties between the model and observations

We compared the observed PSVD and the frequency of terminal velocity with those obtained from simulations accumulated over 3 × 3 grids around the nearest grid point to the observations in longitude–latitude grid space. The simulated data were from the same period as the measurement data.

To create PSVD from the model, mean D ($\overline{D}$) was calculated from the model as:

$$\overline{D} = \frac{\sum_{i=j_{0.5}}^{j_{6.0}} D_i \, n(D_i)}{N}, \tag{2.1}$$

$$N = \sum_{i=j_{0.5}}^{j_{6.0}} n(D_i), \tag{2.2}$$

where D_i and $n(D_i)$ are the diameter of the i-th bin in unit of mm, the particle number of

i-th bin. Using $\overline{D}$, mean v ($\bar{v}$) was calculated according to v-D relationship assumed in each scheme. The frequency distribution of v used for the evaluation is given by

$$f(v_k) = \frac{n(\overline{v_k})}{N}, \tag{2.3}$$

where $\overline{v_k}$, $f(v_k)$, and $n(v_k)$ are $\bar{v}$ of k-th bin, the frequency distribution of the k-th bin, and particle number in k-th bin. $j_{0.5}$ and $j_{6.0}$ are respectively the bin number of D of 0.5 mm and 6.0 mm, which is minimum and maximum value of the disdrometer measurement range approximately supported by VSVD. The width of bin for D and v was same as that of measurement; 0.5 mm and 0.2 m s^{-1}, respectively. $n(D_i)$ in the model was calculated based on the assumption of size distribution of hydrometeor's particles in each scheme. The sum of the number concentrations of snow and graupel was used as simulated $n(D_i)$, because only a few amounts of cloud ice were reached to ground due to its small v, and cloud water and rain were not simulated due to the low temperature near the ground. In contrast, the measured values were accumulated during the same time interval of the model output; 30 minutes.

2.3. Result

2.3.1. General characteristics of simulated snow clouds

First, we validated the simulation through comparisons of the radiance, TBB, and precipitation amount with those obtained by Himawari-8 and AMeDAS. Figs. 2.2a and 2.3a indicate the horizontal distribution of 0.64 μm radiance and 13.3 μm TBB by Himawari-8. Cloud streaks formed by the winter monsoon were observed over the Sea of

Japan and Hokkaido. The horizontal distribution of simulated 0.64 µm radiance and TBB indicated that the three schemes simulated the cloud streaks, regardless of the cloud microphysical scheme (Figs. 2.2b–d, 2.3b-d), although the cloud coverage differed among models. In addition, most of the bias values of simulated precipitation amount over AMeDAS sites were smaller than 0.5 mm, and the distribution of the surface precipitation simulated by the model was similar to that by radar/raingauge-analyzed precipitation product (Fig. 2.A1), regardless of the cloud microphysical scheme. These results show that the three schemes reasonably simulated snow clouds and surface precipitation generated by them during the winter monsoon over land.

The reasonable representations of the cloud streaks and precipitation prompted us to conduct detailed analyses about the differences in the microphysics among individual models. SN14 well reproduced the horizontal distribution of clouds and cloud top height, based on a comparison with the observed 0.64 µm radiance (Figs. 2.2a, b) and 13.3 µm TBB (Figs. 2.3a, b), respectively. By contrast, cloud coverage by T08 was smaller than that observed; therefore, the simulated radiance (TBB) by T08 was smaller (higher) than the observed radiance (Figs. 2.2c and 2.3c). These trends were also evident in the results of RS14 (Figs. 2.2d and 2.3d). Due to the underestimation of cloud coverage, T08 and RS14 showed a smaller radiance and a higher TBB than that of observations (Figs. 2.2f and 2.3f). These trends in the simulated radiance and TBB were also seen in outgoing solar radiation (OSR) and outgoing longwave radiation (OLR) respectively (Fig. A.2.2). As these results are calculated by the same dynamical core (SCALE), these differences originated mainly from the microphysics in the models. Next, we discuss the reason for the difference among the results of three microphysical schemes based on a comparison between the model and in situ measurements by the disdrometers.

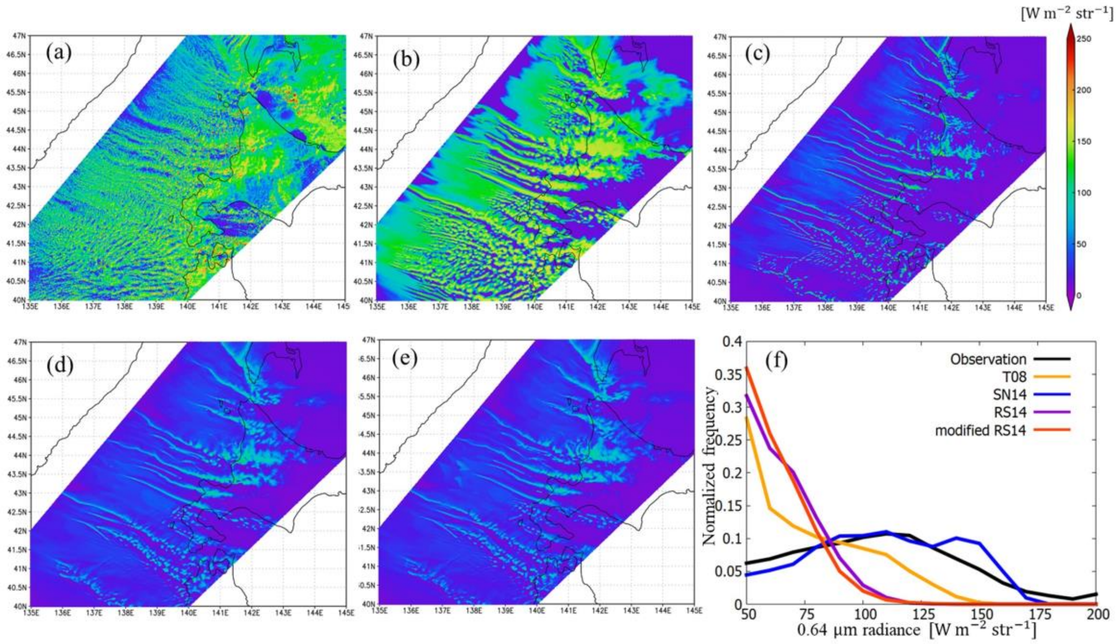

Fig. 2.2. (a) Radiance for a channel centered at 0.64 μm (W m^{-2} str^{-1}) at 0000 UTC on 13 February 2018 observed by the satellite Himawari-8, and (b–e) estimated by a Joint-Simulator from the outputs of Scalable Computing for Advanced Library and Environment experiments with cloud microphysics schemes of (b) SN14, (c) T08, (d) RS14 with a standard setting, and (e) RS14 with a modified velocity–particle diameter (*v*-*D*) relationship and intercept parameter for graupel. The area near the model lateral boundary was excluded from the analyses to avoid the artifacts. (f) The normalized frequency of the radiance data sampled from all gridpoints in yellow box in Fig. 2.1; radiance data were divided into 20 bins of uniform width from 10 to 200 W m^{-2} str^{-1}, which excluded less than 50 W m^{-2} str^{-1} shown in (black; a), (blue; b), (yellow; c), (purple; d) or (red; e).

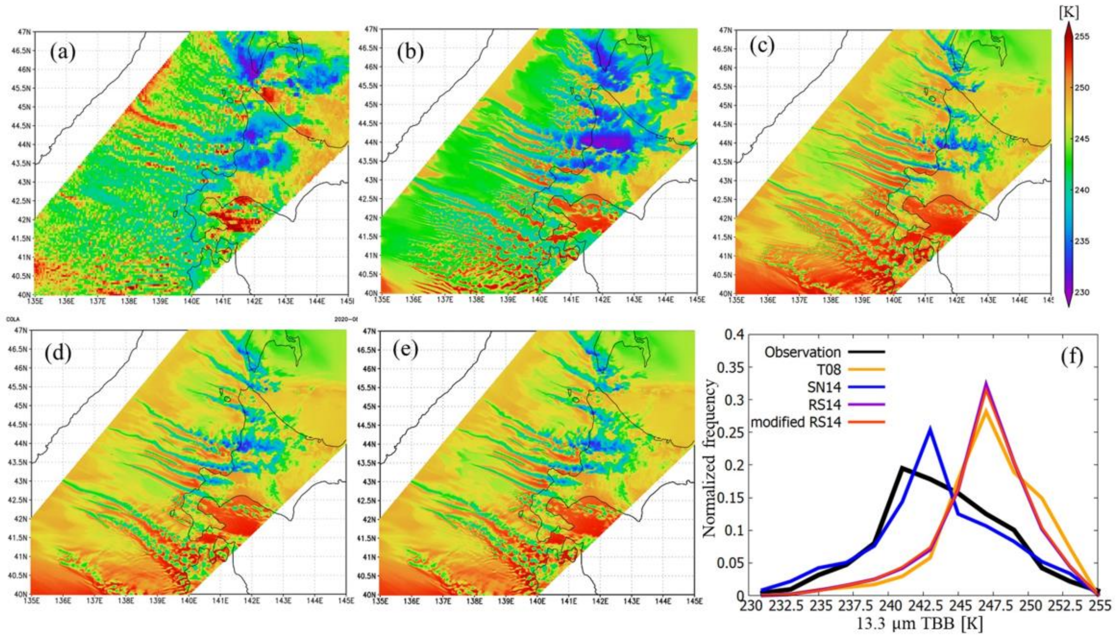

Fig. 2.3. (a–e) Same as Fig. 2.2, but for the equivalent blackbody temperature (TBB; unit is K) for a channel centered at 13.3 μm. (f) The normalized frequency of the TBB data sampled from all grid points in yellow box in Fig. 2.1. TBB data were divided into 20 bins of uniform width from 231 to 255 K, shown in (black; a), (blue; b), (yellow; c), (purple; d), or (red; e).

2.3.2. Microphysical properties

The observed PSVD and frequency of *v* observed by the disdrometers (Fig. 2.4) enabled further clarification of the microphysical properties. The *v* value of most of the measured particles was ~0.8 m s^{-1}, and the median *D* was ~1.5 mm. In addition, the black box plot was close to the dashed line and the observed PSVD was mainly distributed along the dashed line, which represents the *v*-*D* relationship of snow in Figs. 2.4a, 2.4c, and 2.4e (also Table 2.2). Thus, most of the measured particles here corresponded to snow in the model.

In SN14, the simulated PSVD was close to the observed PSVD, in which *v* was well reproduced (Fig. 2.4a). In addition, the frequency distribution of *v* indicated that snow was dominant at the surface (blue dotted line in Fig. 2.4b), similar to the results observed from in situ measurements (black line in Fig. 2.4b). Thus, SN14 reasonably simulated the *v*-*D* relationship of solid hydrometeors measured at the surface. As well as the surface, snow was dominant in the upper layer, based on the vertical profile of the mixing ratios of graupel (q_g), snow (q_s), and total hydrometeors (q_{hyd}), which corresponds to the sum of cloud water, rain, cloud ice, snow, and graupel, as shown in Fig. 2.5.

By contrast, the PSVD by T08 (Fig. 2.4c) indicated that *D* and *v* was underestimated and overestimated, respectively. The frequency distribution of T08 revealed a higher graupel frequency, in which *v* exceeded 3 m s^{-1} (red dotted line in Fig. 2.4d), although graupel was not measured. The reason of the higher frequency of the graupel was clarified in the conversion rate from snow to graupel by the accretion of snow by graupel ($P_{acc,s}$; blue line of Fig. 2.5e). $P_{acc,s}$ in T08 was larger than that of SN14. The large $P_{acc,s}$ in T08 resulted in the higher frequency of the graupel with fast terminal velocity, and overestimation of *v*. Due to the overestimation of *v*, hydrometeors in the atmosphere tended to fall faster to the ground by sedimentation (figure not shown); therefore, q_{hyd}, q_s, and q_g of T08 were smaller than those of SN14 (Figs. 2.5a-c). The small q_{hyd} resulted in the small cloud coverage of T08 (Figs. 2.2c and 2.3c).

The overestimation of *v* was reduced in the results of RS14 (Figs. 2.4e, f). The reduction of overestimated *v* was originated from the large interception parameter of RS14 (Table 2.1), which corresponds to the assumption that graupel has high number concentration, smaller size, and smaller *v*. In addition, as the RS14 turned off the accretion from snow to graupel (Roh and Satoh 2014), $P_{acc,s}$ was also reduced in RS14 (Fig. 2.5e). Due to the small $P_{acc,s}$, the vertical profiles of q_{hyd}, q_s, and q_g by RS14 were similar to those of SN14 (Figs. 2.5a-c), in which q_s was larger than q_g. However, the overestimation of v and the graupel frequency, and the underestimation of D, were not still improved using RS14 (Fig. 2.4f); the overestimations of v and the graupel frequency also suppressed the broadening of cloud coverage, as with T08 (Figs. 2.2d and 2.3d).

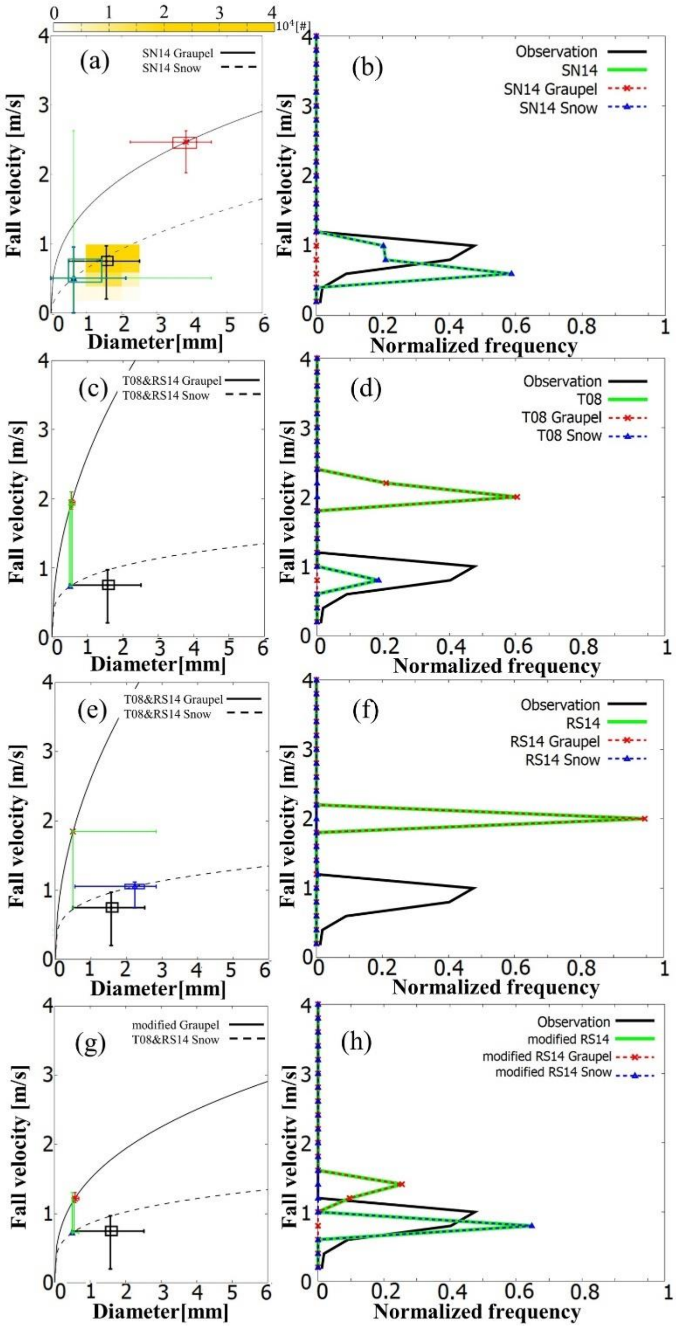

Fig. 2.4. (Left panels) Comparisons of particle size–velocity distribution (PSVD) between disdrometer observations and simulations with cloud microphysics schemes of (a) SN14, (c) T08, (e) standard RS14, or (g) modified RS14. The shaded area of (a) indicates the frequency of the observed PSVD and two-dimensional box-whisker plots indicate quartiles and the range between the 1–tile and 99–tile of the projected data onto (horizontal direction) diameter (mm) and (vertical direction) terminal velocity (m/s). The shaded area and black plot are based on all observed data by the disdrometer at Asahikawa and at Sapporo throughout the observation period; the blue plot is based on all simulated snow data at the nearest grid point to each observational site and eight grid points surrounding the nearest grid point. The red plot is based on all simulated graupel data. The green plot is based on sum of all simulated snow and graupel data. The solid and dashed lines represent the *v*-*D* relationships of graupel and snow, respectively, assumed in a cloud microphysics scheme. (Right panels) Comparison of normalized frequency between (black) disdrometer observations and (green) simulations with (b) SN14, (d) T08, (f) standard RS14 and (h) modified RS14. The simulated normalized frequency is separated into (blue dots) snow and (red dots) graupel. The *v* data was divided into 20 bins from 0 to 4 m s^{-1} using a uniform width.

2.3.3. Further improvement of RS14 based on in situ measurement results

To improve RS14 further, SN14, which showed good performance, was used as a reference value. Fig. 2.5b indicate that q_g profile of SN14 and RS14 was similar to each other, but the number concentration of graupel in RS14 was higher than that of SN14 (Fig. 2.5d). Based on the results, the high frequency and fast v of graupel had to be modified. For these modifications, the intercept parameter of the size distribution and the v-D relationship of graupel were changed as listed in Table 2.1. The modified RS14 simulated lower number concentration of graupel than that by RS14 (Fig. 2.5d). As a result, the overestimated frequency and fast v of graupel by RS14 were improved (Fig. 2.4h), although the cloud coverage remained small (Figs. 2.2e and 2.3e) and D was still underestimated (Fig. 2.4g). These results suggest that the assumptions pertaining to graupel, such as the intercept parameter and the v-D relationship, offer room for some variability. The cloud coverage was not improved by the modification of the graupel parameter (Figs. 2.2 and 2.3). For further improvement of the 1-moment scheme, the assumption of the size distribution of snow as well as graupel is required to be modified as we discussed in supplementary material (Fig. A.2.3 and Text A.2.1).

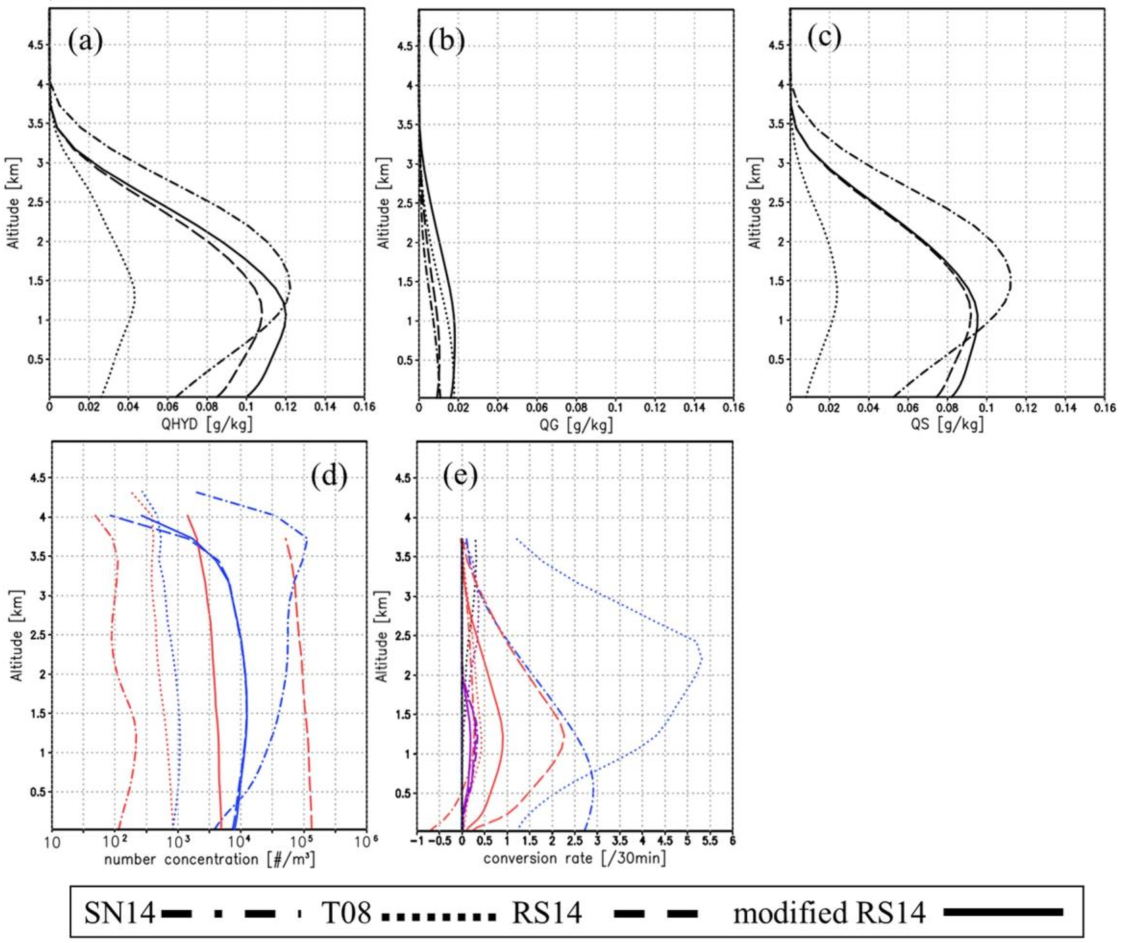

Fig. 2.5. Vertical profile of the mass mixing ratios of (a) total hydrometeors q_{hyd}, (b), graupel q_g, (c) snow q_s, (d) number concentration of graupel and snow, and (e) half-an-hourly conversion rate to graupel of unit q_g ($P_{acc,g}$) averaged over the domain enclosed by 141.518–143.007°E and 43.115–45.0071°N at 0000 UTC on Feb. 13, 2018. Dash-dotted, dotted, dash, and solid lines indicate the results of SN14, T08, standard RS14, and modified RS14, respectively. In (d), red and blue lines indicate number concentration of graupel and snow, respectively, and the number concentration was averaged over the grids in which mass mixing ratio of graupel and snow exceeded 10^{-5} g kg^{-1}. In (e), red, blue, black, and purple lines indicate conversion rate of unit graupel q_g by deposition of graupel, accretion of snow by graupel, that of cloud ice by graupel, and that of liquid hydrometeor by graupel.

2.4. Conclusion and Discussion

This study evaluated three microphysical schemes through a comparison with observations, including in situ measurements by the new disdrometer; VSVDs targeting snowfall events in Hokkaido, Japan. The comparison indicated that SN14 well-reproduced the characteristics of the observations. On the other hand, T08 overestimated v due to the overestimation of graupel. The overestimation of v was small in RS14 compared to that in T08. An experiment using RS14 with modifications indicated that the overestimation of graupel frequency was improved by changing the intercept parameter and the v-D relationship of graupel.

However, further improvements with respect to the underestimation of D and small cloud coverage are required, and we examined the problem by the RS14 scheme with considering the growth process of graupel. In general, graupel grows through the riming, the deposition, and the accretion of snow and cloud ice by graupel (Knight and Knight 1973; Harimaya 1976). Fig. 2.5e showed that the dominant process of graupel growth was different between RS14 and SN14. In SN14, the riming, the deposition, and the accretion of snow and cloud ice by graupel were all contributed as the graupel producing process. By contrast, RS14 represented only the two graupel-producing process; the riming (dashed purple line in Fig. 2.5e) and the deposition (dashed red line in Fig. 2.5e) by turning off the accretion of snow and cloud ice by graupel. Based on Harimaya (1976), who reported that the graupel contained snow by the accretion in winter Hokkaido, we imply that the accretion process is need to be included into the model. As well as the accretion, a more accurate representation of the growth process of graupel is required for simulating solid hydrometeors coexisting snow and graupel such as sea-effect snow cloud.

In Chapter 2, the evaluation was conducted based on a single case study. However, evaluating solid particles using disdrometer data from just one case is required for more comprehensive evaluation; thus, it is essential to extend the evaluation to an one winter season. Because expanding analyses of disdrometer data manually to cover the one winter season would be a highly time-consuming process, the analysis is a challenge for seasonal evaluation. To address this issue, the next chapter focuses on developing an evaluation method for precipitation particles using particle-size fall velocity data.

2.5.A. Appendix

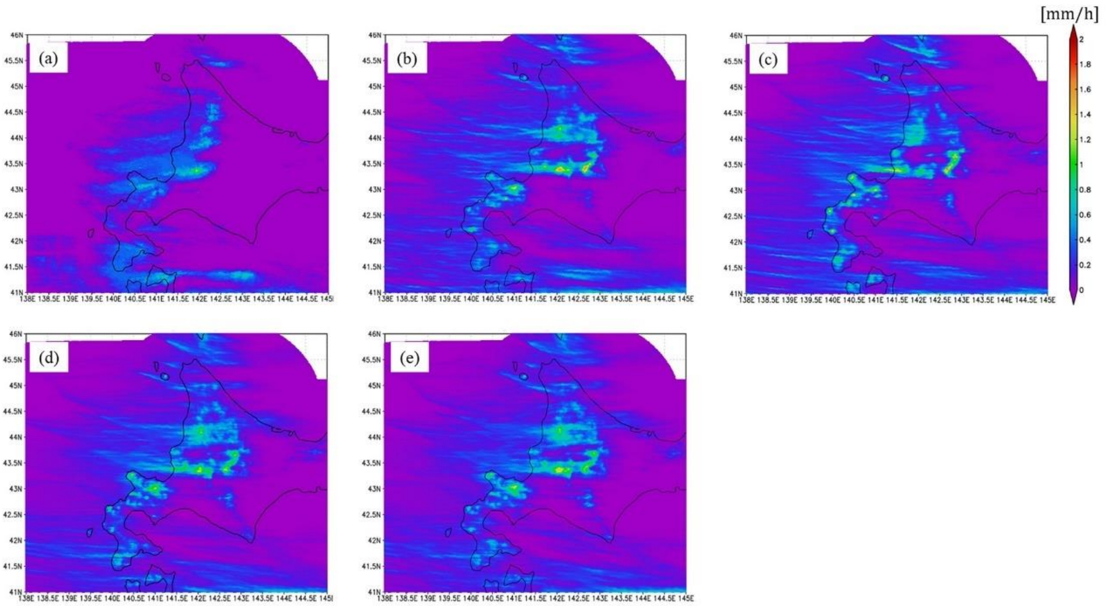

Fig. 2.A1. Geographical distribution of hourly averaged surface precipitation amount during 0000 to 0900 UTC on 13 February 2018 by (a) radar/raingauge-analyzed precipitation product produced by Japan Meteorological Agency (Makihara et al., 1996), and simulated by (b) SN14, (c) T08, (d) RS14, and (e) modified RS14.

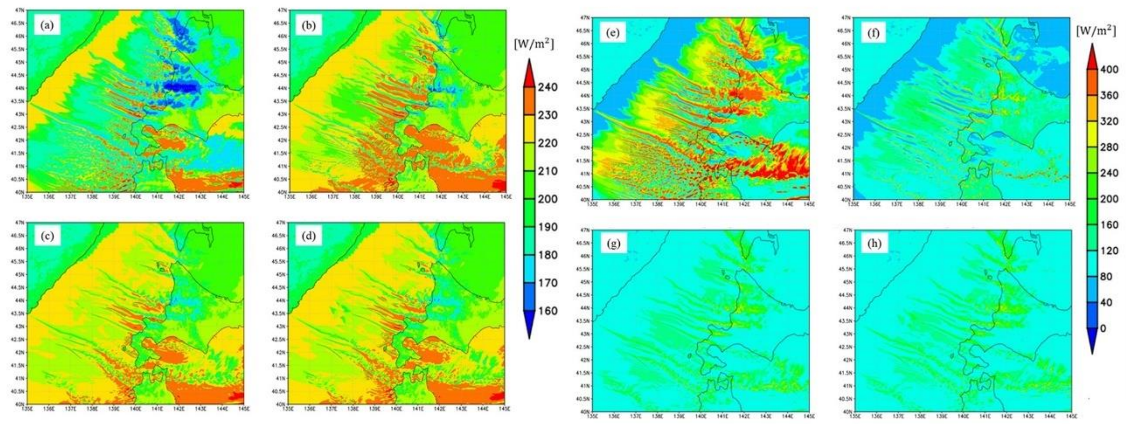

Fig. 2.A2. Geographical distribution of outgoing longwave radiation (OLR) in unit of W m^{-2} (a-d) and outgoing shortwave radiation (OSR) in unit of W m^{-2} (e-f) simulated by (a, e) SN14, (b, f) T08, (c, g) RS14, and (d, h) modified RS14.

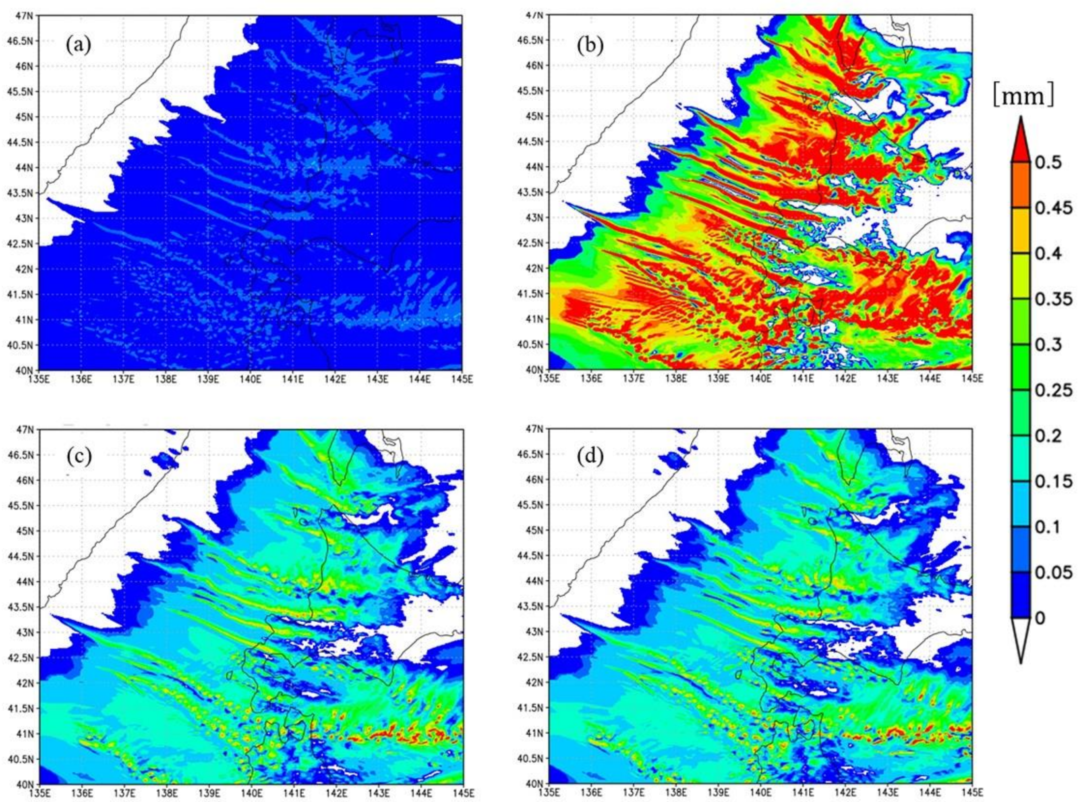

Fig. 2.A3. Geographical distribution of the effective radius of snow at the height of 1.5 km in unit of mm at 0000 UTC on 13 February 2018 simulated by (a) SN14, (b) T08, (c) RS14, and (d) modified RS14.

Text 2.A.1

Fig. 2A3 indicates that the effective radius of snow of 1-moment schemes was much larger than that of two-moment scheme (SN14). This trend was seen in another layer. This means that the size of snow assumed in the 1-moment schemes was larger than that of SN14. The large size of snow resulted in the underestimation of the radiance shown in Figs. 2.2c, 2.2d, and 2.2e. The large size of snow resulted in the fast conversion from snow to graupel and therefore, the small horizontal extent of hydrometeor shown in Figs. 2.3c, 2.3d, and 2.3e. Based on the results shown above, the modification of size distribution of snow is required, which is one of our future study.

Chapter 3. Development of an evaluation method for precipitation particle types by using disdrometer data (Kondo et al. 2024)

3.1. Introduction

Precipitation particles, especially solid precipitation particles, are formed through various microphysical processes such as deposition, aggregation, and riming, depending on the atmospheric conditions in clouds (Magono and Lee 1966; Bailey and Hallett 2004). The particles are classified as graupel, snow aggregates, ice crystals, and others (Kikuchi et al. 2013). Graupel is characterized by its round shape and relatively high density of 100–900 kg m^{-3} (Macklin 1962), whereas snow aggregates and ice crystals are characterized by their complex shape and low density of 10 – 150 kg m^{-3} (Heymsfield et al. 2002). Accurately capturing these microphysical properties is crucial for refining the assumptions made in meteorological models and remote sensing techniques. These microphysical properties affect the relationship between size and fall velocity, usually formulated as the power law of

$$v = aD^b, \tag{3.1}$$

where D and v are the diameter and fall velocity of precipitation particles, respectively, and a and b are coefficients (hereafter Eq. (3.1) is referred to as the v-D relationship). Locatelli and Hobbs (1974) determined a and b by best-fit curves derived from observation data of the diameter and fall velocity of solid precipitation particles. Their analysis indicated that a and b of snow aggregates show low fall velocity with a large diameter and those of graupel show high fall velocity, even with a small diameter. Long-term efforts were devoted to fitting observed or experimental data to the v-D relationship for each type of solid precipitation particles, and the results were summarized by Locatelli and Hobbs (1974). Mitchell (1996) calculated a and b theoretically and Mitchell and Heymsfield (2005) showed that a depends on the density of solid precipitation particles. The v-D relationships include the precipitation particle density, which depends on the particle type, such as snow aggregates or graupel. Hence, the established relationships may relate a set of size and fall velocity data to the solid precipitation particle types near the ground resulting from microphysical processes in clouds aloft.

A disdrometer is an instrument used to observe precipitation particles near the ground and is still widely used in solid precipitation measurements because the alternative approaches are unsuitable for conducting in situ observations over long periods at multiple locations; for example, in-cloud measurement by video sonde (Murakami and Matsuo 1990; Takahashi et al. 1995; Boussaton et al. 2004; Watanabe et al. 2014; Waugh et al. 2015; Suzuki et al. 2018) and aircraft (Bader et al. 1987; Iguchi et al. 2012; Murakami 2019) and remote sensing by dual-polarization radars (Hall et al. 1984; Marzano et al. 2008; Ribaud et al. 2016). The two-dimensional video disdrometer (2DVD; Kruger and Krajewski 2002), particle size velocity (PARSIVEL) disdrometer (Löffler-Mang and Joss 2000; Battaglia et al. 2010; Angulo-Martínez et al. 2018), laser precipitation monitor (LPM; Angulo-Martínez et al. 2018), multi-angle snowflake camera (Praz et al. 2017; Vignon et al. 2019), multiangle snowflake imager (Minda et al. 2017), and Precipitation Imaging Package (Pettersen 2020a,b, 2021) are widely used owing to their ability to observe the size and fall velocity of precipitation particles. Recently, Katsuyama and Inatsu (2021) developed a volume scanning video disdrometer (VSVD) that is more suitable for snowfall observations than the LPM or PARSIVEL because it can detect larger particle sizes.

The data observed by any disdrometer in a sampling time interval can be plotted in the two-dimensional space spanned by diameter and fall velocity. Several methods have been proposed for classifying precipitation particles based on these observations. Lee et al. (2015) developed a classification method based on the empirical v-D relationship, and Ishizaka et al. (2013) proposed the center of mass flux method. Moreover, supervised machine learning techniques, including the decision tree approach (Bernauer et al. 2016) and the support vector machine approach (Grazioli et al. 2014), have also been used for the classification. However, these methods require a reference dataset based on previous observations, manual labeling of the diameter-fall velocity observation data, or *a priori* coefficients based on the v-D relationship. Katsuyama and Inatsu (2020; KI20) developed a method using the expectation maximization (EM) algorithm to estimate the joint probability density function (PDF) of the diameter and fall velocity data that could even be applied to data for multiple precipitation types. In KI20, because the estimated PDF was based on v-D relationships without *a priori* information, precipitation types could be identified manually by referring to the established v-D relationships (Locatelli and Hobbs 1974, Mitchell 1996). However, it is practically impossible to perform manual identification for a massive amount of estimated v-D relationships from disdrometer data, and thus, an automated method is required.

In this study, we aim to develop a method for identifying types of precipitation particle based on particle size-fall velocity data. The particle size-fall velocity data are classified using the EM algorithm and a self-organizing map (SOM; Kohonen 1995;

Kohonen 2013). The SOM uses a neural network algorithm based on unsupervised learning to find generalized patterns in data, thereby reducing the dimensions of large datasets. As a result of SOM training, similar training data are grouped into each node using Euclidean distance and are organized into a two-dimensional array called an SOM map. SOM maps have also been used in climate research (Kawazoe et al. 2020; Nishiyama et al. 2007; Reusch et al. 2007) and predicting tornadic environments based on sounding data (Nowotarski and Jensen 2013). In contrast to other clustering techniques, SOM does not need *a priori* decisions about data distribution (e.g., the v-D relationship or type of precipitation particles); rather, it undergoes training during data processing (Kohonen 1995). As an application of the new method using the SOM map trained by EM algorithm results, we utilize the method to particle size-fall velocity data observed by the VSVD in Sapporo during the winter. The SOM map trained by EM algorithm using VSVD data is grouped into the graupel and snow aggregate categories to obtain the graupel-to-solid precipitation ratio (G/S ratio). The G/S ratio is compared with those obtained from meteorological models that assume graupel and snow aggregate categories to verify cloud microphysics schemes as an application of the product by the new method . In addition, the sensitivity of the results to the training data, SOM configuration, and the grouping of SOM nodes is also discussed.

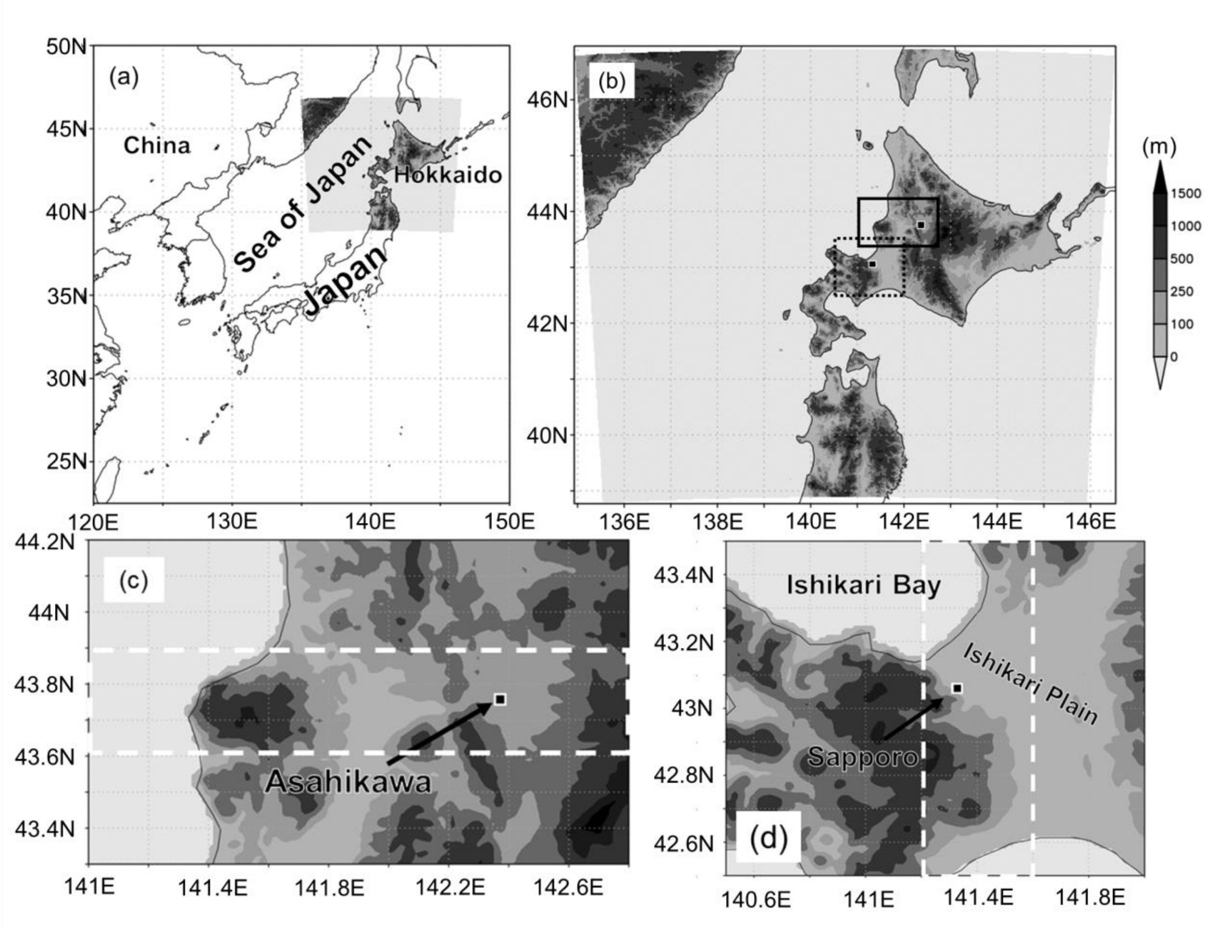

Fig. 3.1. (a) Map of Japan and the surrounding area, with shading indicating height in the model domain as shown in (b). (b–d) Maps zoomed in on (b) Hokkaido, (c) the solid square in (b), and (d) the dotted square in (b). The dashed white lines in (c) and (d) indicate the longitude and latitude bands, respectively, for the vertical cross section in Section 3.5. The shaded area in (a) shows the calculation domain in the model experiment.

The remainder of this Chapter is organized as follows. Section 3.2 describes observation data and model experiments. Section 3.3 explains the identification of precipitation types from disdrometer data. Section 3.4 defines the G/S ratio from observation and simulation data and shows the application of the ratio to model validation. Section 3.5 discusses the sensitivity of the results to different SOM configurations, training data, and grouping SOM nodes. Section 3.6 concludes Chapter 3.

3.2. Model and data

3.2.1. Observation data

The disdrometer data used in this paper were VSVD data collected at a site in Sapporo, Japan (43.083°N, 141.337°E; Fig. 3.1d) from 1 December 2017 to 28 February 2018 (Katsuyama and Inatsu 2021). The data were obtained every minute, but a 1-h interval was used. The VSVD was used in the comparison between observation and simulation data for specific events (Kondo et al. 2021). In Section 3.5.3, the SOM was classified by replacing the training data with the VSVD data at a site in Asahikawa, Japan (43.787°N, 142.347°E; Fig. 3.1c) for the same period as the Sapporo site. The altitudes of the Sapporo site and the Asahikawa site are 11.0 and 104.1 m, respectively. The VSVD instruments at Sapporo and Asahikawa were installed at heights of 1 and 2 m above ground level, respectively, so that they were not buried in snow cover. The instruments were enclosed by double wind-breaking nets to avoid the effect of turbulence. The details of the VSVD, including its location, are described in Katsuyama and Inatsu (2021), with photos (Fig. 1 of Katsuyama and Inatsu, 2021). The VSVD sampling volume was about 0.001 m^3. A set of diameter and fall velocity data of particles falling through the VSVD instrument was binned into equal-sized cells of the diameter-velocity space of 0.5 mm × 0.2 m s^{-1} every hour. We excluded particles smaller than 0.5 mm and slower than 0.2 m s^{-1} due to the limited VSVD detection range (Katsuyama and Inatsu 2021).

3.2.2. Model and experiment

The meteorological model used in this study was version 5.3.3 of Scalable Computing for Advanced Library and Environment (SCALE; Nishizawa et al. 2015; Sato et al. 2015). The model solves three-dimensional fully compressible non-hydrostatic equations with the prognostic variables of density, momentum, entropy, specific humidity, hydrometer mixing ratio, and the number concentration of hydrometeors. We selected a two-moment bulk scheme as cloud microphysics that simulates the hydrometers categorized as cloud droplets, rain, ice, snow, and graupel (Seiki and Nakajima 2014). In this scheme, the riming process is represented based on the stochastic collection equation, and the freezing process includes homogeneous and heterogeneous freezing (Seifert and Beheng 2006). The model includes parameterizations on turbulence (Nakanishi and Niino 2004), radiation (Sekiguchi and Nakajima 2008), urban (Kusaka et al. 2001) and land surface processes, and surface flux (Beljaars and Holtslag 1991; Wilson 2001). The sea surface temperatures were set as the same values as in the 3-h Mesoscale Analysis (MANL) with a horizontal resolution of 5 km, provided by the Japan Meteorological Agency (JMA; 2019).

We conducted a dynamical downscaling experiment to a 1-km horizontal grid interval with SCALE. The calculation domain mostly covered Hokkaido Island and its upstream area over the Sea of Japan (Fig. 3.1b). We set 57 vertical layers, the thickness of which stretched from 40 m above the ground to 650.5 m below the model top at 19.5 km to represent cloud growth in the planetary boundary layer. The model was numerically integrated from 1 December, 2017 to 28 February, 2018 (Inatsu et al. 2020). First, a single run started from 0000 UTC of each date in the integration period to 0600 UTC of the following date, and the first 6 h were the spin-up period, and thus were not analyzed. Next, we built the simulation data by serially connecting the output of the daily runs through the target period without their spin-up. The output interval was 30 min. The initial and lateral boundary conditions were taken from the MANL data of geopotential height, horizontal wind, air temperature, surface pressure, specific humidity, surface temperature, sea surface temperature, soil temperature, and soil moisture.

3.3. Evaluation of precipitation types from disdrometer data

The new approach for evaluating the precipitation types consists of the following three steps.

1. Derive the v-D relationship from the observed size-fall velocity data by the EM algorithm (KI20).

2. Classify the v-D relationship estimated in step 1 by using a SOM (Kohonen 1995).

3. Group each node classified by the SOM to identify the types of precipitation particles.

The details of step 1 are described in Section 3.3.1 and those of steps 2 and 3 are described in Section 3.3.2.

3.3.1. Velocity–diameter relationship

The development of the evaluation of precipitation types from disdrometer data began with estimating bivariate PDF and v-D relationships by the EM algorithm following KI20. We briefly review the part of KI20's work that was independent of the disdrometer instrument in the context of this study. For a single precipitation type (e.g., rain, hail, graupel, and snow) the disdrometer data, which are particle data or gridded particle data, were assumed to follow a joint PDF of gamma-distributed diameter and normally distributed fall velocity with its mean on a v-D relationship. The gamma distribution has shape and scale parameters of μ and λ; the normal distribution has a single parameter of standard deviation σ in fall velocity; and the v-D relationship has parameters of a and b [Eq. (3.1)]. An assumed conditional PDF is then symbolically expressed as $P_0(v, D|a, b, \sigma, \mu, \lambda)$ in units of seconds per meter per millimeter. The EM algorithm found the optimal parameter set in P_0 and the resultant parameters of a_0 and b_0 determined the v-D relationship of $v = a_0 D^{b_0}$.

In snow events, the dominant types of precipitation particles near the surface are graupel and snow in the model. Therefore, graupel and snow, and their mixture must be considered. For mixtures of precipitation types with different v-D relationships, the disdrometer data were assumed to follow a linear combination of PDF for precipitation type $P_1 = P_0(v, D|a_1, b_1, \sigma_1, \mu_1, \lambda_1)$ and other precipitation type $P_2 = P_0(v, D|a_2, b_2, \sigma_2, \mu_2, \lambda_2)$ of $P_m = \omega_1 P_1 + \omega_2 P_2$, where dimensionless ω_1 and ω_2 are a mixing fraction of the precipitation type and the other precipitation type, respectively, satisfying $\omega_1 + \omega_2 = 1$. The EM algorithm found the optimal parameter set in P_m. The resultant parameters in P_m determined two v-D relationships of $v = a_1 D^{b_1}$ and $v = a_2 D^{b_2}$ [Eq. (3.1)]. When the EM algorithm was converged in the mixed PDF estimate, mixed PDF P_m was adopted. At point (v_0, D_0) in diameter-velocity space, if a PDF (P_1) was classified as graupel and the other (P_2) as snow, the fraction of graupel was $\gamma_1(v_0, D_0) = \omega_1 P_1(v_0, D_0)/P_m(v_0, D_0)$ and that of snow aggregates was $\gamma_2(v_0, D_0) = \omega_2 P_2(v_0, D_0)/P_m(v_0, D_0)$.

For this study, ω_1 and ω_2 were chosen to account for graupel, snow and their mixture. However, depending on the classification of the precipitation particles, users can adjust the number of ω. The selection of the number of ω affects the number of particles required for successful estimation using the EM algorithm (Katsuyama and Inatsu, 2020), but the constraints related to the number of particles can be mitigated by coarsening the temporal resolution of the classification or increasing the number of instruments to observe more particles.

To overcome the constraint relating to the number of particles, we used the data with a 1-h interval. However, while the new method can estimate multiple particle size-fall relationships for hourly interval observations, the habit could easily change from graupel to snow aggregate within 1 h in precipitation systems such as a low-pressure system (e.g., Colle et al., 2014). For future detailed analyses (e.g., various synoptic condition events and fine time scale changes of solid particle habits), the required number of particles should be measured by increasing the number of observation instruments or improving the sampling rate of the disdrometer.

3.3.2. Identification of precipitation types

The EM algorithm converted the hourly particle number data in equally sized cells in the velocity–diameter space to an optimal bivariate PDF. The hourly data were used to satisfy the required sampling number for the EM algorithm. A set of hourly v-D relationships generated by the EM algorithm was transformed into SOM input vectors, each of which consisted of velocity values corresponding to diameter grid points ranging from 0.1 mm to 5 mm in 0.1-mm intervals. The SOM map was constructed using all the input vectors derived from the EM algorithm. For mixtures, each of the two v-D relationships could be input independently. These input vectors are required to exclude unrealistic fall velocity calculated by the EM algorithm when b is negative or the v-D curve is concave downward. The threshold for exclusion is determined by the user and should be chosen based on the realistic fall velocity of the precipitation types to be classified and the shape of the v-D curve. In this study, v-D relationships with a negative b and those with maximum velocities exceeding 100 m s^{-1} were excluded because these relationships are unrealistic.

Next, the size of the SOM map, which is the basis of the classification, must be defined. The size is an artificial parameter in machine learning and depends on the number of input vectors and the types of precipitation particles to be classified. Therefore, users must try multiple sizes of SOM maps, as this is inherent to the nature of SOM. In this study, the reference SOM map was 4 × 4 nodes trained by the v-D relationships through the EM algorithm based on the hourly disdrometer data at the Sapporo site from 1 December, 2017 to 28 February, 2018 (Fig. 3.2a). We discuss the SOM configuration sensitivity in Section 3.5.1 and the training data sensitivity in Section 3.5.3. The SOM map contained upper left nodes associated with lower fall velocities at larger particle sizes and the lower right ones associated with higher fall velocities at smaller particle sizes. This feature indicated that the upper left and lower right nodes corresponded to snow-like and graupel-like v-D relationships, respectively.

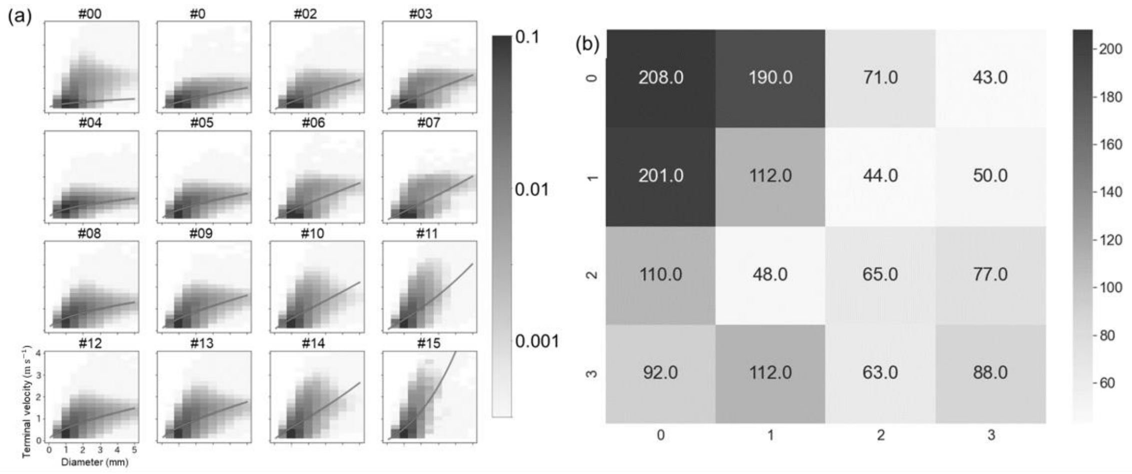

Fig. 3.2. (a) Reference SOM map created by the EM algorithm learning the v-D relationships from hourly disdrometer data at the Sapporo site from 1 December 2017 to 28 February 2018. Shading shows the normalized particle-number frequency at each node in the cells retrieved by the composite average as the reference on the right of the velocity–diameter space. The solid line in each node denotes the v-D relationship reconstructed from the SOM output vector. (b) Number of input v-D relationships.

Table 3.1. Type of graupel and snow reported in Locatelli and Hobbs (1974) and the corresponding nodes in the reference SOM map.

Particle type	Node
Lump graupel (density range: >0.1 to 0.20 mg m^{-3})	#15
Lump graupel (density range: >0.2 to 0.45 mg m^{-3})	#14
Conical graupel	#11
Hexagonal graupel	#11
Graupel-like snow of lump type	#13
Graupel-like snow of hexagonal type	#08
Densely rimed columns	#14
Densely rimed radiating assemblages of dendrites	#13
Densely rimed dendrites	#04
Aggregates of unrimed radiating assemblages of plates, side planes, bullets, and columns	#12
Aggregates of unrimed radiating assemblages of dendrites	#08
Aggregates of densely rimed radiating assemblages of dendrites	#08
Aggregates of unrimed side planes	#08

Grouping 16 SOM nodes (i.e., 4 × 4 nodes) into cases of graupel, snowfall, and error was based on the v-D relationships reported by Locatelli and Hobbs (1974), fraction of variance unexplained (FVU), and measured particle numbers used to obtain v-D relationships for each node. The nearest v-D relationship in the reference SOM map to each type of solid precipitation measured by discretized velocity vectors is shown in Table 3.1. The Euclidean distance was used to determine the similarity of the v-D relationship in the reference SOM map to that of the literature. First, node #00 was

grouped into error because the observed particle number used by KI20 to calculate the input velocity vectors was two orders of magnitude less than the others. KI20 reported that the estimation performance was worse for data sizes smaller than 2000 compared with larger data sizes. Due to the small number of observed particles, the FVU of node #00 was large, supporting the assignment of node #00 as error. The details of FVU and measured particle numbers are presented in Appendix 3A. Next, nodes #11, #14, and #15 were categorized as graupel because the patterns of the learned velocity–diameter vector were similar to that shown in Locatelli and Hobbs (1974). Although the curves derived from observations (e.g., Locatelli and Hobbs 1974) and theoretical formulation (e.g., Mitchell 1996) are upwardly convex curves, they had unrealistic downwardly convex curves in the output of the EM algorithm due to data truncation for the limited observation range of VSVD measurements (Section 3.2.1). In addition, lump graupel in #14, which had a higher density than lump graupel in #15 (Table 3.1), showed a lower fall velocity. Therefore, the fall velocity of the lump graupel with a high density was slower than that with a low density. This non-physical discrepancy originated from the range of diameter and fall velocity used in the EM algorithm and SOM being wider than that in Locatelli and Hobbs (1974), and the problem could exist in general cloud microphysical schemes. However, these lines do not pose mathematical difficulties for the EM algorithm. The nodes elsewhere fell into the snow group. For v-D relationships that were not in the literature, we determined them as graupel or snow according to our judgment based on the sensitivity experiment. The grouping in Fig. 3.2(a) is shown again in Fig. 3.3(a) with the grouping boundary. We ignored the problem that some nodes did not correspond to any v-D relationships in previous studies. The sensitivity of the grouping to the results is discussed in Section 3.5.2.

After the grouping, the PDF and the mixing fraction obtained by the EM algorithm (i.e., P_0, P_1, P_2, ω_1, and ω_2) were separated into graupel-like PDF, snow-like PDF (P_g and P_s), and their mixing fraction (ω_{g} and ω_{s}). The number of graupel particles in a cell of $\mathrm{C} = [v_0, v_0 + \Delta v] \times [D_0, D_0 + \Delta D]$ is

$$N_{\mathrm{G}}(C) = N(C) \times \gamma_{\mathrm{G}}(C), \tag{3.2}$$

where $N(C)$ is the total number of particles in C, v_0 and D_0, are the arbitrary values of v and D in the measurement range, and Δv and ΔD are the size of bin for the v and D direction, respectively. Similarly, the number of snow aggregate particles in a cell, C, is

$$N_{\mathrm{S}}(C) = N(C) \times \gamma_{\mathrm{S}}(C). \tag{3.3}$$

The procedure for classifying precipitation particles in this section is summarized as a schematic in Fig. 3.4. This method is also applicable to other disdrometer data, such as gridded data and data per particle. If more diverse training data are available, including different types of precipitation such as rainfall and hail in other areas, the size and boundaries of the SOM map could be further diversified. Additional efforts to obtain diverse training data are required in future work.

In this study, we applied this new evaluation method to the observation data of particle size and fall velocity in winter in Hokkaido, and the classified observation data by the new method was compared with that estimated by a meteorological model as an example of the application of the new method (Section 3.4). We examined the sensitivity of the SOM (Section 3.5).

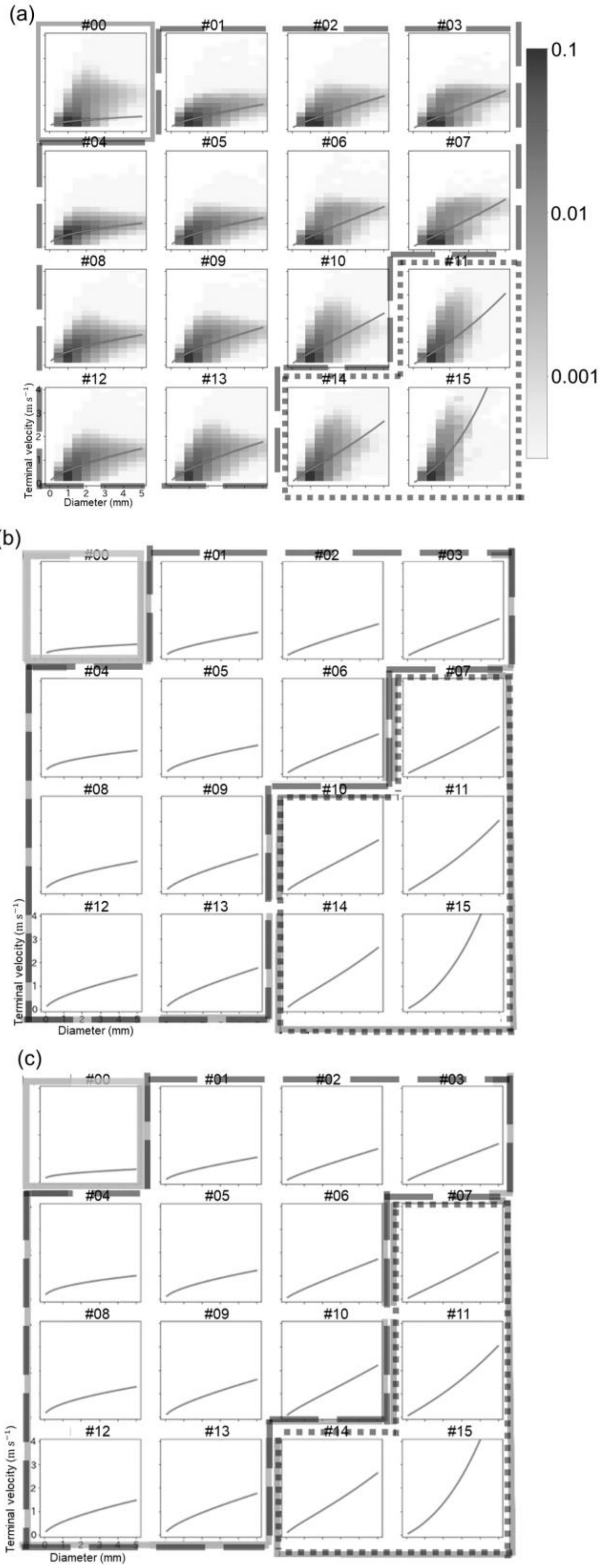

Fig. 3.3. Grouping of (a) original, (b) B5, and (c) B4 separations. Shading in (a) is the same as in Fig. 3.2a, but with grouping boundaries. Nodes of error, snow, and graupel are enclosed by solid, dashed, and dotted lines, respectively.

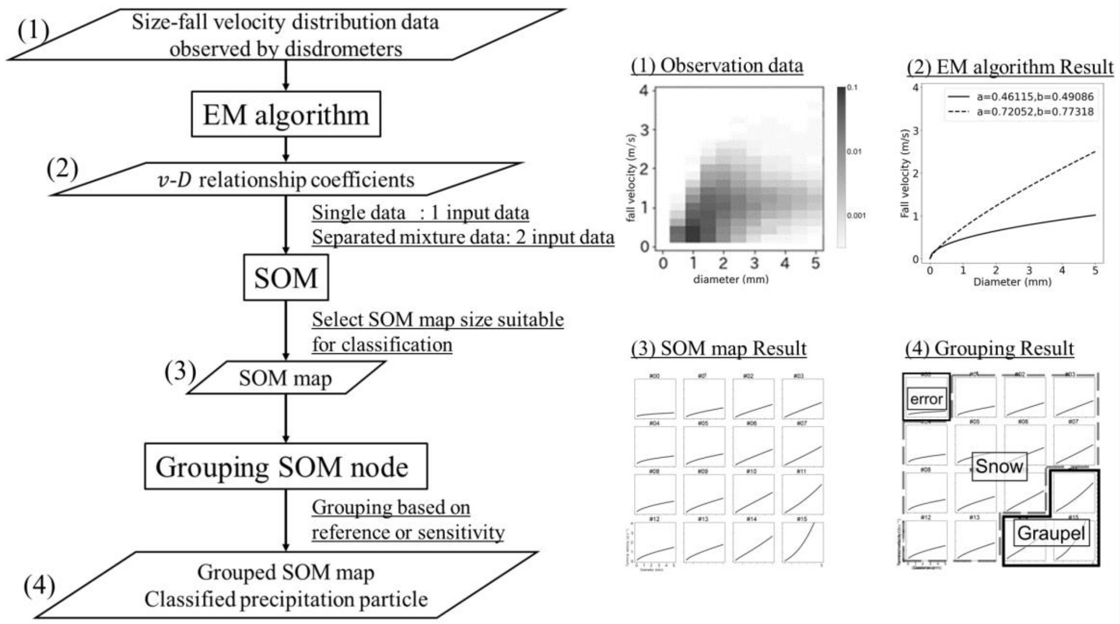

Fig. 3.4. Schematic of the classification procedure for precipitation particle types using the EM algorithm and SOM. Example results for each process in the parallelogram correspond to panels (1) to (4) next to the diagram.

3.4. Application to model validation

3.4.1. Graupel-to-solid precipitation ratio

We applied our new method to the validation of the meteorological model with the G/S ratio. The G/S ratio is a key element of the reasonable simulation of snowfall because the difference in the terminal velocity of graupel and snowflakes strongly affects the geographical distribution of snowfall (Magono et al. 1966; Smith and Barstad 2004). The validated meteorological model allowed us to analyze snowfall dominated by graupel based on cloud microphysical processes. This analysis required a comparison of days with high and low G/S ratios.

In the comparison of the observation and simulation data, the difference in the absolute value of particle numbers must be addressed. Some disdrometers often missed small-sized particles, and model results depend on the size distribution assumed in bulk cloud microphysics schemes. Relative particle numbers should be used to validate the cloud microphysical schemes in meteorological models by comparing the schemes with disdrometer data. Because the graupel and snow aggregate categories were used, the G/S ratio was defined based on the disdrometer data.

v-D relationships linked with graupel or snow aggregates were obtained by the method described in Section 3.3. The disdrometer data at a specific time were then linked with a single SOM node for graupel-only or snow-only PDFs (Section 3.3.2). The data were linked with two SOM nodes for mixture PDFs; the number of particles was divided into the fraction of graupel and snow particles obtained from the EM algorithm (ω_{g} and ω_{s} in Section 3.3.1). Following the grouping in Section 3.3.2, the number of particles in cells in the velocity–diameter space was counted as graupel when the time sample was linked with SOM nodes #11, #14, and #15, whereas the particles were counted as snow when the sample was linked with snow-group SOM nodes (Fig. 3.3a). When the time sample was linked with two SOM nodes, that is, one in the graupel group and the other in the snow group, the number of particles were divided according to the fraction of graupel and snow particles. The numbers of graupel and snow particles, N_{G} and N_{S}, were then obtained in each hour, so the daily G/S ratio (r) was defined as

$$\boldsymbol{r} = \frac{\sum_{\boldsymbol{n}=\mathbf{0}}^{\mathbf{23}} \boldsymbol{\omega}_{\mathbf{G},\boldsymbol{n}} \boldsymbol{N}_{\mathbf{G},\boldsymbol{n}}}{\sum_{\boldsymbol{n}=\mathbf{0}}^{\mathbf{23}} \boldsymbol{\omega}_{\mathbf{G},\boldsymbol{n}} \boldsymbol{N}_{\mathbf{G},\boldsymbol{n}} + \boldsymbol{\omega}_{\mathbf{S},\boldsymbol{n}} \boldsymbol{N}_{\mathbf{S},\boldsymbol{n}}}, \tag{3.4}$$

where n is the number of hours from 0000 UTC in a day.

The G/S ratio in the simulation was also defined as the number concentration ratio of graupel to the sum of snow and graupel in the bottommost layer. The days were excluded on which the model did not reproduce precipitation events and on which the liquid precipitation was simulated because the VSVD was unable to detect liquid particles (Katsuyama and Inatsu 2021).

3.4.2. Model validation

The temporal evolution of the G/S ratio estimated by our new method at Sapporo is shown in Fig. 3.5a. The estimated G/S ratios in December and January showed large variability, with 8 days exceeding ratios of 0.3, whereas in most of February the estimated G/S ratios were less than 0.3. Fig. 3.6a shows the normalized frequency of the estimated G/S ratio in each month. In December, over 80% of days had a G/S ratio of less than 0.3, but some days with G/S ratios exceeding 0.3 were observed during precipitation extending across multiple days (Fig. 3.5a). In January, almost 20% of the days had a G/S ratio greater than 0.3, and high G/S ratios were frequently observed. In February, the G/S ratio was less than 0.3 for almost 90% of the days, with the ratio mostly close to 0 (Fig. 3.5a). Thus, the G/S ratio estimated from the disdrometer data showed the intra-seasonal variability of solid precipitation types, suggesting changes in the products observed near the ground of cloud microphysical processes over synoptic timescales during a winter season. The estimated G/S ratio at Asahikawa was less than 0.3 on almost all days during the target period (Figs. 3.5b and 3.6b), which suggests a difference in dominant cloud microphysical processes for precipitation particles between Sapporo and Asahikawa.

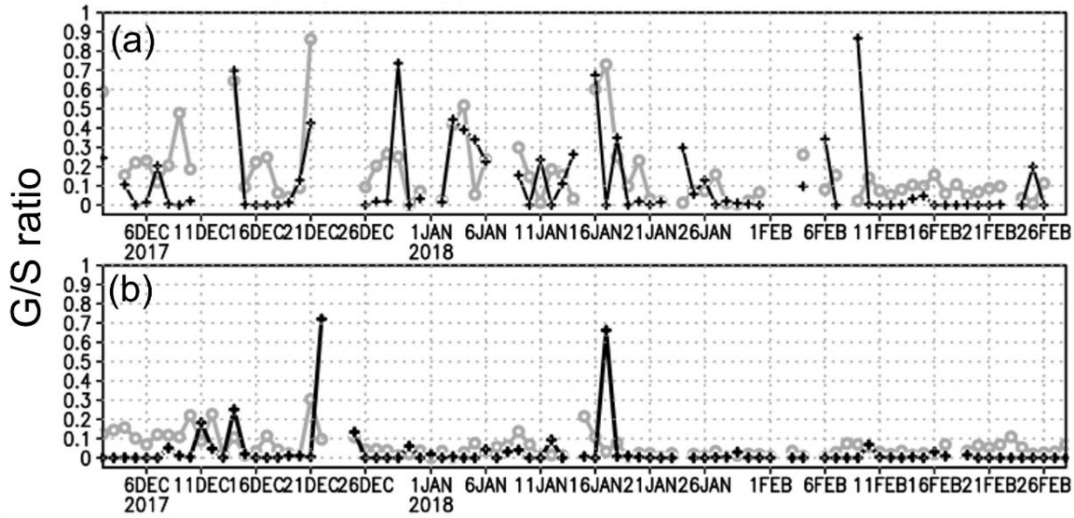

Fig. 3.5. Daily G/S ratio at (a) Sapporo and (b) Asahikawa from 2 December 2017 to 28 February 2018. Black lines with crosses show the estimates from the disdrometer data with the automatic discrimination algorithm developed in Section 3.3. The gray line with open circles indicates the simulation results.

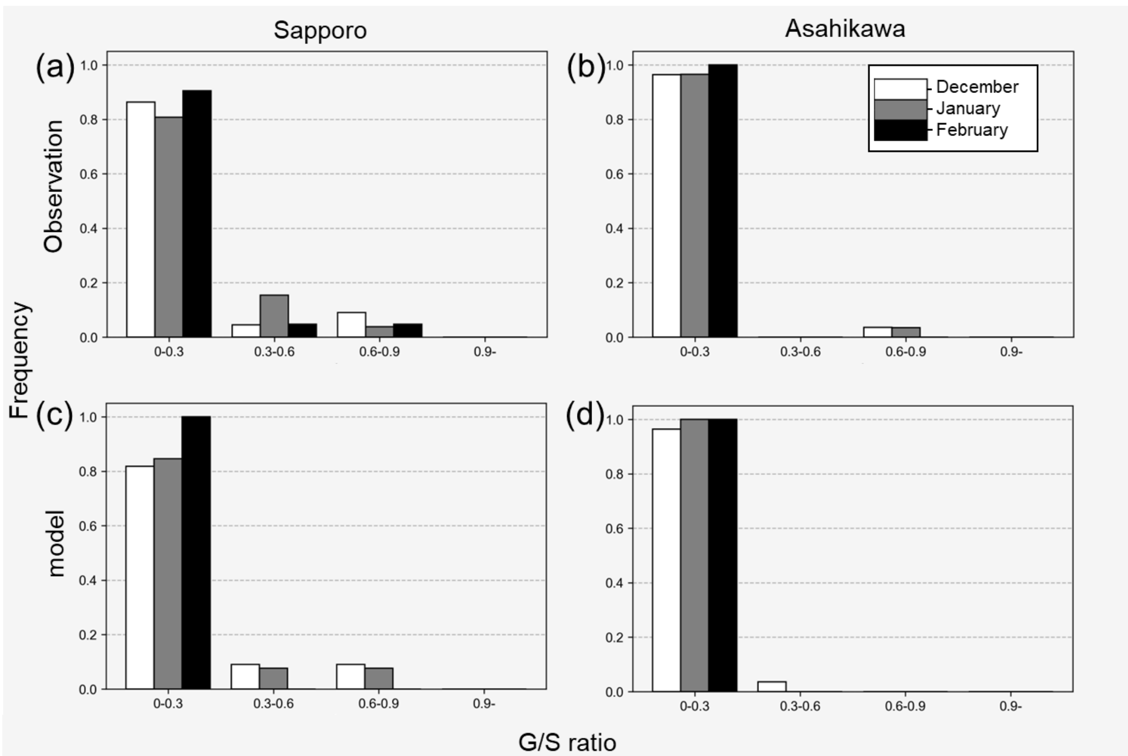

Fig. 3.6. (a, b) Monthly normalized frequency of the observed G/S ratio at (a) Sapporo and (b) Asahikawa in (white) December, (gray) January, and (gray) February. (c,d) Same as (a,b), but for the simulation. The simulated G/S ratio occasionally shows values of approximately 0.2 for observations with G/S ratios below 0.1. Therefore, a sensitivity experiment was conducted in Appendix D, leading to the determination of a threshold of 0.3.

The high ratio frequency of both the simulated G/S ratio and that observed at the Sapporo site decreased from December to February, with a slight overestimation in December and a slight underestimation in February (Fig. 3.6c). The worst overestimations occurred around 6 December and 16 December (Fig. 3.5), when a low-pressure system passed. This is presumably because solid precipitation particles can grow in a variety of habits determined by the ambient conditions in low-pressure systems with large spatial variations in temperature and water vapor inside the systems (Colle et al. 2014). This result implies that the representation of position and ambient conditions in low-pressure systems could affect the simulated G/S ratios. In addition, the simulated precipitation area sometimes differed by several kilometers from the observed precipitation area. The temporal evolution of the G/S ratio included the surrounding 10×10 km grids (Fig. 3.C1), indicating that such a discrepancy partly affected the difference in the absolute value of the G/S ratio between the model and the observation. However, this problem did not originate from the new method for deriving G/S ratio, but from the model uncertainty. Despite the effects of this problem, the low ratio observed in February was reproduced by the simulation (Fig. 3.6c). In addition, the simulated G/S ratio at Asahikawa was less than 0.3 during most of the target period (Figs. 3.5b and 3.6d), which was similar to the observed G/S ratio. Therefore, via the automated identification of particle types from the disdrometer data (Section 3.3), we confirmed that the model captured the difference in G/S ratio between Sapporo and Asahikawa and the intra-seasonal variability of the G/S ratio during winter by comparison with the observed G/S ratio (Fig. 3.6).

3.5. Sensitivity tests

3.5.1. SOM configuration

Sensitivity tests were performed by changing the SOM configuration to 3 × 3 and 5 × 5 (Fig. 3.7). For the 3 × 3 map, the general characteristics of the classification were similar to that of the 4 × 4 map. However, nodes #7 and #8 of the 3 × 3 SOM map are regarded as both snow and graupel in the literature based on the Euclidean distance, whereas in the 4 × 4 SOM map, there was no overlap between graupel and snow nodes. In contrast, in the 5 × 5 SOM map, many nodes did not have the v-D curves referred to in the literature, making it difficult to classify graupel and snow clearly based on the v-D curves of each node. Therefore, we concluded that the SOM configuration should be 4 × 4 to identify graupel and snow clearly.

It is possible to select a SOM configuration with a larger number of node than we examined (e.g., 10 × 10, 20 × 20 and so on), if we obtain the various types of v-D curves and a sufficient number of v-D curves for each node. In this study, we examined SOM configurations of 3 × 3, 4 × 4, and 5 × 5 because the number of v-D curves for each node was acceptable for conducting the SOM analyses. For detailed analyses using larger SOM sizes, more measurement data should be obtained for various types of precipitation particle.

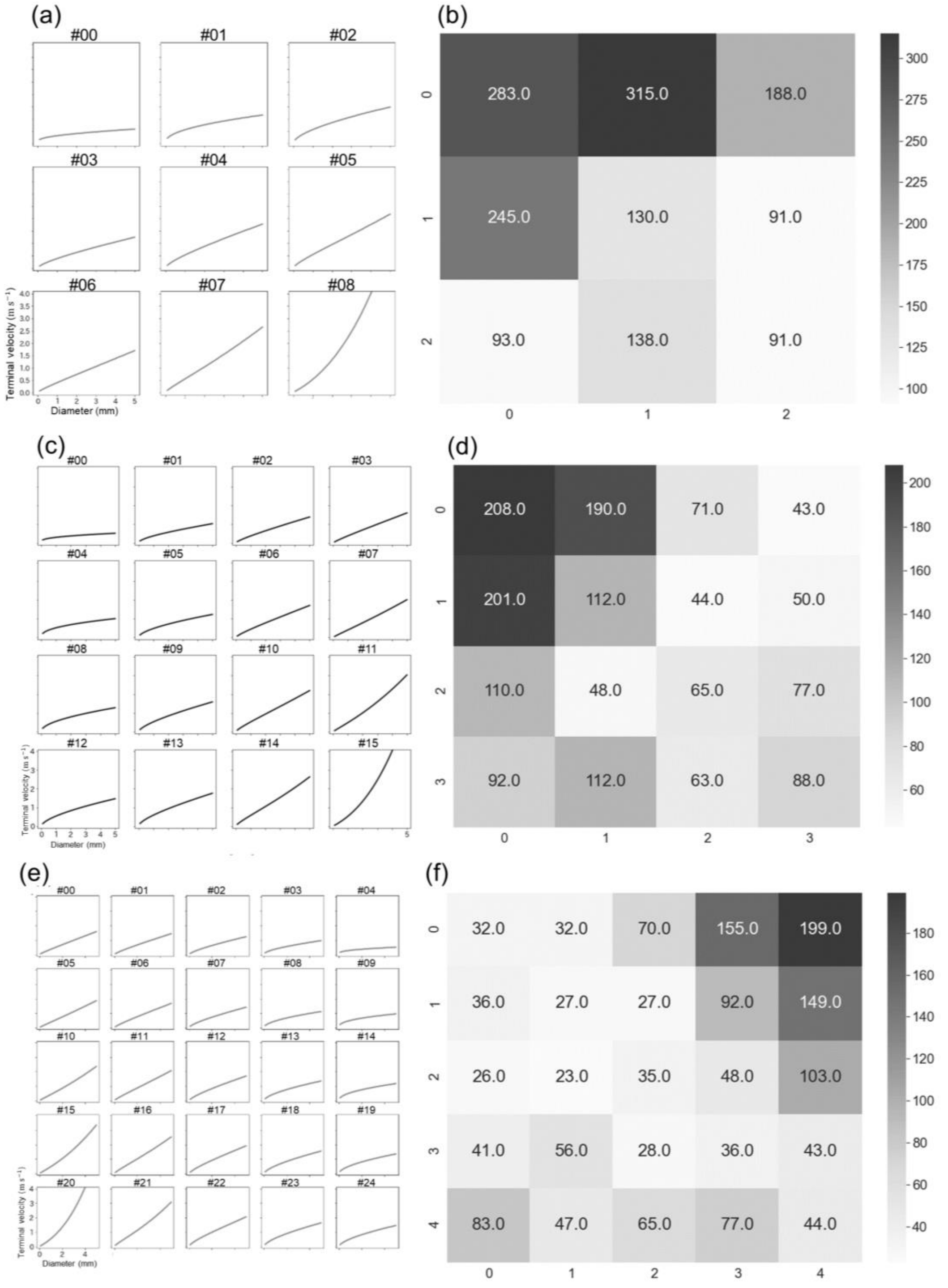

Fig. 3.7. (a, c, e) Reference SOM map obtained by learning the velocity–diameter curves with the EM algorithm based on hourly disdrometer data measured at Sapporo from 1 December 2017 to 28 February 2018 with (a) 3 × 3, (c) 4 × 4, and (e) 5 × 5 map sizes. Each node contains a curve reconstructed from the SOM output vector, shown as a solid line. (b, d, f) Number of input vectors derived from the observation data measured at the Sapporo site at (b) 3 × 3, (d) 4 × 4, and (f) 5 × 5 map sizes projected onto the reference SOM nodes shown in (a), (c), and (e), respectively.

3.5.2. Grouping

The grouping in Section 3.3.1 was arbitrary because some nodes were near the boundary between the graupel and snow aggregate groups. For example, nodes #7 and #10 could be regarded as both graupel and snow. To examine the effects of the treatment of nodes #7 and #10, the groupings shown in Fig. 3.3b (grouping B5) and Fig. 3.3c (grouping B4) were tested. The temporal evolution of the G/S ratio with these two groupings is shown in Fig. 3.8. In the setup of the boundary of B4 and B5, extending the graupel nodes increased the G/S ratio compared with the original grouping. However, the increases on days with a G/S ratio exceeding 0.3 for B4 and B5 were 4.4% and 16.2%, respectively, and both B4 and B5 could distinguish the high and low G/S ratio days (Fig. 3.9). Therefore, all groupings were acceptable for distinguishing the days with high and low G/S ratios. However, we selected the original grouping because all the nodes grouped as graupel had literature references corresponding to graupel (Locatelli and Hobbs, 1974). Considering that the v-D relationship assumed for each precipitation type is different for each model, the most suitable grouping could be different from the original grouping if this method were applied to the validation of other cloud microphysical schemes. In addition, if our method were used for validating cloud microphysical schemes that separate solid precipitation particles into four or more categories (e.g., ice, snow, graupel, and hail), grouping into categories other than snow and graupel would be required.

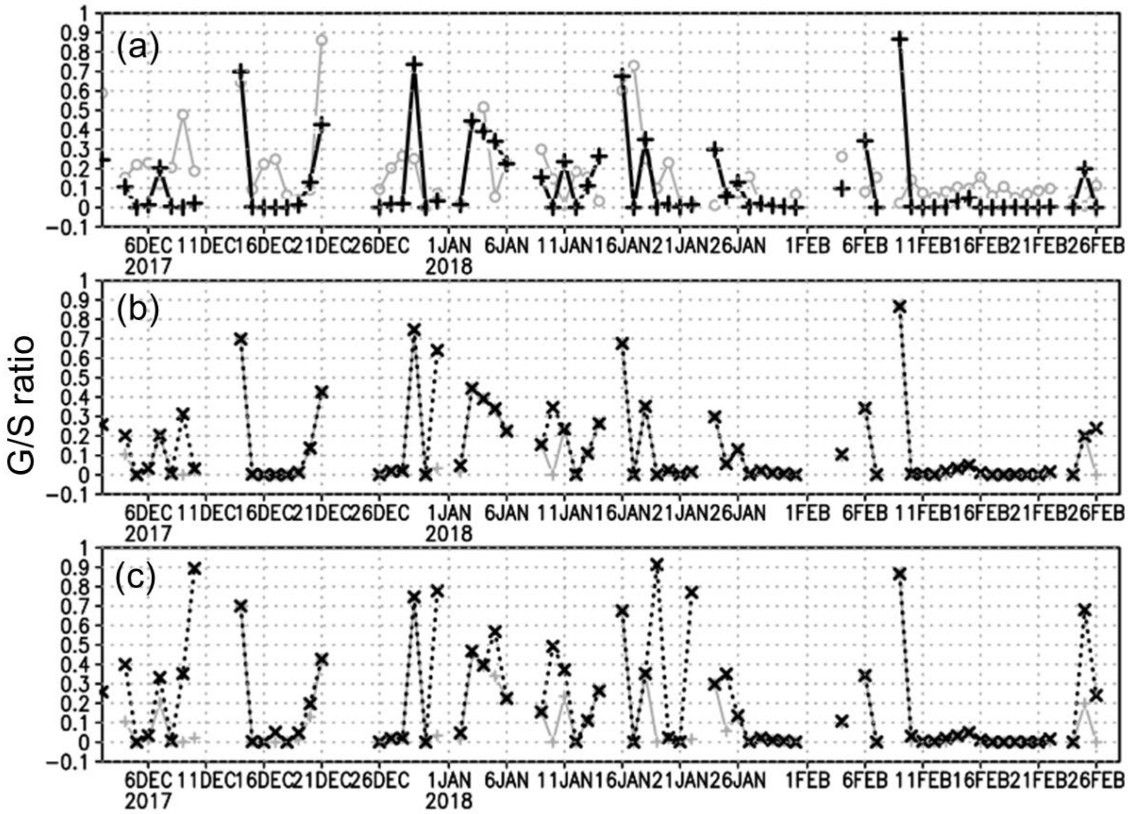

Fig. 3.8. Same as Fig. 3.5a but for the boundary sensitivity test. (a) Gray line with open circles and black line with crosses indicate the G/S ratio from observations and the model, respectively. (b, c) Gray line with crosses and the black dotted line with x symbols indicate the G/S ratio from the original and sensitivity test grouping, respectively. The lines for the sensitivity test in (b) were derived in the same way as for the separation graupel and snow particles by the original grouping, which is same as Fig. 3.3a but for B5, and in (c) was derived in the same way as in (b), but for B4.

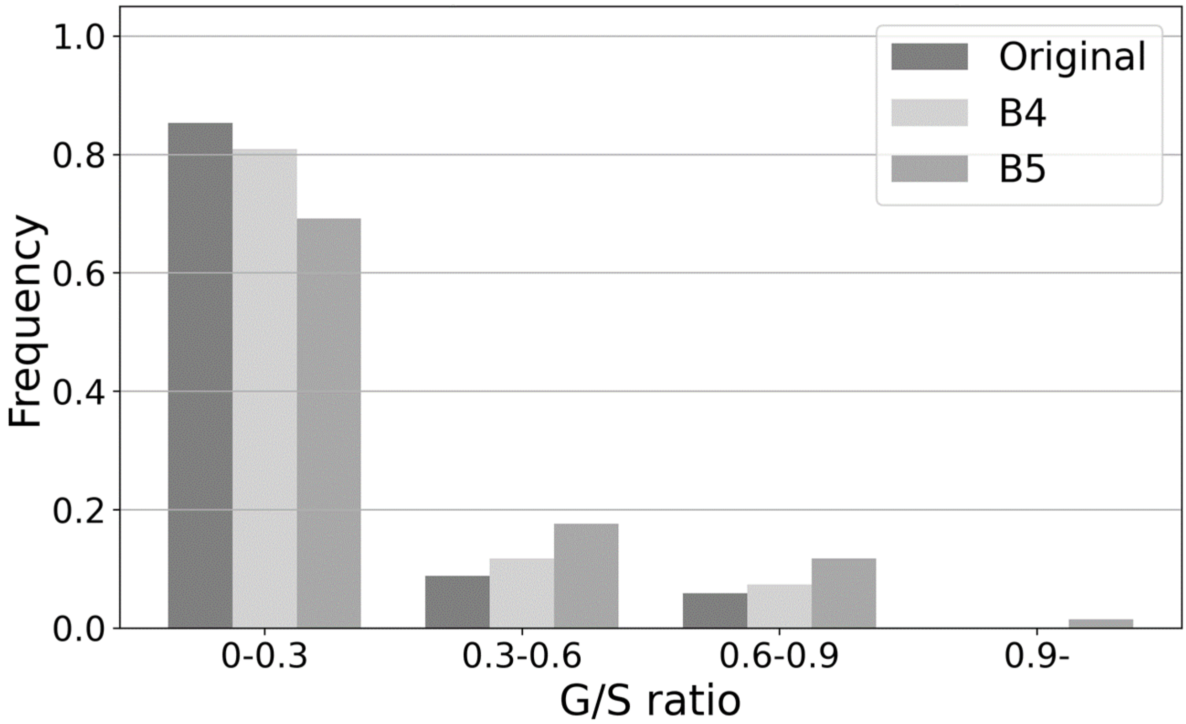

Fig. 3.9. Same as Fig. 3.6a but for the 3-month period of December, January, and February derived from the original, B4, and B5 groupings.

3.5.3. Training data in SOM

The results of the SOM classification were expected to depend on the training data. The training data were replaced with the disdrometer data from the Asahikawa site. The SOM map was consistent with the pattern observed in the reference SOM map based on the Sapporo data (Fig. 3.10), whereby the nodes in the lower right corner of the map exhibited a higher falling velocity, whereas those towards the left displayed a lower falling velocity. This pattern suggested that other training data for v-D relationships could also be classified by a SOM map. However, graupel was less frequent at Asahikawa, as shown by the G/S ratio at the Asahikawa site based on the nearest-neighbor fitting to the reference SOM map trained by the data from the Sapporo site (Fig. 3.5b). The pattern was consistent with the statistical characteristics of graupel precipitation days over Japan including Sapporo and Asahikawa (Mizuno 1992). The SOM map trained by the data from the Asahikawa site deemphasized the graupel nodes; nodes #11 and #14 were unclear because they were near the boundary of the graupel and snow groups. This result suggested that the training data reasonably included as many solid precipitation types as possible, rather than being biased towards a specific type of solid precipitation, such as only snow particles. In an example of an application in Section 3.4, graupel particles were needed as the training data for the SOM. It would be desirable to extend the observation sites, so that the data from various observation sites could be included to train a more general SOM map. However, the effect of the training data was small on separating days with the high and low G/S ratio because the G/S ratio was less than 0.3 for most of the target period, and the G/S ratio frequency showed small differences (Fig. 3.11).

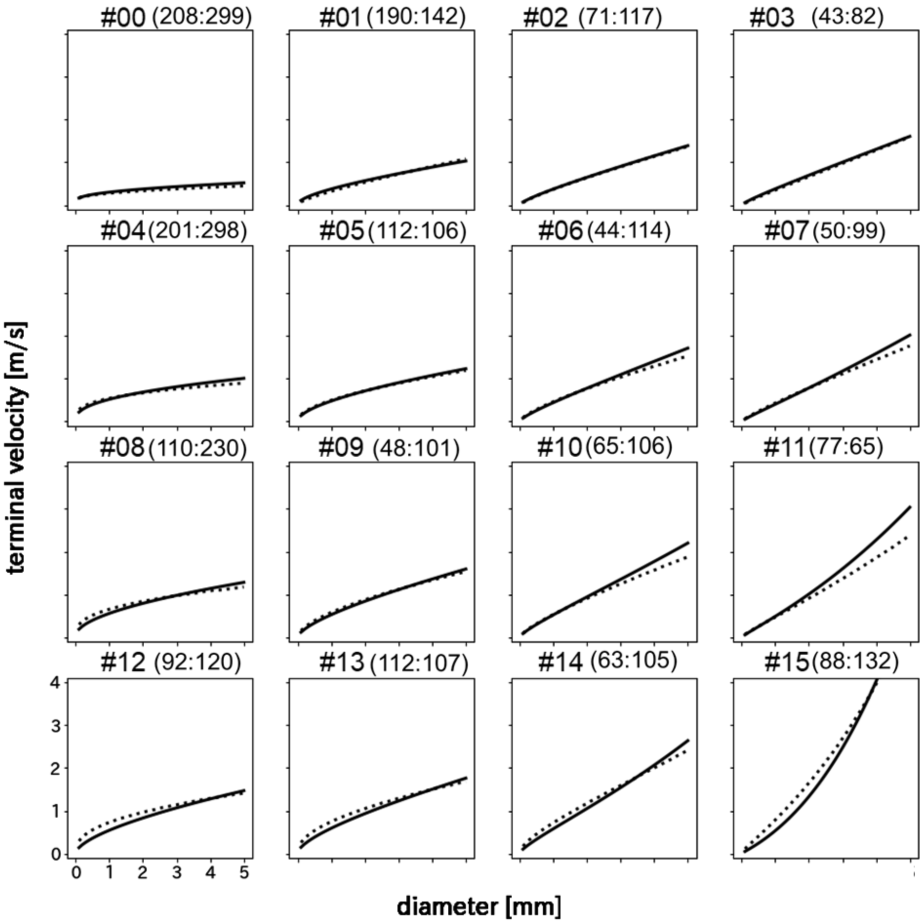

Fig. 3.10. Same as Fig. 3.2a, but for the SOM results trained by data from the Sapporo and Asahikawa sites. The numbers in the parentheses denote the number of input vectors (left and right numbers show the number of data in each node for the Sapporo and Asahikawa data, respectively). The SOM results trained with data from Sapporo and Asahikawa sites are shown by the solid lines and those trained with data from the Sapporo site are shown by the dotted lines.

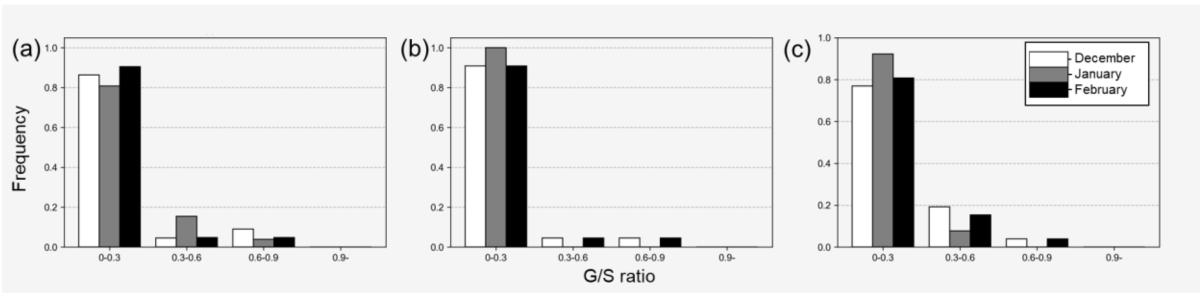

Fig. 3.11 Same as Fig. 3.6, but for G/S ratio trained by (a) only Sapporo data, (b) both Sapporo and Asahikawa data, and (c) only Asahikawa data.

Considering the selection of suitable training datasets, the simulation results in Section 3.4 provided a clue to which environments produce a variety of particle types (i.e., graupel and snow aggregates). To compare days with high and low G/S ratios using simulation results, we made a composite map from the model output over days where the G/S ratio at the Sapporo site exceeded 0.3. There were 4 days with a high G/S ratio and 27 days with a low G/S ratio. Solid precipitation originated from the streak cloud band that formed as a horizontal roll convection in a boundary layer with directional shear over the Sea of Japan in the winter monsoon season, with cloud tops ranging from 2 to 3.5 km (Tsuchiya and Fujita 1967). The map demonstrated that the abundant liquid water in the atmospheric boundary layers was consumed mainly by the riming process (Figs. 3.12b, d), which was highly efficient for graupel generation. However, the composite map over days with G/S ratios less than 0.3 showed that the abundant liquid water was mostly consumed by freezing, not riming (Figs. 3.12a, c). In general, riming occurs mainly when liquid water is present in the temperature range of −15 °C to −5 °C (Pflaum and Pruppacher 1979; Pruppacher and Klett 1997; von Blohn et al. 2009), and at lower temperature ranges, freezing mainly occurs within convective clouds (Korolev 2007). The liquid water was distributed in the layer with the temperature range in the composite with the G/S ratio exceeding 0.3 (Fig. 3.12f). In contrast, the temperature of the layer in which the liquid water was mainly distributed was −25 °C to −15 °C in the composite with the G/S ratio of less than 0.3 (Fig. 3.12e). This characteristic was also found on most snowy days over Asahikawa and the windward area (west) of Asahikawa (Fig. 3.13). Liquid water in the temperature range suitable for riming was critical for the graupel fall near the ground; otherwise, snowfall was dominant. Therefore, we suggest that one choice for training disdrometer data is a site that can experience the temperature range at the cloud altitudes during the observation period.

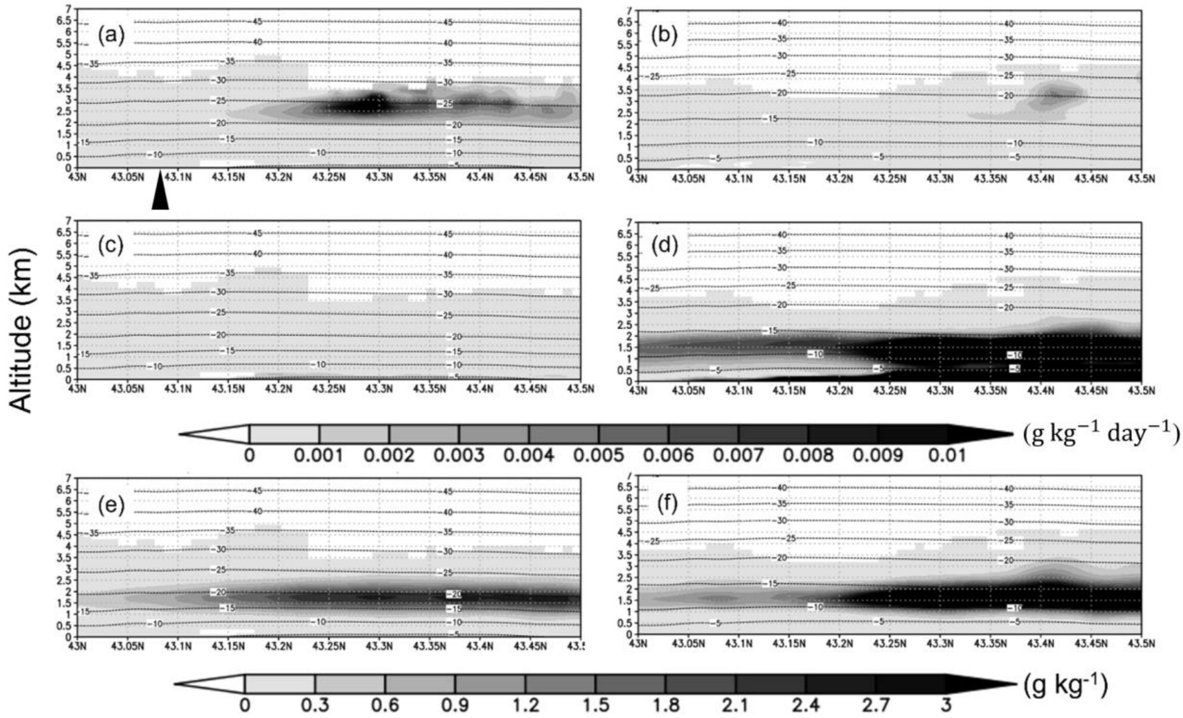

Fig. 3.12. Left panels (a, c, e) show the composite of cases with G/S ratios of <0.3 and right panels (b, d, f) show same as the left panels, but for G/S ratios of >0.3. (a, c, e) Composite of (a) freezing rate (g kg^{-1} day^{-1}), (c) riming rate (g kg^{-1} day^{-1}), and (e) liquid water mixing ratio (g kg^{-1}) in the vertical cross section zonally averaged over the meridional band shown in Fig. 3.1d (observation site was at 43.083°N, which is marked with a triangle in panel (a)). The reference for freezing and riming rates is below (c, d) and that for liquid water mixing ratio is below (f). Contour shows air temperatures with 5 °C intervals.

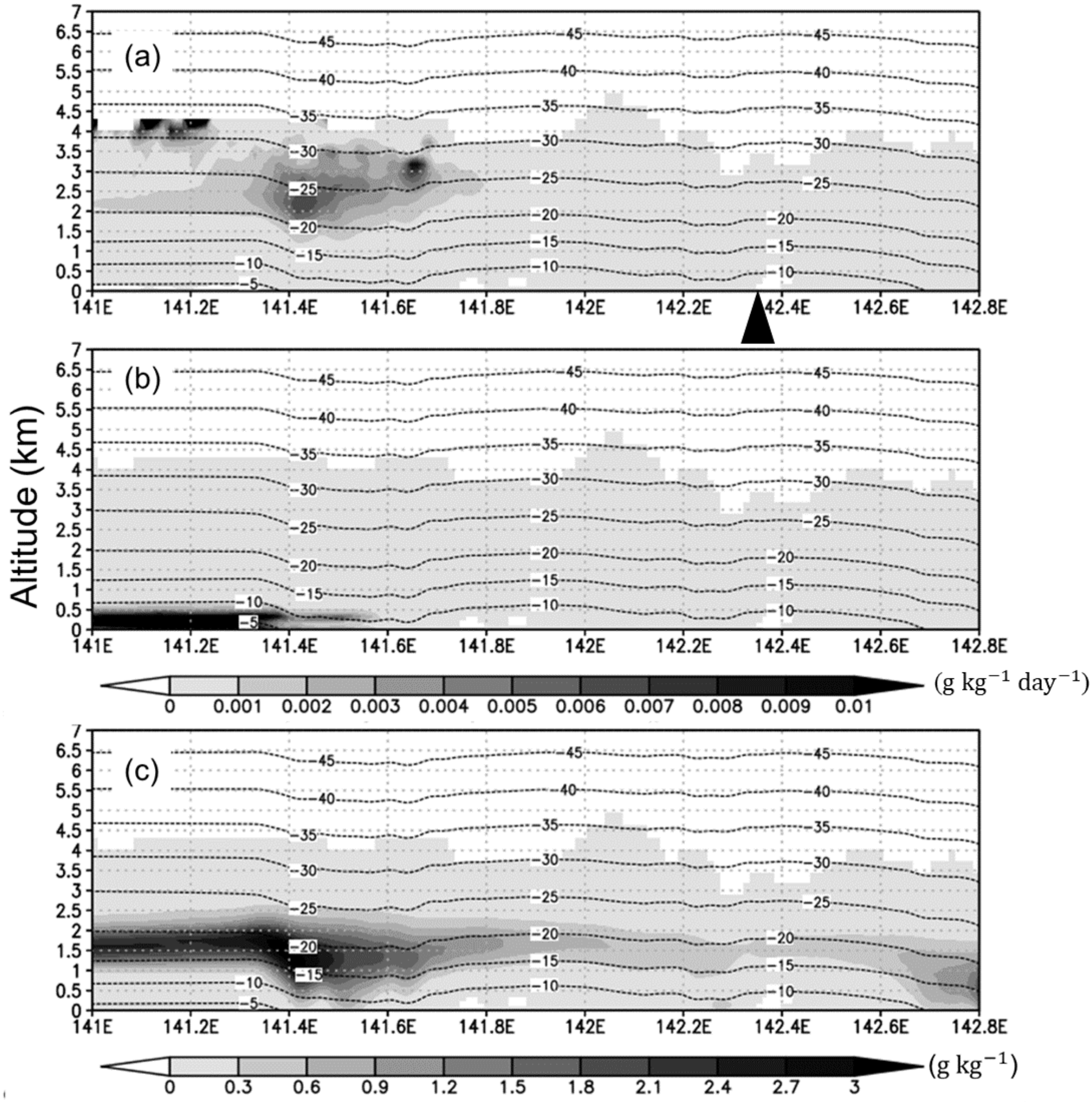

Fig. 3.13. Composite of (a) freezing rate (day^{-1}), (b) riming rate (day^{-1}), and (c) liquid water mixing ratio (g kg^{-1}) for the snowfall days at Asahikawa (observation site was at 142.347°E, marked by a triangle in panel (a)) due to cloud streaks in the vertical cross section meridionally averaged over the zonal band shown in Fig. 3.1c.

3.6. Conclusion

We developed an evaluation method that uses machine learning techniques to determine the precipitation particle types from size-fall velocity data observed by disdrometers. The method was applied to size-fall velocity data observed in winter. Following KI20, we first determined the v-D relationship(s) based on the single or mixed PDF estimate from a set of size-fall velocity data using the EM algorithm. We input VSVD data (Katsuyama and Inatsu 2021) chunked into 1-h intervals; the VSVD was installed at the Sapporo site in winter 2017/18. We input the resultant v-D relationships into the SOM algorithm as the training data and we identified particle types by grouping the nodes into graupel and snow aggregates in the 4 × 4 SOM configuration. The new method enables us to automatically classify the precipitation particle types from disdrometers' data without any *prior* data.

The G/S ratio produced by the new method from the disdrometer's data at Sapporo was compared with that simulated by the model to show an application of the new method. The model reproduced the difference in the G/S ratio between Sapporo and Asahikawa, and the intra-seasonal variability of the G/S ratio. In the sensitivity test, we suggested that the training data should include a variety of solid precipitation types. To achieve this, we recommended using disdrometer data at a site with a temperature range from −15 °C to −5 °C at cloud altitudes at which the graupel generation tended to occur through riming processes. These sensitivity experiments demonstrated that our method allows for arbitrary adjustments to the size and grouping of SOM maps.

In this study, we constructed a 4 × 4 SOM map for classifying graupel and snow as an example of the application of our methodology. The 4 × 4 SOM map was suitable for this classification. However, a larger SOM map would be ideal for classifying any type of precipitation particle. Ideally, we require a sufficient number of observed particles to obtain a stable estimate from the EM algorithm for each type of precipitation and sufficient v-D relationship data estimated by the EM algorithm as input vectors of SOM map learning. This ideal case would enable more classifications of precipitation particle types and better discussion of variations in dominant physical processes among nodes. Nevertheless, in practical cases with limited data, the choice of SOM map size is restricted, thereby limiting the types of precipitation particles that can be classified. Future research could create an extensive reference SOM map if sufficient sample data became available. Therefore, by applying our method to data from disdrometers around the world, including traditional disdrometers, such as 2DVD, LPM, and the PARSIVEL disdrometer, it would be possible to evaluate the characteristics of precipitation particles automatically in any region and any season, understand precipitation trends, and potentially improve remote sensing and meteorological models. These applications are possible because our method gives the same results regardless of the kind of disdrometer used, provided that the particle size and fall velocity are measured correctly.

The 2-moment bulk scheme used in Chapters 2 and 3 was evaluated cloud microphysical processes of graupel. From the results in Chapters 2 and 3, it is concluded that this scheme effectively reproduced graupel, which plays a crucial role in riming growth and riming electrification. Therefore, in the next chapter, we utilized this scheme to investigate the mechanisms of rapid increase in lightning preceding downbursts.

3.7. Appendix

3.7.A. Fraction of variance unexplained

To show the goodness of fit for each node of the SOM map, the fraction of variance unexplained (FVU) is used to evaluate whether each node can explain the learning data (Akinduko et al. 2016; Clark et al. 2016). This index is calculated as

$\mathrm{FVU_i} = \mathrm{VAR_i}/\mathrm{VAR_{tot}}$, where VAR_i and VAR_{tot} are the variances of the residuals and the sample variance of the dependent variable in each node, respectively. Nodes with a high FVU have a large amount of error and the fitting is poor. The FVU was high for node #00, and we determined it as the error node. Node #15 also had a high FVU, probably because it included all curves with a faster rate of decline than the node #15 curve. In contrast, FVU was small for other nodes, suggesting successful classification.

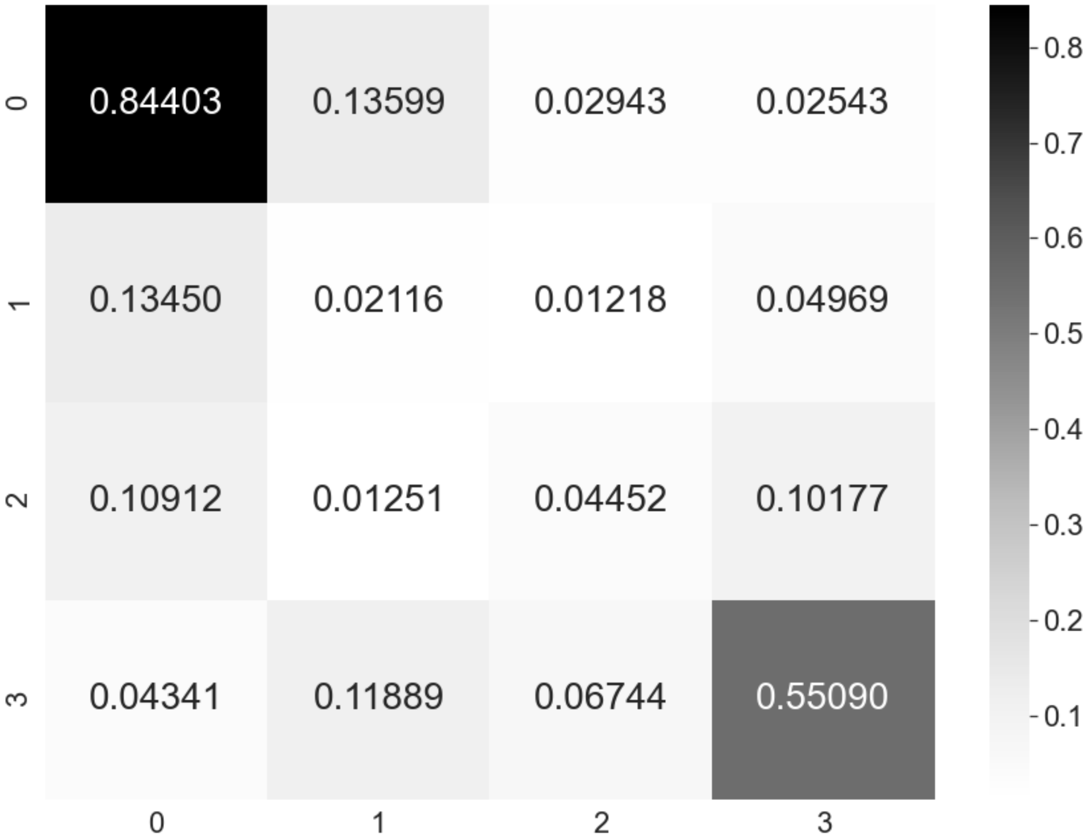

Fig. 3.A1. FVU for each node for the original SOM map (Fig. 3.2a).

3.7.B. Average number of particles for each node

Fig. 3.B1 shows the average number of particles in the learning data for each node. The number of particles in the learning data was small for node #00 compared with the required particle number of 2000 (Katsuyama and Inatsu 2020).

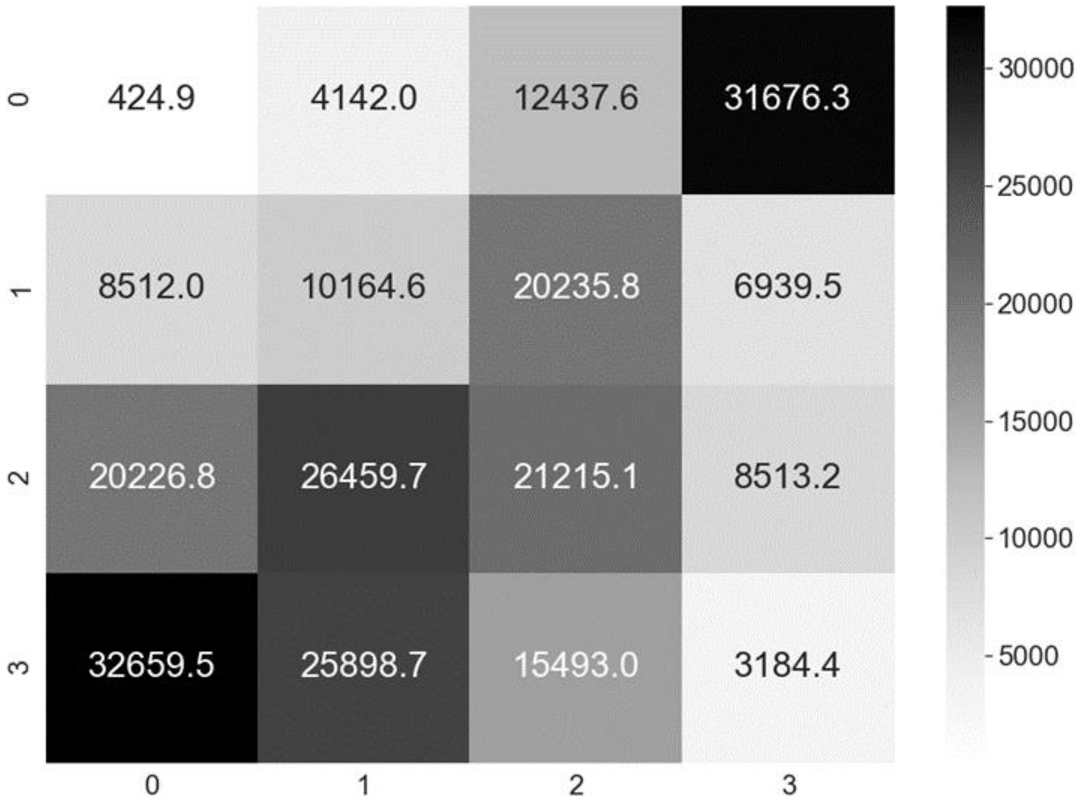

Fig. 3.B1. Average number of particles for each node based on the training data: mean for the period used in the G/S ratio calculation.

3.7.C. Range of simulated G/S ratio including 10 × 10 km area around the Sapporo observation site

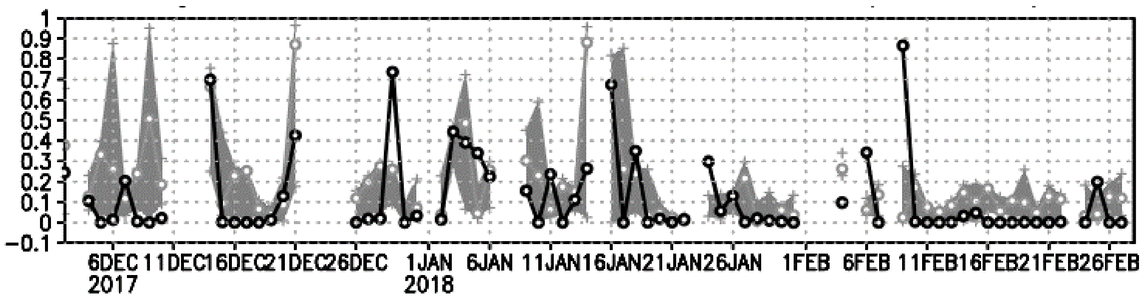

Fig. 3.C1. Temporal variation of G/S ratio. The black and gray lines show the results of the original and simulation, respectively. The gray shaded area for each day represents the range of the maximum and minimum G/S ratio in a 10 × 10 km area surrounding the observation site.

3.7.D. Sensitivity of the G/S ratio threshold

Figs. 3.D1–3.D3 show the frequency distributions of the G/S ratios in each month obtained by using thresholds of 0.1, 0.2, and 0.3. The model reproduced the frequency distributions of G/S ratio well with a threshold of 0.3. Changing the threshold value to 0.2 and 0.1 resulted in large discrepancies between the model and the observations, especially for the results in December with a threshold value of 0.1. These discrepancies mainly originated from the model limitations. The model simulates the solid precipitation for only three categories (i.e., ice, snow, and graupel) and it assumes a single *v-D* relationship for each category. In contrast, the characteristics of solid precipitation, such as shape, density, and *v-D* relationship, have larger variability than those in the model, and it is impossible for the model to reproduce the variability of the solid precipitation perfectly. The model limitations would make it difficult to reproduce the small G/S ratio in Sapporo in December. Based on these results, the threshold value of 0.3 was effective for separating the graupel-dominant precipitation considering the model limitations. Detailed analyses based on the threshold value of 0.1 and 0.2 will increase our knowledge for validating the model and will be conducted in future.

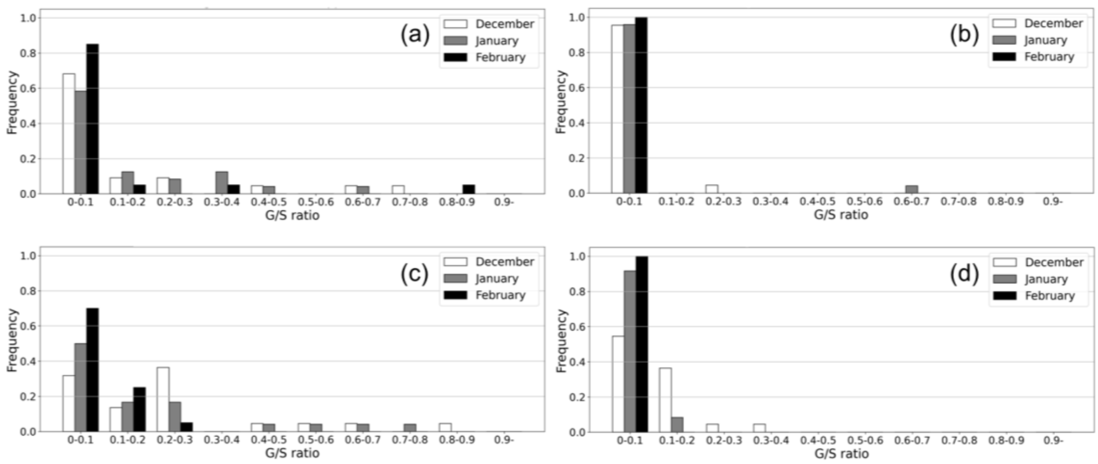

Fig. 3.D1. (a, b) Normalized frequency of the observed G/S ratio at (a) Sapporo and (b)

Asahikawa in (white) December, (gray) January, and (black) February. (c, d) Same as (a, b), but for the simulation. A threshold of 0.1 was used.

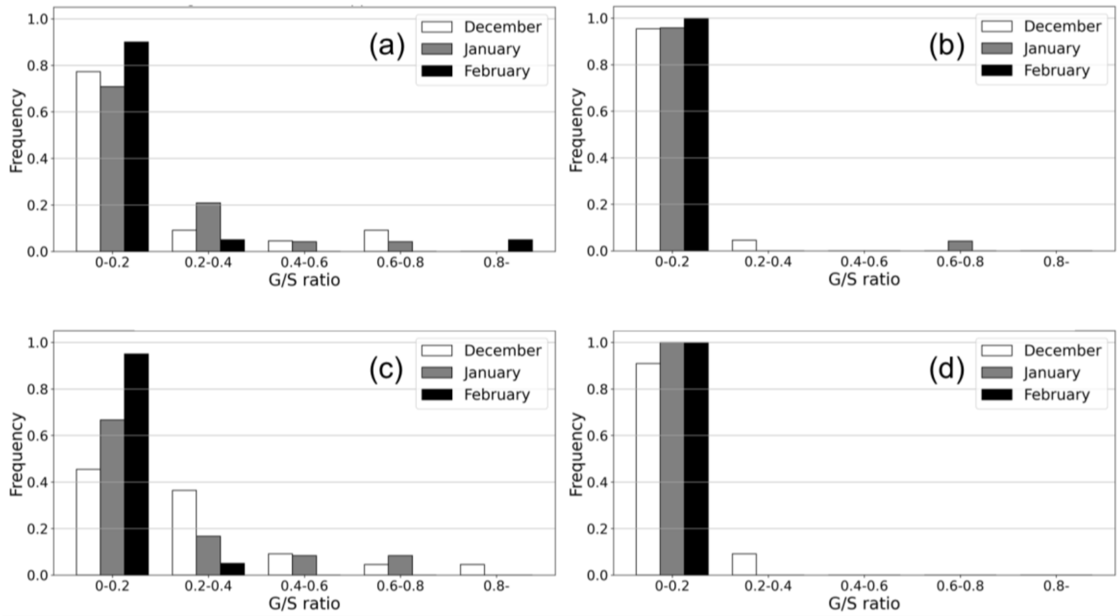

Fig. 3.D2. Same as Fig. 3.D1 but a threshold of 0.2 was used.

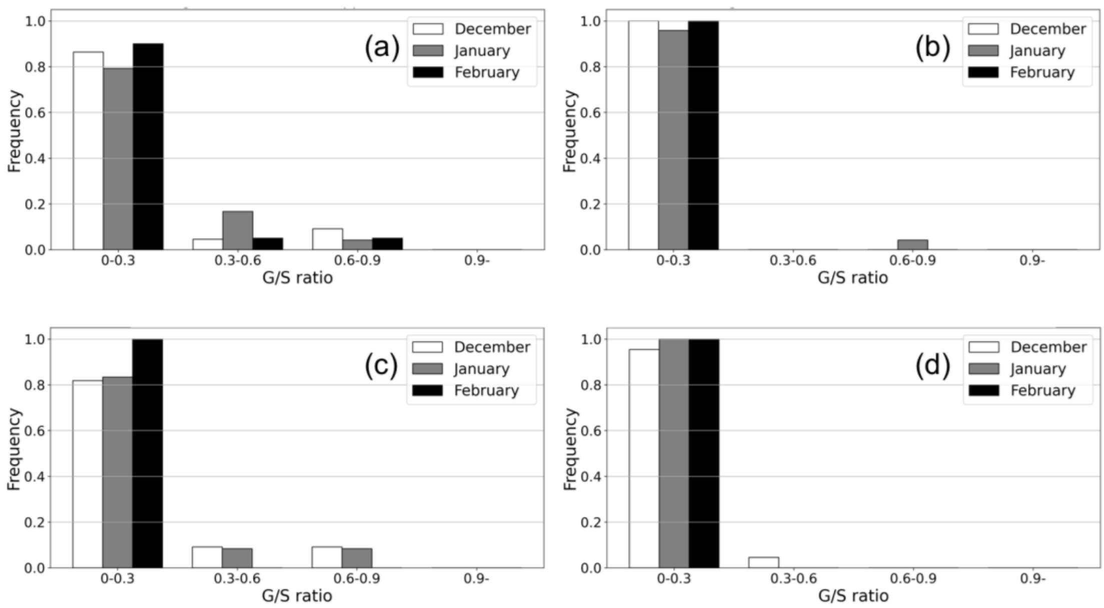

Fig. 3.D3. Same as Fig. 3.D1 but a threshold of 0.3 was used. (Same as Fig. 3.6).

Chapter 4. Transition of Dominant Cloud Microphysical Processes for Increasing Lightning Preceding Downbursts in Multi-cell Convective Clouds

4.1. Introduction

Solid and liquid particles in convective clouds grow mainly by collision (Pruppacher and Klett, 1997), which is more efficient for growth than is deposition or evaporation (Korolev, 2007). In deep convective mixed-phase clouds, solid particles can grow by collisions involving supercooled water, known as riming (riming growth), which produces dense solid particles such as graupel and hail (Pruppacher and Klett, 1997; Brdar and Seifert, 2017; List, 1961, 2014). The high-density solid particles produced by riming significantly influence the precipitation distribution due to their large terminal velocity compared to low-density solid particles, as their larger terminal velocities can lead to more localized and intense precipitation. (Bennetts and Rawlins, 1981; Fovell and Ogura, 1988; Gilmore et al., 2004), and they can intensify downdrafts near the surface via drag force and cooling by evaporation, sublimation, and melting. According to previous reports, such downdrafts can sometimes result in appreciable downbursts with wind velocities exceeding 3.66 m s^{-1} at 91.4 m above the surface (Fujita and Byers, 1977; Fujita, 1985; Wakimoto, 1985; Wilson et al., 1984; Hjelmfelt, 1988; Fujita, 1992; Wilson and Wakimoto, 2001).

Another distinctive cloud microphysical process related to collisions in deep convective mixed-phase clouds is charge separation through riming electrification, which was reported originally in laboratory experiments (e.g., Takahashi, 1978; Saunders et al., 1991). Riming electrification occurs through the collision and rebound of rimed ice crystals or graupel with ice or snow particles (Takahashi, 1978; Saunders et al., 1991), and it is supported by sonde observations of charge distributions in convective clouds (Takahashi et al., 1999, 2019; Rust, 1989; MacGorman and Rust, 1998) and remote-sensing observations (Zheng et al., 2019; Brook et al., 1982; Kumjian and Deierling, 2015). Riming electrification is one of the main processes for charge generation in thunderstorms, and the charged particles generated via charge separation can lead to lightning.

The above background indicates that riming growth and riming electrification induce the occurrence of severe disastrous weathers such as heavy rainfall, hailstorms, downbursts, and lightning, which can be disastrous. By gaining a detailed understanding of these cloud microphysical processes in mixed-phase convective clouds, it becomes possible to improve predictive models and develop more effective early warning systems, ultimately mitigating the impacts of such disasters.

To find a precursor of severe weathers that bring disastrous consequences, the relationship between lightning and severe weather has been examined recently. Lightning frequency increases rapidly preceding severe weather related to riming growth, such as heavy rainfall, hail, and downbursts (e.g., Goodman et al., 1988; Williams et al., 1999; Schultz et al., 2009, 2011). Sometimes called a lightning jump (LJ) (Goodman et al., 1988; Williams et al., 1999; Schultz et al., 2009, 2011, 2017), this rapid increase in lightning frequency is used to predict severe weather events (e.g., Schultz et al., 2009, 2011; Farnell and Rigo, 2020; Gatlin and Goodman, 2010, Erdmann and Poelman, 2023). Combined analyses of radar and lightning observations have contributed considerably to understanding the relationship between severe weather and LJs; these include North

Alabama Lightning Mapping Array (NALMA; Koshak et al., 2004; Goodman et al., 2005), National Lightning Detection Network (NLDN; Orville, 2008), Earth Networks Total Lightning Network (ELNTN; Heckman, 2014), LIghtning DEtection Network system (LIDEN; Ishii et al., 2014), Lightning Map Array (LMA; Proctor, 1971), Broadband Observation network for Lightning and Thunderstorm (BOLT; Yoshida et al., 2014), Geostationary Lightning Mapper (GLM; Goodman et al., 2013), Meteosat Third Generation Lightning Imager (MTG LI; Dobber and Grandell, 2014), and the lightning mapping imager (Yang et al., 2017). Schultz et al. (2015, 2017) investigated the kinematic and cloud microphysical characteristics of LJs by using the three-dimensional bulk characteristics of particle types and fall velocities retrieved from Advanced Radar for Meteorological and Operational Research (ARMOR; Knupp et al., 2014) and KHTX radar data, as well as total lightning data from NALMA. Schultz et al. (2015) examined the relationship between LJs and the trends in mixed-phase graupel mass, maximum updraft velocity, and updraft volume, and they reported that LJs occurred when the updraft volume whose velocity reached $10\ \mathrm{m\ s^{-1}}$ and the mixed-phase graupel mass increased. Schultz et al. (2017) subjected the relationship reported by Schultz et al. (2015) to statistical analysis and reported that updraft volume is a suitable condition for triggering LJs. The relationship between updrafts and lightning frequency is well established, as updrafts exceeding $10\ \mathrm{m\ s^{-1}}$ lead to an increase in the number concentration of ice particles aloft (Dye et al., 1986; Schultz et al., 2015) and result in both active riming and riming electrification within the updraft areas of deep convective clouds.

However, there is scope for further investigation into the relationship among lightning frequency, graupel mass, and updraft intensity. Deierling (2008) reported a tenfold difference in total lightning frequency for clouds with similar graupel masses, and several other studies have reported that lightning originating from riming electrification tends to occur in areas where hail produced by the riming growth is absent. Known as lightning holes (Krehbiel et al., 2000; MacGorman et al., 2005; Emersic et al., 2011; Ni et al., 2023), such areas have been observed in supercell cases with mesocyclones (Krehbiel et al., 2000; MacGorman et al., 2005) and other thunderstorm cases (Emersic et al., 2011). The clouds that produce lightning holes suggest that the lightning holes are governed by not only the kinematic structure of the clouds but also their microphysical processes. Emersic et al. (2011) indicated that the occurrence of lightning holes could be due to the environment conducive to riming growth of hail being unsuitable for charge separation, based on observations from the National Weather Radar Testbed Phased-Array Radar.

These reports from previous studies imply that the whole complicated relationship among hydrometeors (including supercooled water, ice, snow, graupel, and hail), riming growth, riming electrification, and other cloud microphysical processes should be considered in order to comprehend the relationship between lightning and severe weather.

Observational studies that used the characteristics of graupel and lightning as proxies for the cloud microphysical properties of mixed-phase areas have provided valuable insights into the mechanisms behind LJs. However, there are challenges associated with using radar observations to analyze the cloud microphysics of mixed-phase areas. While radar can capture the entire cloud and identify particle characteristics within it using hydrometeor classification methods (Park et al., 2009; Dolan et al., 2013), it struggles to accurately represent the coexistence of ice and liquid water particles, which is crucial in mixed-phase regions. Consequently, understanding the physical processes within mixed-phase clouds—where riming growth and riming electrification either coexist or conflict—is essential to clarify their mechanisms and advance our knowledge of cloud microphysical processes and their effects on LJs.

Numerical studies using meteorological models have advantages for analyzing mixed-phase clouds because simulating the latter in this way offers dense three-dimensional data that can represent the coexistence of solid and liquid particles in mixed-phase areas. Additionally, by utilizing meteorological models coupled with bulk lightning models (BLMs) (Sato et al., 2019; Fierro et al., 2013; Barthe et al., 2012), we can investigate mixed-phase areas conducive to lightning and downbursts. In a BLM, the charge separation processes are calculated explicitly from the collision and rebound processes between graupel and snow within cloud microphysical schemes based on riming electrification (Takahashi, 1978; Saunders et al., 1991), and the electric field generated by the calculated charge distribution can be used to represent lightning as the neutralization of these charge imbalances. Meteorological models coupled with BLMs enable the investigation of complex charge distributions within convective clouds based on dynamical and cloud microphysical processes including riming growth and riming electrification (Chen et al., 2020; Sato et al., 2019, 2022). Recent studies have utilized meteorological models coupled with BLMs to examine the correlation between severe weather and lightning activity. Luque et al. (2023) investigated the correlation between severe weathers in convective clouds and lightning activity observed during field campaigns using Weather Research and Forecasting with the ELECtrification (WRF-ELEC; Fierro et al., 2013); however, that study was focused on identifying good proxies for LJs, such as hail and strong wind, rather than analyzing the physical mechanisms between hail and lightning activity such as an LJ.

The aim herein is to suggest a possible mechanism for an LJ, characterized by the rapid increase of lightning flash rate associated with riming electrification, which precedes the downburst associated with riming growth in mixed-phase clouds. To achieve this, we use a meteorological model coupled with a BLM.

4.2. Data and Methods

4.2.1. Target case

To achieve the aims of this study, idealized experiments were conducted focusing on the downburst that occurred in Misato Town in Saitama Prefecture in Japan on 8 September 1994, a day that saw the occurrence of multi-cell convective clouds involving multiple downbursts and lightning (Takayama et al., 1997). As the first step, we selected multi-cell convective clouds because with them the correlation between LJs and downbursts is stronger than with isolated convective clouds (Rigo and Farnell, 2022).

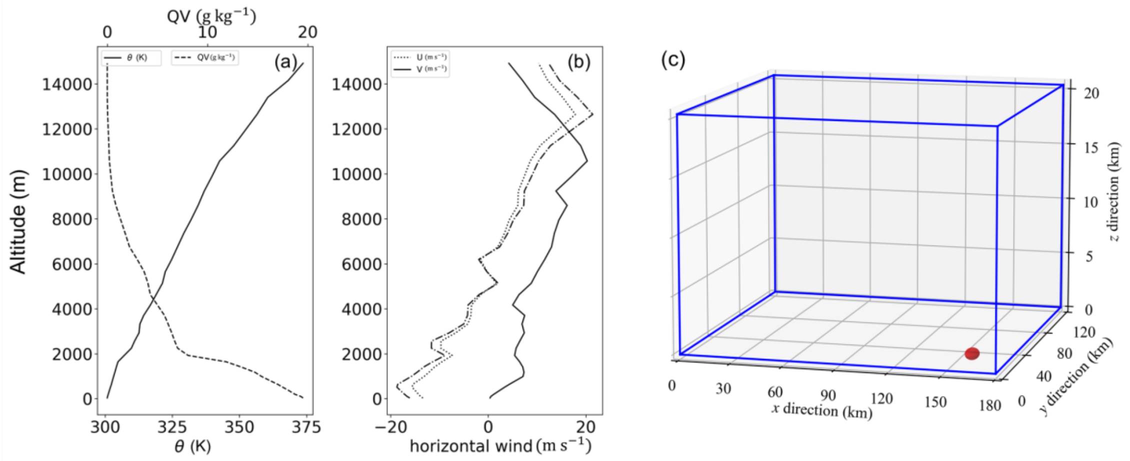

Fig. 4.1. (a,b) Initial profiles for idealized experiment: (a) potential temperature (solid line) and vapor mixing ratio (dashed line); (b) horizontal wind speed in *x* direction (dotted line) and *y* direction (solid line), and zonal wind component in strong shear (SS) experiment (dash-dotted line). (c) Model domain for the numerical experiments (rectangular prism surrounded by blue lines) and location of initial the warm bubble (red area).

4.2.2. Model description and experimental setup

Idealized experiments were conducted using the SCALE (Scalable Computing for Advanced Library and Environment) (Nishizawa et al., 2015; Sato et al., 2015) meteorological model coupled with a BLM (Sato et al., 2019). The BLM calculates the charges of cloud hydrometeors as prognosis variables: the riming electrification is calculated using a look-up table based on Takahashi (1978), and the flash origin density (FOD) corresponding to flash frequency is calculated using the neutralized scheme by Fierro et al. (2013); see Sato et al. (2019) for the details of the BLM. A two-moment bulk cloud microphysical scheme (Seiki and Nakajima, 2014), the Smagorinsky-type sub-grid model (Smagorinsky, 1963), and a Mellor–Yamada-type planetary boundary layer scheme (Nakanishi and Niino, 2004, 2009) were applied, and the radiation was ignored. The cloud microphysical scheme represents cloud hydrometeors by the five categories of cloud, rain, cloud ice, snow, and graupel. The hail category is not treated by the model, but the drag force accompanied with falling heavy solid hydrometeors can be reproduced by heavy graupel. The calculation domain covered 180 km × 120 km in the x and y directions, respectively, with 100-m horizontal grid spacing with doubly periodic boundary conditions, and 100 vertical layers with gradually increasing layer thickness from 10 m to 1578 m (the model top is 20.4 km) were used (Fig. 4.1c). The calculation time was 90 min, and the output interval was 20 s. Rayleigh damping was imposed above 15,000 m, and a free-slip surface boundary was adopted.

The horizontally uniform initial vertical profiles of potential temperature, water vapor mixing ratio, and horizontal wind were obtained from sounding data measured at Maebashi and Tateno, with the data from Tateno used to supplement the lack of wind data at Maebashi on the day described in Section 4.2.1 (Guo et al., 1999) (Figs. 4.1a,b), and the surface pressure was set as 992.8 hPa at the initial time. We conducted two experiments to investigate the relationship between lightning activity and downburst. The control (CTL) experiment was conducted using the initial vertical profiles of the original sounding data (Guo et al., 1999). For the sensitivity experiment [strong shear (SS) experiment], only the horizontal wind shear in the x direction was increased by 20% from its vertical profile used in the CTL experiment (dash-dotted line in Fig. 4.1b).

To trigger convection, a potential-temperature perturbation θ' defined by Eq. (4.1) based on Miyamoto (2021) was inserted at (x, y, z) = (160, 20, 0.5) km in the calculation domain, where the origin is set at the southwest corner of the domain at the initial time:

$$\theta'(x,y,z) = \begin{cases} \theta_{wb}\cos(\frac{\pi}{2}\sqrt{l_{\mathrm{wbh}} + l_{\mathrm{wbz}}}), \text{for } \sqrt{l_{\mathrm{wbh}} + l_{\mathrm{wbz}}} \leq 1.0, \\ 0, \qquad \text{for } 1.0 < \sqrt{l_{\mathrm{wbh}} + l_{\mathrm{wbz}}}, \end{cases} \tag{4.1}$$

where θ_{wb} is the amplitude of θ', and we have $l_{\mathrm{wbh}} = (r_{\mathrm{wbh}}/r_{\mathrm{wbz}})^2$ and $l_{\mathrm{wbv}} = (r_{\mathrm{wbz}}/r_{\mathrm{wbh}})^2$, where r_{wbh} and r_{wbz} are the horizontal and vertical distances from the bubble center, respectively. In both experiments, we set θ_{wb} = 4 K, r_{wbh} = 4 km, and r_{wbz} = 1 km.

4.2.3. Definitions of lightning increase preceding downburst corresponding to lightning jump and heavy graupel

Various algorithms have been proposed for defining LJ： the 2σ LJ algorithm for the increase in lightning frequency every 2 min (Schultz et al., 2009, 2011; Farnell and Rigo, 2017), and the Relative Increase Level algorithm for the Geostationary Lightning Mapper, which calculates simple lightning frequency increments (Erdmann and Poelman, 2023). However, these LJ algorithms require thresholds for the target severe weather, and these LJ thresholds depend on observational instruments. Also, it is not easy to apply these algorithms to the output of the model, so we simply defined a preceding lightning increase (PLI) corresponding to an LJ as an increase in lightning activity continuing for at least 5 min preceding the occurrence of a downburst. This PLI definition is not equivalent to those used in previous studies, which aimed to evaluate lead times and warning accuracy for severe phenomena. The PLI defined in this study does not focus on predictive accuracy but rather emphasizes the preceding relationship between lightning activity and downbursts. In addition, Shultz et al. (2011) reported that total lightning, which is the sum of cloud-to-ground and intra-cloud discharges, is a superior LJ indicator, so we used FOD as the lightning frequency, which corresponds to total lightning in the model.

For analyzing the downburst, we focused on the heavy graupel simulated by the model, which corresponds to hail in nature. Simulated graupel with the averaged particle mass exceeded 50 mg was classified as heavy graupel in this study. The averaged particle mass; m_g was calculated as $m_g = \rho Q_g / N_g$, where $\rho, Q_g,$ and N_g are respectively the graupel density, mass mixing ratio, and number concentration predicted by the model.

4.2.4. Analysis of convection tilting, horizontal flux, and vertical flux

To investigate the influence of wind circulation, we examined the impacts of liquid water supply from lower layers on the riming growth and the supply of solid hydrometeor particles from the surrounding area on the riming electrification according to the vertical mass flux of liquid water (WQ_{liq}) and the horizontal flux of the snow number concentration (UN_S), respectively. The quantities UN_S and WQ_{liq} are defined as

$$UN_S = U_{\mathrm{horiz}} N_S, \tag{4.2}$$

where N_S is the number concentration of snow and U_{horiz} is the absolute horizontal wind velocity, and

$$WQ_{\mathrm{liq}} = W\rho(q_R + q_C), \tag{4.3}$$

where q_R and q_C are the mixing ratios of rain and cloud water, respectively, and W is the vertical wind velocity.

The convection tilting angle φ_{tilt} is calculated as

$$\varphi_{\text{tilt}} = \arctan\left(\frac{W}{U_{\text{horiz}}}\right) \left(-\frac{\pi}{2} \leq \varphi_{\text{tilt}} \leq \frac{\pi}{2}\right). \tag{4.4}$$

In this study, convection with $\varphi_{\text{tilt}} > \frac{5}{18}\pi$ is defined as upright convection, that with $\varphi_{\text{tilt}} < \frac{\pi}{6}$ is defined as tilted convection, and that with $\frac{\pi}{6} < \varphi_{\text{tilt}} \leq \frac{5}{18}\pi$ is defined as moderate tilted convection.

Also, to interpret the results from the present numerical experiments on multi-cell convective clouds, we use the parameter $C/\Delta U$ (Rotunno et al., 1988; Weisman and Rotunno, 2004; Takemi, 2006; Lebo and Morrison, 2014), where C and ΔU represent cold pool intensity and vertical wind shear, respectively. This parameter was introduced by previous studies (Rotunno et al., 1988; Weisman and Rotunno, 2004) as part of the Rotunno–Klemp–Weisman (RKW) theory in order to discuss optimal convection structures, and it was reported that $C/\Delta U \sim 1$ and $C/\Delta U \gg 1$ are optimal conditions for upright convection and tilted convection, respectively, at the leading edge of the cold pool. Therefore, we calculated $C/\Delta U$ for our results to examine suitable environments for tilted or upright convection, with C, B, and ΔU defined as follows (Takemi, 2006):

$$C^2 = \int_0^H (-B)dz, \tag{4.5}$$

$$B = g\left(\frac{\theta-\overline{\theta}}{\overline{\theta}} + \left(\frac{R_v}{R_d}\right)(q_v - \overline{q_v}) - q_{hyd}\right), \text{ and} \tag{4.6}$$

$$\Delta U = U_{\text{horiz},z=H} - U_{\text{horiz},z=0}\,, \tag{4.7}$$

where g is the acceleration due to gravity, θ is the potential temperature, q_v is the water vapor mixing ratio, q_{hyd} is the total hydrometeor mass mixing ratio defined as the sum for all hydrometeor categories, B is buoyancy, R_d is the gas constant for dry air, R_v is the gas constant for water vapor, and H is the cold pool thickness. H = 5 km, as referenced in Takemi (2006). Overbars indicate the model's basic state defined as domain-averaged variables.

4.3. Results

4.3.1. Representation of downbursts and increases in lightning frequency

First, we show the general characteristics of the simulated multi-cell convective clouds. The snapshot of precipitation distribution in Appendix 4.6.A indicates that the precipitation produced by the convective clouds was generated repeatedly and lasted until the end of the simulation, which is a typical characteristic of long-lasting multi-cell convective clouds. As well as the strong precipitation exceeding 100 mm h^{-1} with downdraft exceeding 10 m s^{-1} near the altitude of 90 m, wind speeds exceeding 40 m s^{-1} corresponding to a downburst occurred multiple times in both experiments (shown as the black line in Figs. 4.2c and 4.2d). In this study, the first convective cloud initiated by the warm bubble at the initial time (Eq. 4.1) was not considered when examining the multi-cell convective clouds triggered by a cold pool, and therefore we analyzed the results after 24 min.

In the CTL experiment, the lightning frequency increased and reached a local maximum at around 33.3 min (the red line in Fig. 4.2c), which is 14.7 min before the downburst at 48 min (the black line in Fig. 4.2c). The sequence of increasing lightning frequency followed by a downburst was identified as the occurrence of a PLI corresponding to an LJ based on its definition in Section 4.2.3. Furthermore, strong winds exceeding 40 m s^{-1} also occurred at around 61 min and 72 min (the black line in Fig. 4.2c), but these downbursts were not preceded by increasing lightning frequency, corresponding to downbursts without PLIs. These results indicate successful representation of long-lasting multi-cell convection and downbursts with and without PLIs in the CTL experiment.

The successful representation of downbursts with and without PLIs enabled us to examine the mechanism contributing to PLI occurrence. We investigated heavy graupel particles and charge separation as precursors of downbursts and lightning. Table 4.1 summarizes the times of maximum charge separation (shown in Fig. 4.2e) and local maximum number concentration of heavy graupel particles around the time of local maximum charge separation. In the CTL experiment, active charge separation occurred at around 33.3 min (the pink line in Fig. 4.2e), which was attributed to the positive charge separation of graupel around the height of 7000 m (the pink contour lines in Fig. 4.2a). This active charge separation generated the large charge density of the hydrometeors and resulted in increased lightning frequency (the red line in Fig. 4.2c). Before the downburst at around 48 min, an increase in heavy graupel particles generated around the height of 4500m (the region filled with solid colors in Fig. 4.2a), was seen at 40 min, which was 8 min before the downburst (the purple line in Fig. 4.2c). These results indicate that the downburst at 48 min was produced by the drag force and evaporative/sublimation cooling below the clouds caused by the heavy graupel particles.

In the SS experiment, the vertical distribution of the active charge separation area and the area of the active production of heavy graupel particles (Fig. 4.2b) were consistent with those in the CTL experiment (Fig. 4.2a), but the magnitude of the charge separation was smaller than that in the CTL experiment. In addition, a local maximum of heavy graupel particles (30 min) and strong wind regarded as a downburst (33 min) occurred before the increase in charge separation and lightning frequency (36.6 min) (Figs. 4.2b and 4.2f). This means that PLIs were absent in the SS experiment.

Table 4.1. Times of local maxima of charge separation amount and the number of heavy graupel particles in CTL and SS experiments after 24 min from the initial time.

	CTL exp.	SS exp.
Charge separation	33.3 min	36.6 min
Heavy graupel particle number	40.0 min	30.0 min

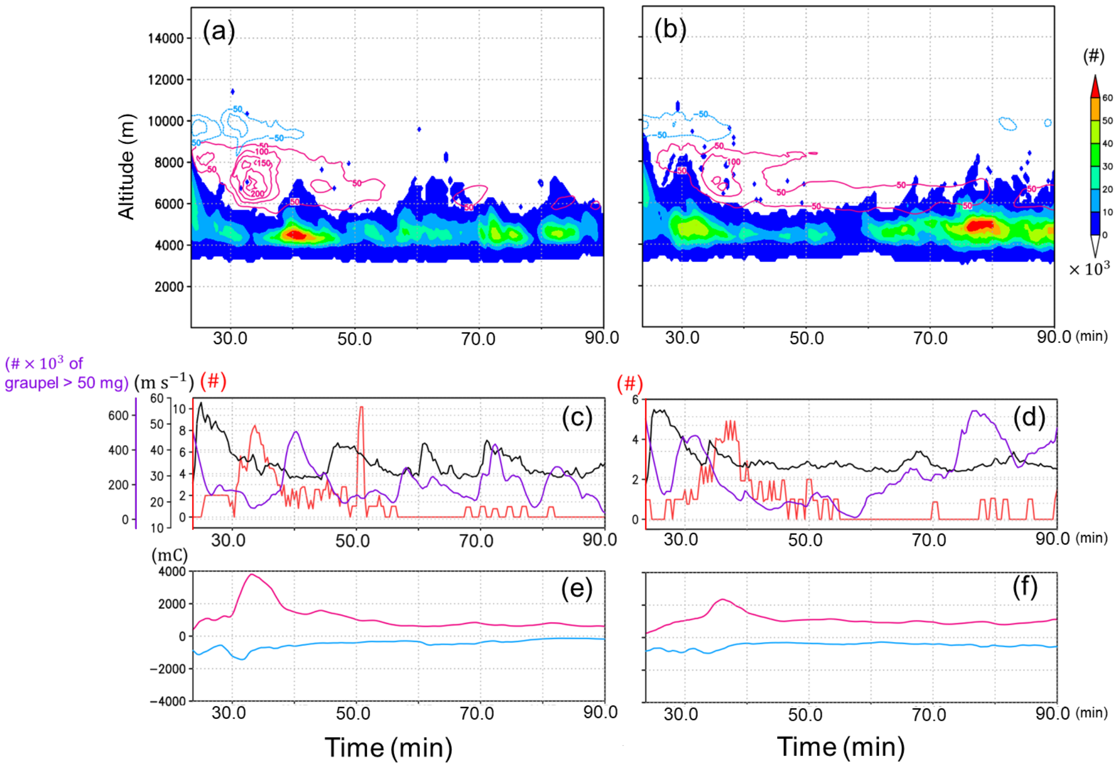

Fig. 4.2. (a,b) Time series of region filled with solid colors represents accumulated number of graupel particles exceeding 50 mg. (#), The red and blue contour lines show accumulated positive and negative charge separations of graupel (mC), respectively. (c,d) Black, red, and purple lines represent maximum wind speed, cumulative flash origin density, and total number of graupel particles exceeding 50 mg within the model domain, respectively. (e,f) Pink and blue lines represent accumulated positive and negative charge separation of graupel. (a), (c), and (e) show the results for CTL experiment and (b), (d), and (f) show the result for the SS experiment.

4.3.2. Environment During PLIs and Active Generation of Heavy Graupel Particles

Next, we investigate the environment during PLIs and the active generation of heavy graupel particles to understand the differences in the physical mechanisms contributing to active charge separation and active growth of such particles. To investigate these mechanisms, we focus on the mixed-phase area, where liquid and solid hydrometeors coexist in convective clouds.

Figure 4.3 shows how the area in which charge separation occurs and the area with heavy graupel particles are distributed over a vertical cross-section through convective clouds, with each panel showing a snapshot at the time of either active charge separation (33.3 min in the CTL experiment and 36.6 min in the SS experiment) or active growth of heavy graupel particles (40.0 min in the CTL experiment and 30 min in the SS experiment). Fig. 4.3 enables consideration of the cloud microphysical and electrical properties in the mixed-phase area, together with the zoom-in panels (Fig. 4.4). At the time of active charge separation in the CTL experiment, snow and cloud ice, graupel, and liquid water (supercooled water), marked with blue, green, and orange hatching, respectively, coexisted over the area with active charge separation (138 km $< x <$ 145 km, 5000 m $< z <$ 9000 m; Figs. 4.3a and 4.4a). During this period, lightning activity increased, and no heavy graupel particles (purple hatching) were simulated in this area.

In contrast, at the time of active growth of heavy graupel particles, liquid water and graupel (orange and green hatching, respectively) coexisted, but snow and cloud ice (blue hatching) were not seen over the area with production of heavy graupel particles (purple hatching; 130 km $< x <$ 132 km, 4500 m $< z <$ 6000 m; Figs. 4.3b and 4.4b). The downburst at 48 min was produced by the drag force and evaporative/sublimation cooling below the clouds caused by the heavy graupel particles produced in this area (figure not shown).

The results of the SS experiment indicated similar trends as in the CTL experiment, such as the occurrence of charge separation (Figs. 4.3d and 4.4d; 135 km < x < 145 km, 6000 m < z < 9000 m) and the production of heavy graupel particles (Figs. 4.3c and 4.4c; 135 km < x < 142 km, 4000 m < z < 6000 m).

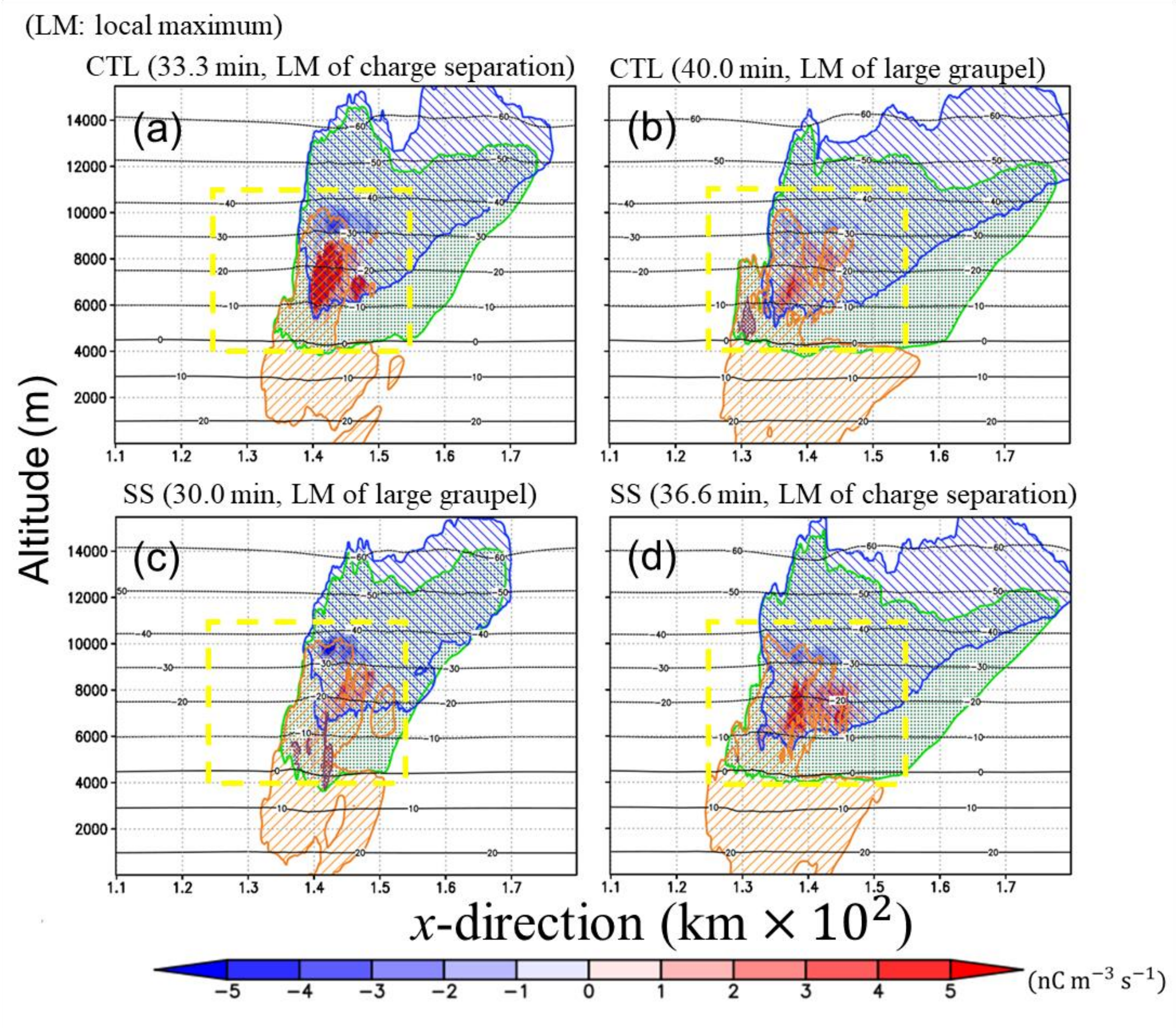

Fig. 4.3. The *x-z* cross-sections for the results of accumulated over the *y* gridpoints where a total hydrometeor mixing ratio exceeds 0.1 g kg^{-1} and a charge separation exceeds 0.5 nC m^{-3}, for the snapshot at (a) 33.3 min and (b) 40.0 min from the initial time of the CTL experiment and the snapshot at (a) 30.0 min and (b) 36.6 min in the SS experiment. The orange hatches, green dots, and blue hatches respectively indicate liquid water, graupel, and snow and cloud ice exist. The purple hatches indicate areas where the number of heavy graupel particles exceeds 500 m^{-3} in the accumulation. The black contours denote air temperatures (°C). The yellow dashed box is a zoom-in domain of Fig. 4.4.

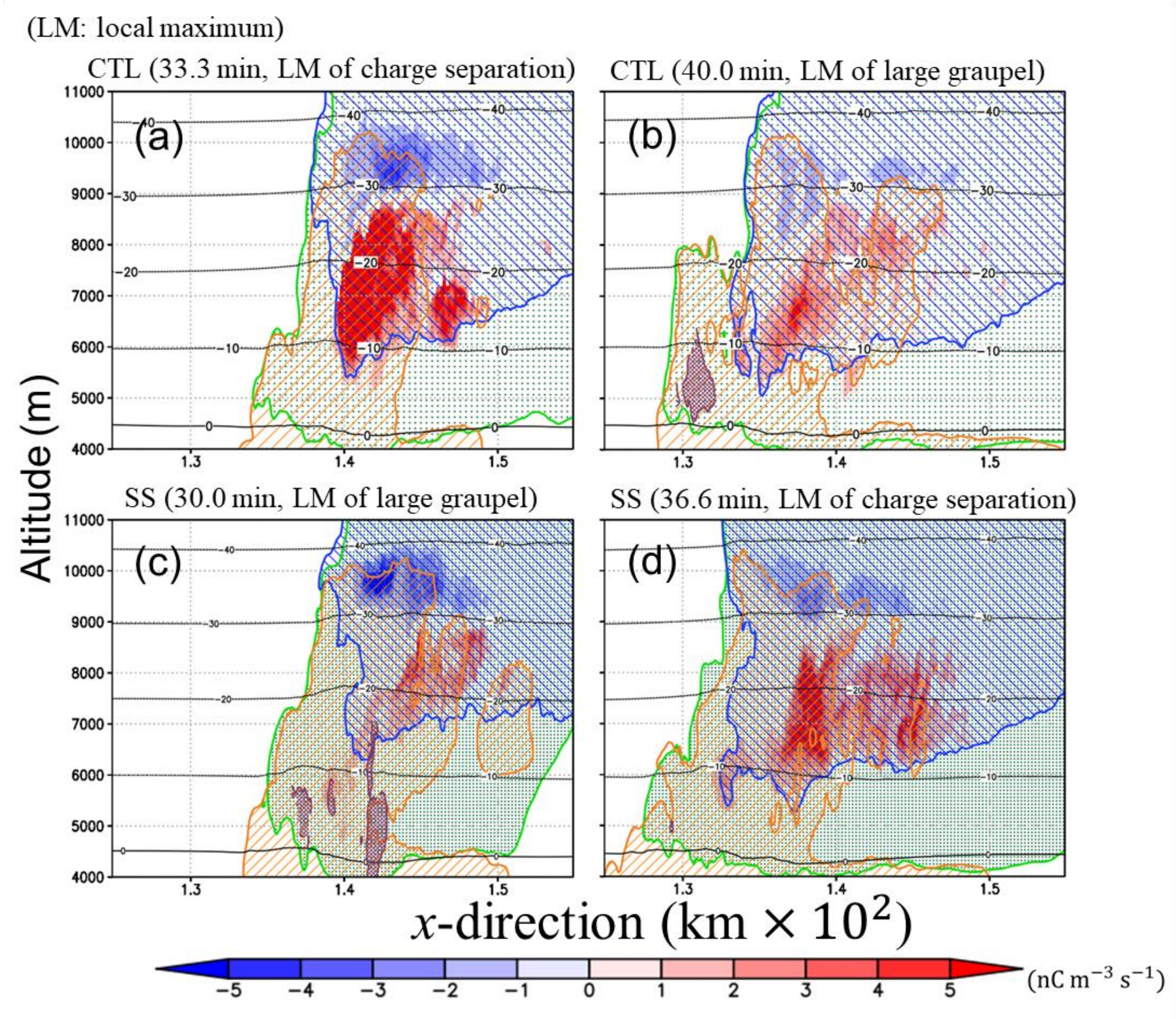

Fig. 4.4. The zoom-in figure for the yellow dashed box in Fig. 4.3.

To examine the reason for the different characteristics at the times of active charge separation and active growth of heavy graupel particles, we analyzed the wind flow around the mixed-phase area. Figure 4.5 shows vertical cross-sections of charge separation amount with streamlines at the times of active charge separation and active growth of heavy graupel particles. It also indicates the areas with heavy graupel particles (purple hatching), strong vertical velocity exceeding 25 m s^{-1} (orange hatching), and negative velocity in the *x* direction (green hatching). In the CTL experiment at the time of active charge separation (33.3 min), the area of active charge separation (138 km < x < 145 km, 5000 m < z < 9000 m) was located behind the convective area (Figs. 4.5a and 4.5b). In the area of active charge separation, the horizontal wind blew toward the area with active riming electrification (green hatching in Figs. 4.5a and 4.5b; 140 km < x < 150 km, 6000 m < z < 8000 m) from the rear side of the convective cloud; the horizontal wind toward this area from the rear side of the convective cell corresponds to a rear inflow jet (Fan et al., 2017; Weisman and Rotunno, 2004). Similar trends were simulated in the SS experiment (green hatched area in Figs. 4.5g and 4.5h; 140 km < x <150 km, 6000 m < z < 8000 m), but the charge separation amount was smaller than that in the CTL experiment.

In contrast, at the time of active growth of heavy graupel particles in the CTL experiment, the area with heavy graupel particles coincided with the area of strong updrafts, and the horizontal wind flow from the rear side of the convection was not included in the area with heavy graupel particles. Furthermore, the area with heavy graupel particles (Figs. 4.5c and 4.5d; $x \approx 130$ km) was located around the area with strong vertical wind. However, that area was distinct from the area with updrafts exceeding 25 m s^{-1} (132 km < x < 138 km) located behind it. This indicates that the strong updraft at $x \approx 130$ km was a new convective cell generated by the convergence and divergence at the surface by cold pools produced by the preceding convective cell seen at 132 km < x < 135 km. In the SS experiment, heavy graupel particles were produced in the area where $x \approx 142$ km and 4000 m < z < 6000 m (Figs. 4.5e and 4.5f).

The above analyses clarify that a horizontal wind from the rear side of the convective cell is prominent during the periods of active riming electrification. This horizontal wind from the rear side of the convective cell transported solid particles such as snow and cloud ice to the area containing graupel and liquid water, thereby generating an environment in which graupel, snow, and liquid water coexisted. Under this environment, the charge separation by the riming electrification occurred actively (See Appendix 4.6.B).

On the other hand, in the area of active heavy-graupel growth, updrafts were dominant, and this vertical flow supplied much liquid water from the lower layers. In addition, the horizontal wind from the rear side of the convective cell was either weak or absent altogether, and few solid particles were supplied from the surroundings. In such conditions, an environment where only graupel and liquid water coexisted was produced. Under this environment, the riming growth of graupel was active, but the riming electrification was not active because of the absence of snow and cloud ice. As a result, heavy graupel particles were generated actively through riming growth.

To summarize the above, the environment that was suitable for riming electrification, which leads to PLIs, was formed by the horizontal wind from the rear side supplying snow and cloud ice to the convective cell. Conversely, the production of heavy graupel particles contributing to downbursts grew efficiently in the environment where the riming growth of graupel was active because of the absence of solid particles and the active supply of liquid water.

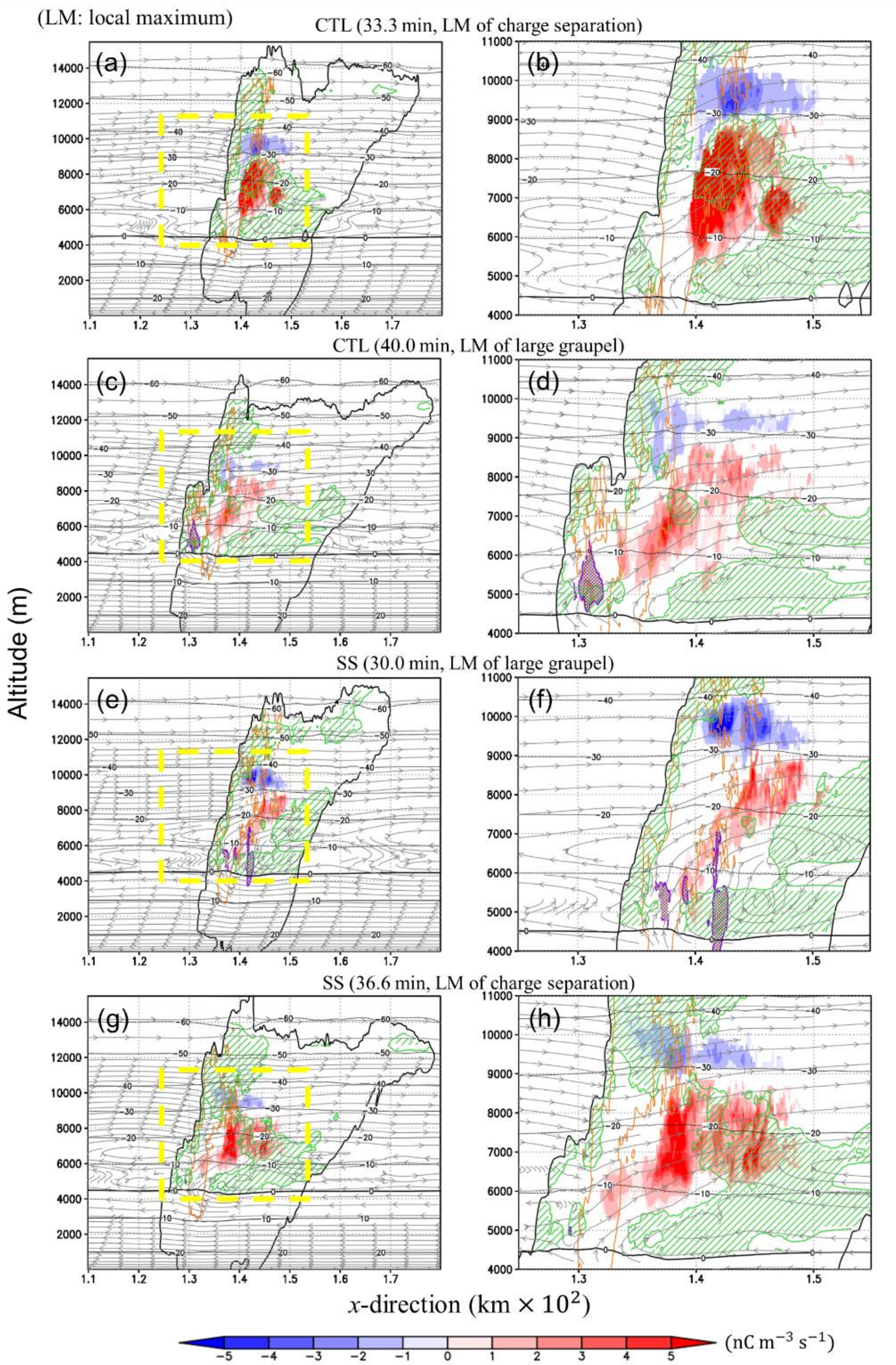

Fig. 4.5. Vertical cross-sections in x direction at times of local maxima of charge separation and heavy graupel particles for each experiment. The yellow dashed box in (a, c, e, g) is the area that is enlarged in (b, d, f, h). The shading represents the charge

separation averaged in the y direction and indicates where it exceeded 5 nC m^{-3}. The thick black line encloses the area where the total condensate averaged in the y direction exceeded 10^{-1} g kg^{-1}, while the orange line indicates the area where the maximum vertical wind speed in the y direction exceed 25 m s^{-1}. The gray lines with arrows are the streamlines of the wind. The green hatched area is that where the horizontal wind was positive (horizontal wind minus initial horizontal wind > 0 m s^{-1}), flowing from the convective-cloud rear side in the x direction. (a–d) and (e–h) show the results from the CTL and SS experiments, respectively. (a, b) and (c, d) show the results at 33.3 min and 40 min in the CTL experiment, respectively, and (e, f) and (g, h) show the results at 40 min and 36.6 min in the SS experiment, respectively.

To extend the above analyses to the whole period of the simulation, we investigate the horizontal wind flux of snow number concentration and the vertical flux of liquid water mass as proxies for the supply of solid particles such as snow and ice and the riming growth area. Figure 4.6 shows the horizontal wind flux of snow number concentration against the total number of heavy graupel particles (Figs. 4.6a and 4.6c) and the positive charge separation of graupel (Figs. 4.6b and 4.6d). The heavy graupel particles existed predominantly when the horizontal flux of snow number concentration was small ($UN_S < 10^{-2}$ m^{-2} s^{-1}) (Figs. 4.6a and 4.6c). The timing of this small UN_S is synchronised with that of the generation of heavy graupel particles in the CTL experiment but not in the SS experiment (Figs. 4.7a–4.7d). In contrast, charge separation of graupel occurred in the area where the horizontal flux of snow number concentration was active ($> 10^7$ m^{-2} s^{-1}) (Figs. 4.6b and 4.6d). The frequency of this area of large UN_S showed a good correspondence with the temporal variations of positive charge separation of graupel in both experiments (Figs. 4.7e–4.7h). Additionally, the negative charge separation of graupel exhibited a similar feature (not shown), although it was weaker than the positive charge separation. These results indicate that charge separation was large when the horizontal wind from the rear side of the convective cell was strong.

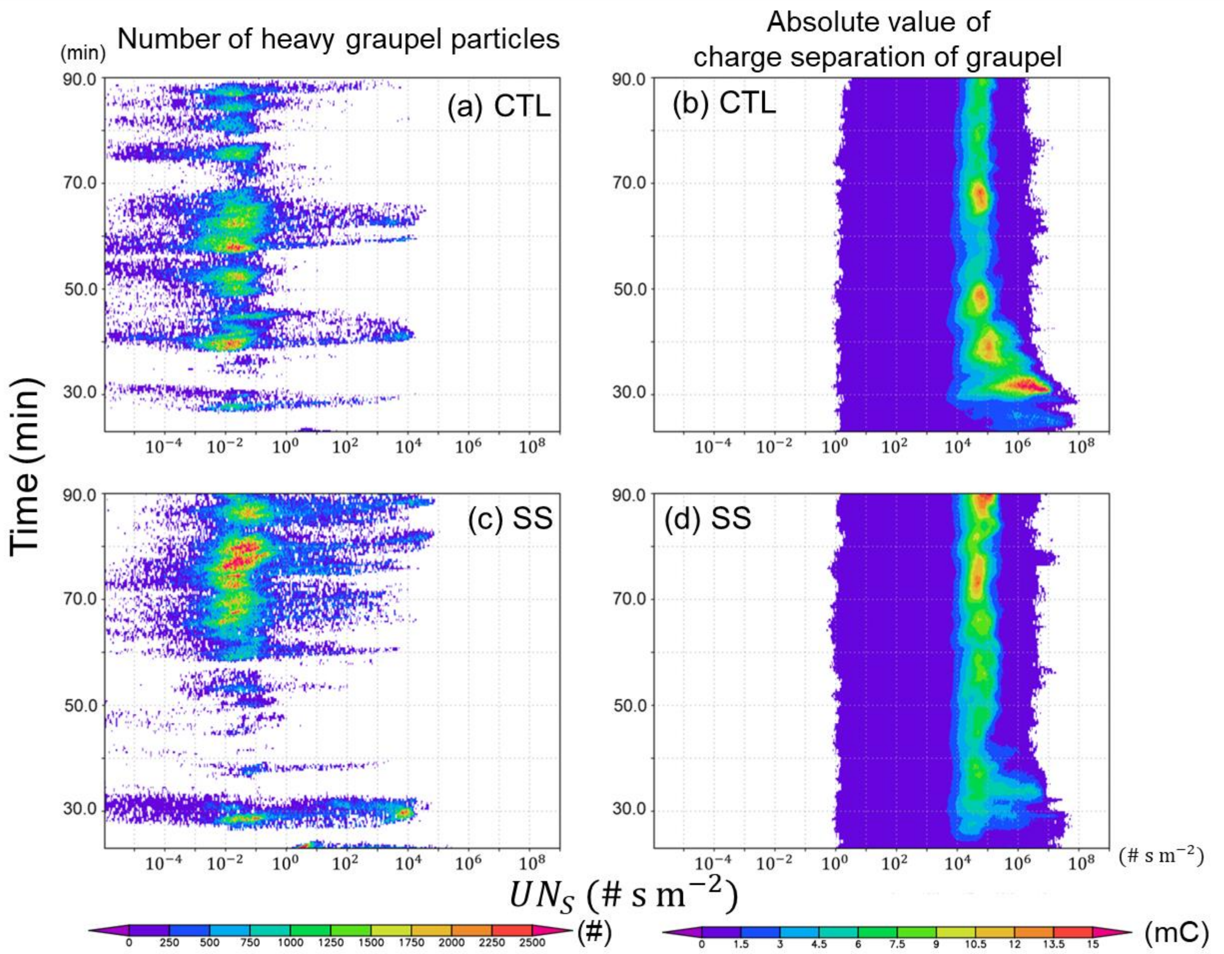

Fig. 4.6. Time series of distribution of summation of each variable with snow number concentration horizontal flux ($\mathrm{m^{-2}\ s^{-1}}$) for grid cells where each variable exists after 24 min from the initial time for (a,b) the CTL experiment and (c,d) the SS experiment. Panels (a) and (c) show the total values of the number of heavy graupel particles exceeding 100 mg. Panels (b) and (d) show the absolute value of charge separation of graupel exceeding 0.5 mC.

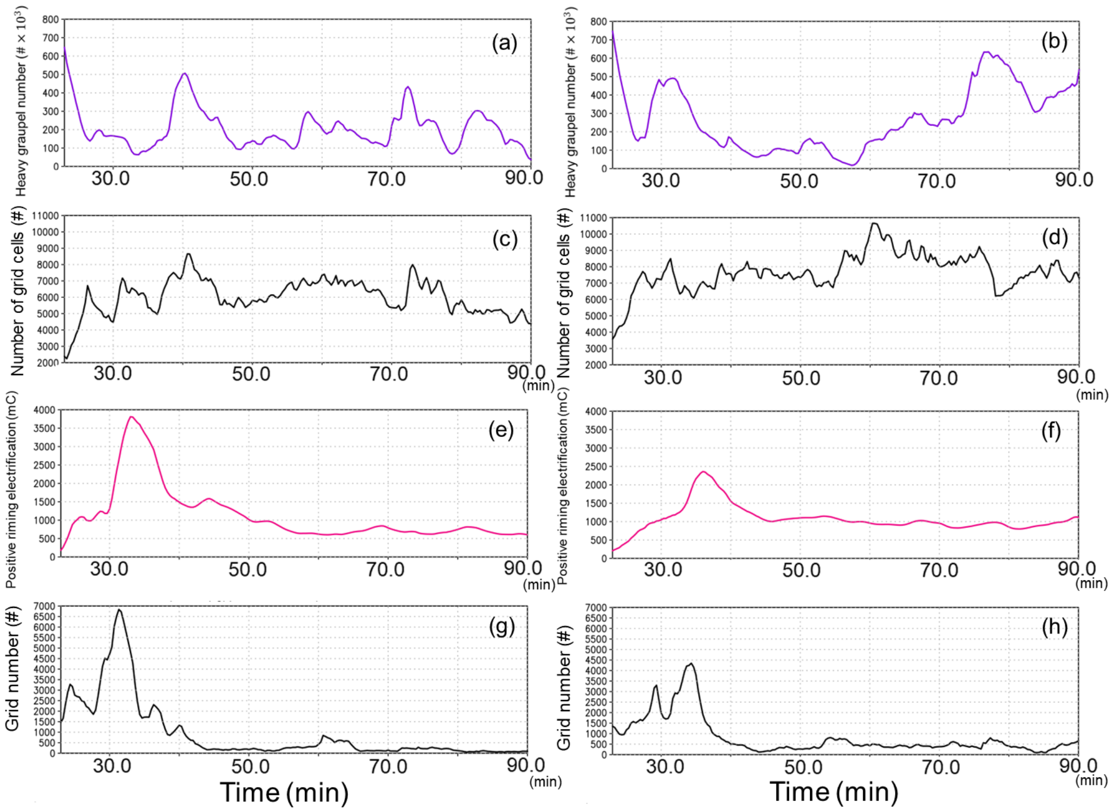

Fig. 4.7. Time series of quantities related to mass flux convection for (left) the CTL and (right) the SS experiments after 24 min from the initial time. Panels (a) and (b) show the number of heavy graupel particles; (c) and (d) indicate the number of grid cells where $UN_S < 10^{-2}$; (e) and (f) represent the positive charge separation; and (g) and (h) correspond to the number of grid cells where $UN_S > 10^{7}$.

Figure 4.8 shows the vertical flux of liquid water WQ_{liq}, which contributed to the production of heavy graupel particles. Heavy graupel particles tended to form during periods when WQ_{liq} ranged of 0–15 $\mathrm{g\,m^{-2}s^{-1}}$ (e.g., Fig. 4.8a: 40 min; Fig. 4.8c: 30 min and 78 min). In contrast, charge separation of graupel occurred in the area of small WQ_{liq} (0–5 $\mathrm{g\,m^{-2}s^{-1}}$) (Fig. 4.8b: 33 min; Fig. 4.8d: 36 min). These results suggest that heavy graupel particles were produced in areas with little supply of solid particles by horizontal winds and a large supply of liquid water from the lower layers.

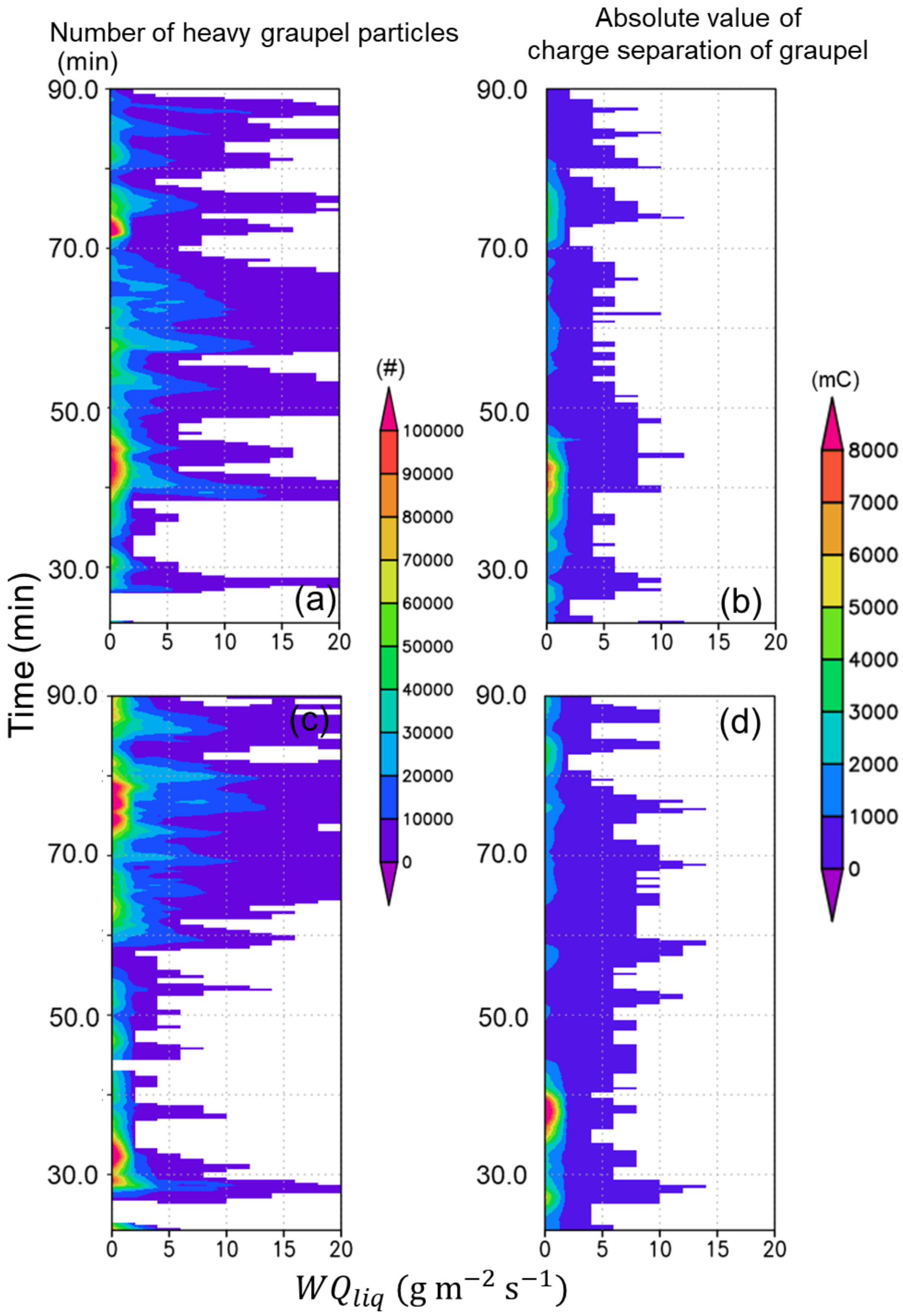

Fig. 4.8. As Fig. 4.6 but for time series of distribution of vertical liquid water flux (g m^{-2} s^{-1}).

4.3.3. Formation of Mixed-phase Area Suitable for Growth of Graupel and Riming Electrification

As described above, the CTL and SS experiments both reproduced the downburst, but only the CTL experiment offered the PLI corresponding to the LJ event. The characteristics of convective cells exhibiting active charge separation and those producing heavy graupel particles differed in each experiment. This difference was originated from the supply to the mixed-phase area of solid particles from the surroundings from lower layers, bywind circulation (Figs. 4.6 and 4.8). In this subsection, we discuss the conditions required for PLI occurrence. According to the analyses in Section 4.3.2, the horizontal wind toward the mixed-phase area corresponding to the horizontal wind from the rear side of the convective cell is a key property for active charge separation and PLI occurrence. Analyses along squall lines suggest that the rear inflow jet from the rear side of the convective cell is dominant when the convection was tilted (Weisman and Rotunno, 2004; Rotunno et al., 1988). Although the present study did not cope with a squall-line system, multi-cell convection is created by the cold pool produced by the convection by the previous generation. Thus, we can discuss PLI as LJ occurrence in multi-cell convection according to the tilting of the convection.

Figure 4.9 shows the horizontal distribution of the vertical winds at altitudes of 5000 m and 7000 m, when active charge separation and active growth of heavy graupel particles, respectively, were seen in both experiments. At the time of active charge separation in the CTL experiment (33.3 min; Figs. 4.9a and 4.9b), the large vertical velocity around the leading edge at z = 5000 m was located around x = 136 km, y = 32 km (shown as the crossing point of the dashed lines in Figs. 4.9a, 4.9b), and that at z = 7000 m was distributed around x = 140 km, y = 34 km (Fig. 4.9b). These results indicate that the convection was tilted when charge separation was active. In contrast, the large vertical velocity was located in the same location (x = 131 km, y = 32 km) at both z = 5000 m and 7000 m when the heavy graupel particles were much generated, shown as the crossing point of the dashed lines in Figs. 4.9c and 4.9d. Upright convection was generated during the active growth of heavy graupel particles. Note that the vertical velocity at x = 137 km, y = 28 km in Figs. 4.9a and 4.9b and x = 134 km, y = 27 km in Figs. 4.9c and 4.9d was negligible, because updrafts in old convective cell are weaker than those in the new cell at the leading edge of the cold pool.

Figure 4.10 shows the convection tilt angle φ_{tilt} as defined in Section 4.2.4. In the CTL experiment (Fig. 4.10a), the area with active riming electrification (140 km < x < 150 km, 6000 m < z < 9000 m) predominantly exhibited tilted convection ($\varphi_{tilt} < \frac{\pi}{6}$). In such a case, the horizontal transport of snow particles and riming electrification were dominant in the convective cell resulting in PLI occurrence. On the other hand, in the mixed-phase area with heavy-graupel production (around x = 130 km, 4500 m < z <6000 m in Fig. 4.10b), most of the convection was upright ($\varphi_{\mathrm{tilt}} > \frac{5}{18}\pi$), and this led to an environment with a large supply of liquid water from the lower layers. Subsequently, heavy graupel particles contributing to downburst were produced in a newly grown upright convection cell (40.0 min).

In the SS experiment, the area of strong updraft was located in the area (x = 136 km, y = 25.5 km) when the heavy graupel particles were much generated (Figs. 4.9e, 4.9f), which is similar to the CTL experiment (Figs. 4.9c, 4.9d). At the time of active charge separation in the SS experiment, the difference in the updraft area between z = 5000 m and z = 7000 m was small (Figs. 4.9g, 4.9h) compared with the tilting in the CTL experiment.

In the SS experiment, before the time of active charge separation, upright convection became dominant (30.0 min); this promoted the production of heavy graupel through riming (Fig. 4.10c), and the downburst followed it (34.3 min; Fig. 4.2d). Subsequently, at 36.6 min, the tilted convection led to the formation of a mixed-phase area suitable for riming electrification. As a result, charge separation attained its peak (Fig. 4.10d), but it did not lead to the downburst.

These results suggest that the sequence from the generation of tilted convection cells conducive to riming electrification to the growth of newly formed upright convection cells is important for active riming electrification preceding the generation of heavy graupel for LJ occurrence.

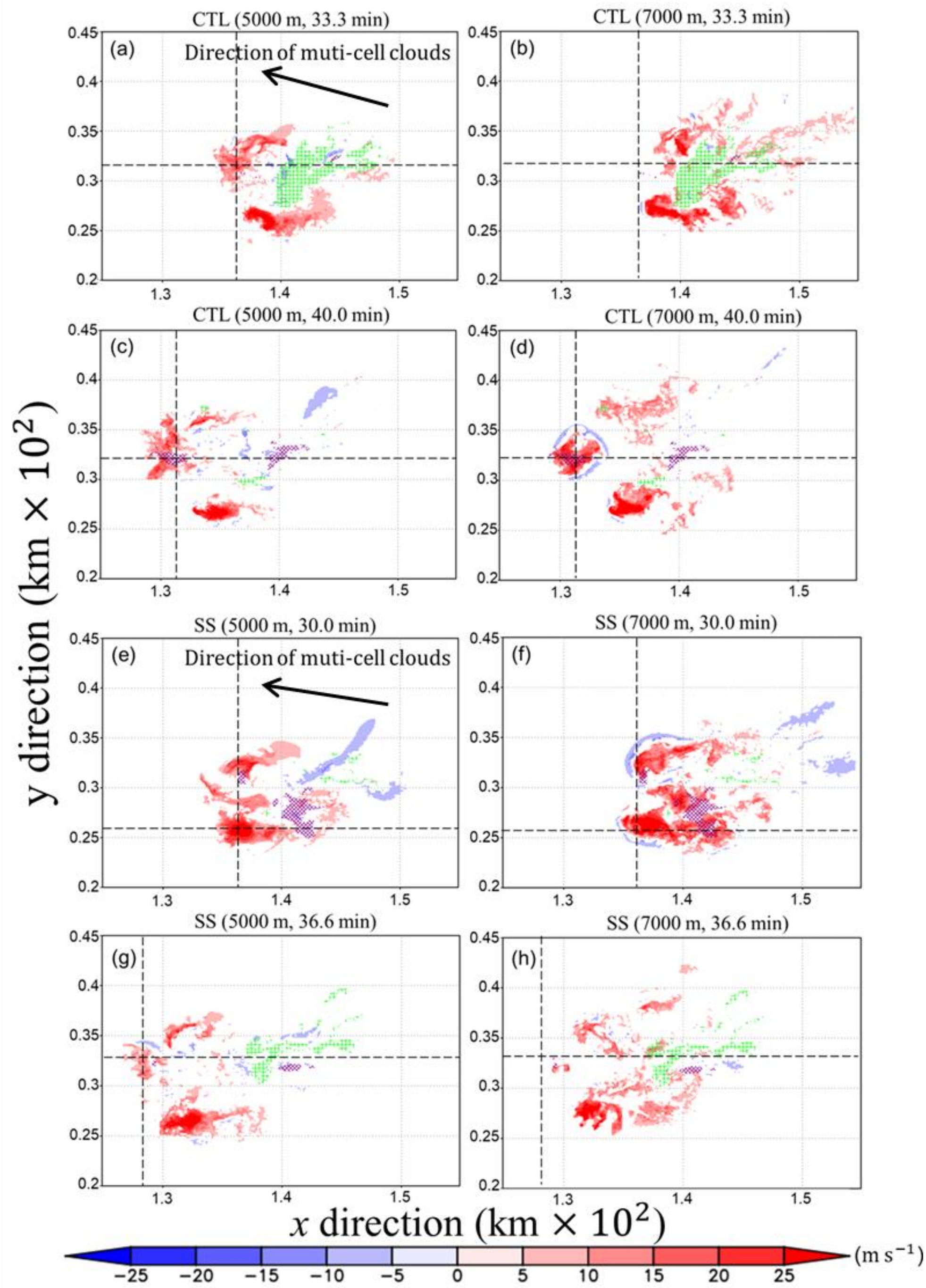

Fig. 4.9. Snapshot at 33.3 min for the CTL experiment at altitudes of (a) 5000 m and (b) 7000 m. The red-blue color shading show vertical wind as per the reference at the bottom. Purple color indicates the area where heavy graupel particles vertically integrated through the domain count > 100. Green color indicates the absolute value of charge separation exceeds 0.5 mC. The crossing point of the two dashed lines is the center of the area of maximum vertical velocity at z = 5000 m at its time of local maximum. (c,d) Same as (a,b) but for 40.0 min. (e-h) Same as (a-d) but for the SS experiment.

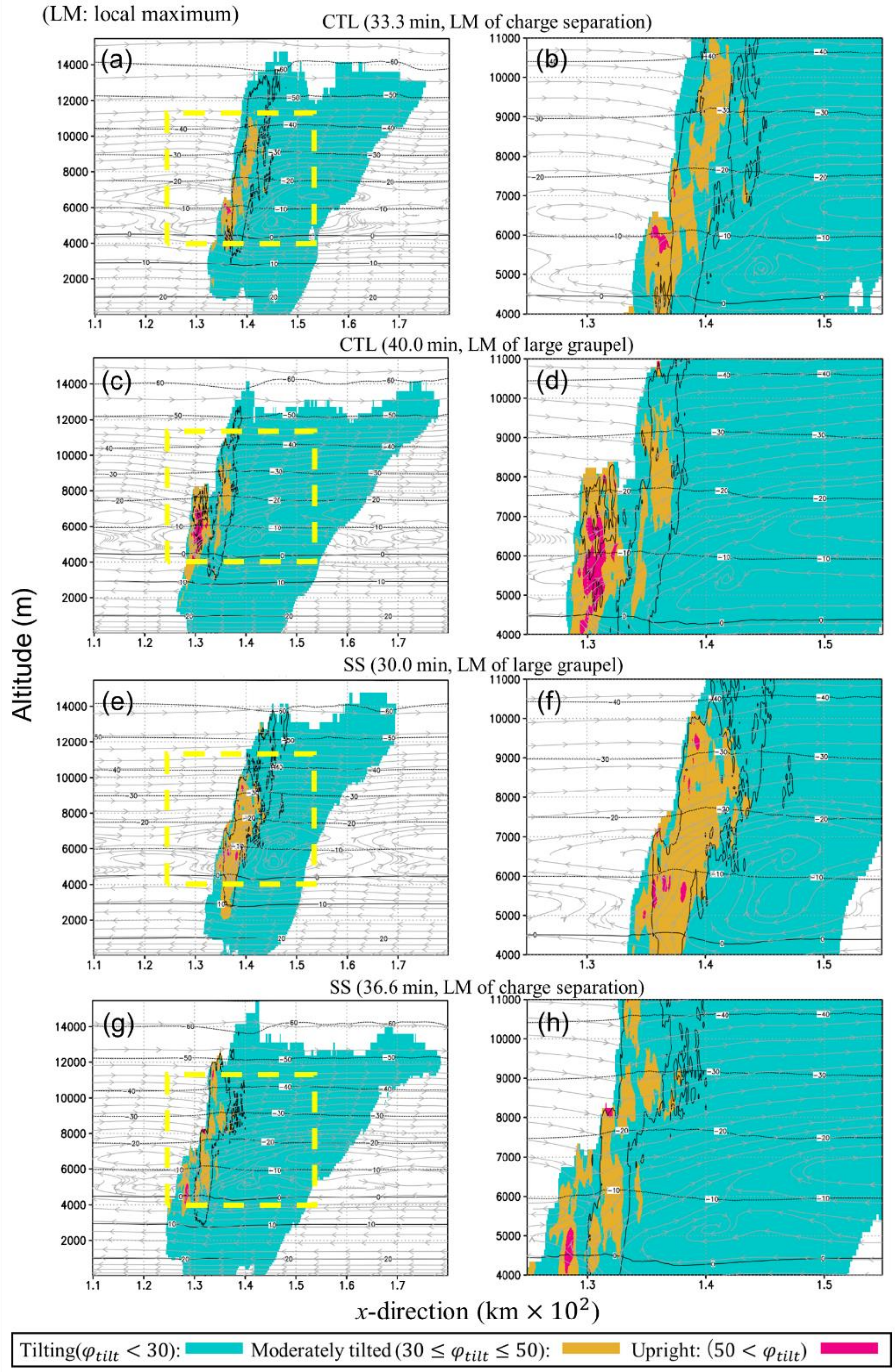

Fig. 4.10. Vertical distribution of wind tilting angle φ_{tilt} averaged in y direction. Blue, yellow, and red represent tilted, moderate, and upright convection, respectively, based on φ_{tilt}. The data are shown over the area where the total condensate averaged in the y direction exceeds 10 g kg^{-1}. The black lines and the gray streamlines indicate the temperature profile and the y-direction-averaged wind streamlines, respectively. (a, c) and (e, g) show the results from the CTL and SS experiments, respectively. (a) and (c) show the results at 33.3 min and 40 min in the CTL experiment, respectively, and (e) and (g) show the results at 40 min and 36.6 min in the SS experiment, respectively. The yellow dashed box in (a, c, e, g) is the area that is enlarged in (b, d, f, h).

The above convection characteristics suggest that the transition to convection cell tilting is related to the LJ mechanism, and so we examined the factors contributing to this transition in the convection environment. Because all convective clouds generated in the idealized experiments that we conducted were multi-cell convective clouds, the tilting of the convection is elucidated by the RKW theory introduced in Section 2.4. As reported in previous studies (Takemi, 2006; Lebo and Morrison, 2014; Rotunno et al., 1988; Weisman and Rotunno, 2004), the environment with $C/\Delta U{\sim}1$ corresponds to optimal convection in the form of upright convection, while that with $C/\Delta U \gg 1$ tends to bring tilted convection. Figure 4.11 shows time series of the frequency of $C/\Delta U > 3$. In the CTL experiment, such an environment was seen around 26 min, which was 7 min before the time of active charge separation (33.3 min). The cold-pool intensity correlated with low-level updrafts represented a high frequency exceeding 15 m s^{-1} (black line in Fig. 4.11b). Therefore, tilted convection could create an environment suitable for riming electrification, leading to PLI occurrence. Environments suitable for tilted convection with $C/\Delta U > 3$ were also observed at 45 min and 65 min (Fig. 4.11a). The cold-pool intensity after 47.6 min was weaker than that at 26 min (Fig. 4.11b), and therefore the convection was weak compared with that at 33.3 min. In such a case, the magnitude of charge separation was small and resulted in a lower lightning frequency.

The diagnosis by $C/\Delta U$ data indicated a small frequency of $C/\Delta U > 3$ at the preceding local maximum of heavy graupel particles (40.0 min). This condition suggests that an environment suitable for upright convection during 30–40 min (Fig. 4.11a) tended to be generated. This environment formed a continuous supply of liquid water from the lower levels with a less of a supply of solid-phase particles from the rear, and it was suitable for producing heavy graupel. Moreover, in the $C/\Delta U{\sim}1$ environment, although the cold-pool intensity became weak after the timing attaining the local maximum of charge separation, multiple downbursts occurred when the convection was upright and suitable for active growth of heavy graupel in the CTL experiment (61 min, 72 min; Fig. 4.2c).

In the SS experiment, even when the cold-pool strength was comparable to the CTL experiment (Fig. 4.11b), $C/\Delta U$ tended to take smaller values because the vertical shear (ΔU) is larger. As a result, around the local maximum at 26 min simulated in the SS experiment, the frequency of $C/\Delta U > 3$ (Fig. 4.11a) was relatively lower, and this feature could form an environment suitable for upright rather than tilted convection. Consequently, this upright convection promoted the active growth of heavy graupel particles starting at 30.0 min.

Based on the relationship between cold-pool intensity and vertical wind shear, we can propose the following conditions for PLI occurrence. When a convective cell is tilted and sufficient cold-pool intensity is generated, an environment suitable for charge separation is formed and leads to increased lightning activity. If the subsequently generated convective cells are upright, then heavy graupel particles are produced therein, leading to downbursts, and this transition leads to PLI occurrence. On the other hand, in cases where only upright convection occurs, while heavy-graupel production is more likely, downbursts can still occur. However, riming electrification occurs less likely, implying that an LJ may not occur. In addition, when the cold pool is weak, the tilted convection does not lead directly to the active charge separation required for the increase of lightning.

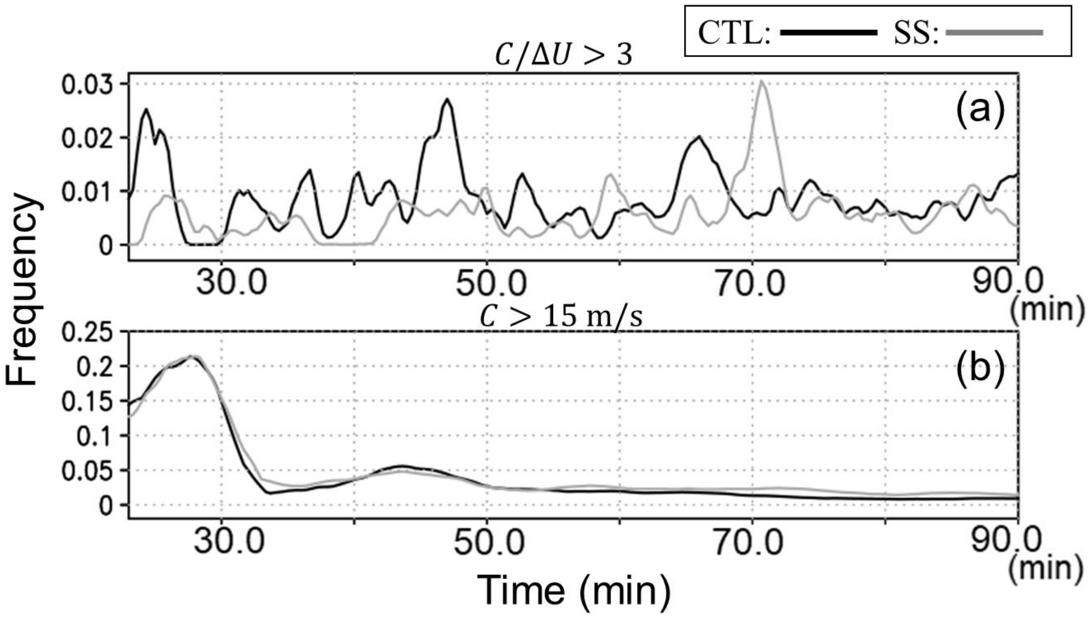

Fig. 4.11. Time series of normalized frequencies of (a) $C/\Delta U > 3$ and (b) $C > 15$ m s^{-1} after 24 min. The black and gray lines are the results of the CTL and SS experiments, respectively.

4.4. Discussion

The model simulated well a PLI corresponding to an LJ characterized by an increase in the lightning flash rate approximately 15 min preceding a downburst. In contrast, a downburst occurred 3 min before the increase in the lightning and no PLI occurred when the vertical wind shear was larger.

When the lightning increased before a downburst, the convection was tilted because of the strong updraft caused by the strong cold pool, and a horizontal wind from the rear side of the convective cell blew. This supplied abundant solid particles such as snow and ice to the mixed-phase area in the convective cell. This supply of solid precipitation particles produced an environment in which graupel, liquid water, and snow and ice coexisted, which was suitable for charge separation by the riming electrification mechanism.

In contrast, when convective clouds with no PLIs were produced, upright convection was generated, and the supply of solid precipitation particles by the horizontal wind from the rear side of the convective cell was prohibited. In such conditions, liquid (supercooled) water was supplied for the mixed-phase area of the convective cell, and an environment with coexisting graupel and liquid water but without snow and ice was produced. In such an environment, riming electrification was prohibited, and the graupel particles grew large via the riming process and resulted in a downburst. This characteristic suggests that an environment with a limited supply of solid particles enhances the growth of heavy graupel.

The conditions required for PLI occurrence were examined by analyzing the transition of cloud microphysical properties, the tilting of convection, and the strength of the cold pool according to the RKW theory. Our analyses clarified that the transition from a tilted convection cell triggered by a strong cold pool to an upright convection cell is required for PLI occurrence. In other cases, the upright convective cell leads to a downburst before the intensification of lightning activity, because riming electrification becomes less active during upright convection. In such cases, a downburst occurs without a PLI. The former is relevant to charge separation, and the latter is associated with the generation of heavy graupel particles. When the cold pool is weak, so is the convection, and therefore the charge separation required for the increase in lightning is not active, but a downburst occurs nevertheless.

The differences in cloud microphysical properties among convective cells caused by the transition of convective conditions were interpreted using a zero-dimensional box model (Appendix 4.6.B). In this model, experiments were conducted under various conditions: the -15SI experiment, representing a mixed-phase region at low temperatures with solid particles (snow and cloud ice) supply characteristic of tilted convection conducive to charge separation; the -5noSI experiment, simulating high temperatures without solid particles supply, suitable for the production of heavy graupel associated with upright convection; and two sensitivity experiments, -5SI and -15noSI. The results showed that charge separation in the -15SI experiment was most active in these experiments, while heavy graupel in the -5noSI experiment was most efficiently produced. Furthermore, in the sensitivity experiments with different temperature and solid particle supply settings, both charge separation and heavy graupel production were relatively less efficient. These results indicate that variations in convective conditions led to differences in the mixed-phase area conditions within convective cells. These differences, in turn, resulted in distinctions in charge separation and heavy graupel production.

The difference between convective cells with active riming and those with active riming electrification is consistent with observations and laboratory experiments on the growth environment of wet-growth hail and the characteristics of charge separation. Emersic et al. (2010) reported that during the early stages of thunderstorm development, lightning tends to avoid wet-growth regions of hail. Jayaratne and Saunders (2016) conducted laboratory experiments using ice crystals and an icing cylindrical rod simulating riming hail to observe charge separation by riming electrification, and they found that when the ice crystals and simulated hail collided, little charge separation occurred in the wet-growth regions of the simulated hail.

The hypothesis regarding the conditions for the increase in lightning activity preceding downbursts in multi-cell convective clouds can be supported by previous studies. Several studies reported that not only extremely strong updrafts but also moderate ones can enhance the growth of graupel such as hail (Jewell and Brimelow, 2009; Lin and Kumjian, 2022; Nixon et al., 2023). Furthermore, the characteristics of the environment with active riming electrification are consistent with the findings in Ushio et al. (2003) and Salinas et al. (2022). They reported that environments with vortices and turbulence generated by rear inflow jets derived from tilted convection, are conducive to lightning occurrence referred to as a “lightning bubble.” The insights gained from this study align with findings from previous numerical and observational research on tilt of convective clouds conducive to lightning activity (Gharaylou et al., 2020) and on the characteristics of low-level wind shear features that inhibit production of heavy graupel particles (Nelson, 1987; Kumjian and Ryzhkov, 2008; Dennis and Kumjian, 2017).

4.5. Conclusion

This study was aimed to propose the possible mechanisms and required conditions for LJs in multi-cell convection focused on riming growth and riming electrification, which are good indicators of downburst and lightning, respectively. To achieve this, we conducted idealized experiments focused on multi-cell convective clouds using a meteorological model coupled with a BLM that explicitly calculates lightning and graupel growth processes. The experiments were conducted using sounding data from a case of multiple downburst events with lightning.

In this study, through the analysis focused on graupel in a mixed-phase area, the convective cell can be categorized into the following four patterns as illustrated schematically in Fig. 4.12 according to the relationship between the strength of the cold pool (C) and the vertical shear of the horizontal wind (ΔU).

1. When $C/\Delta U \gg 1$ and the cold pool is strong, the convection tends to tilt and updrafts are strong. This environment forms a tilted convective cell with an abundant supply of solid particles by the horizontal wind from the rear side of the convective cell corresponding to a rear inflow jet, contributing to riming electrification (Fig. 4.12a).

2. When $C/\Delta U \gg 1$ and the cold pool is weak, the convection tends to tilt and updrafts are relatively weak. This environment forms a convective cell with a limited supply of solid particles contributing to riming electrification. In this environment, the lightning is less active as well as the growth of heavy graupel particles (Fig. 4.12b).

3. When $C/\Delta U \sim 1$ and the cold pool is strong, the convection tends to be upright and updrafts are strong. This environment forms a convective cell supplying abundant liquid water from the lower layers and few solid particles contributing to the production of heavy graupel particles (Fig. 4.12c).

4. When $C/\Delta U \sim 1$ and the cold pool is weak, the convection tends to be upright and updrafts are relatively weak. This environment forms a convective cell supplying liquid water from the lower layer and few solid particles. Then if liquid water is supplied sufficiently to grow graupel particles by riming, heavy graupel particles can be produced and result in a downburst (Fig. 4.12d).

From our analyses, we suggest that an LJ occurs when a convective cell transitions in the sequence of Fig. 4.12a to Figs. 4.12c or 4.12d from one convection to the next in multi-cell convection. In this context, LJ events do not always occur in all multi-cell convective clouds; rather, an LJ develops provided that certain critical conditions are satisfied. Additionally, LJ events originating from the transition of convective cells are not expected in isolated convective clouds; this is consistent with the observation that multi-cell convective clouds are associated more with LJ events than are isolated convective clouds (Rigo and Farnell, 2022).

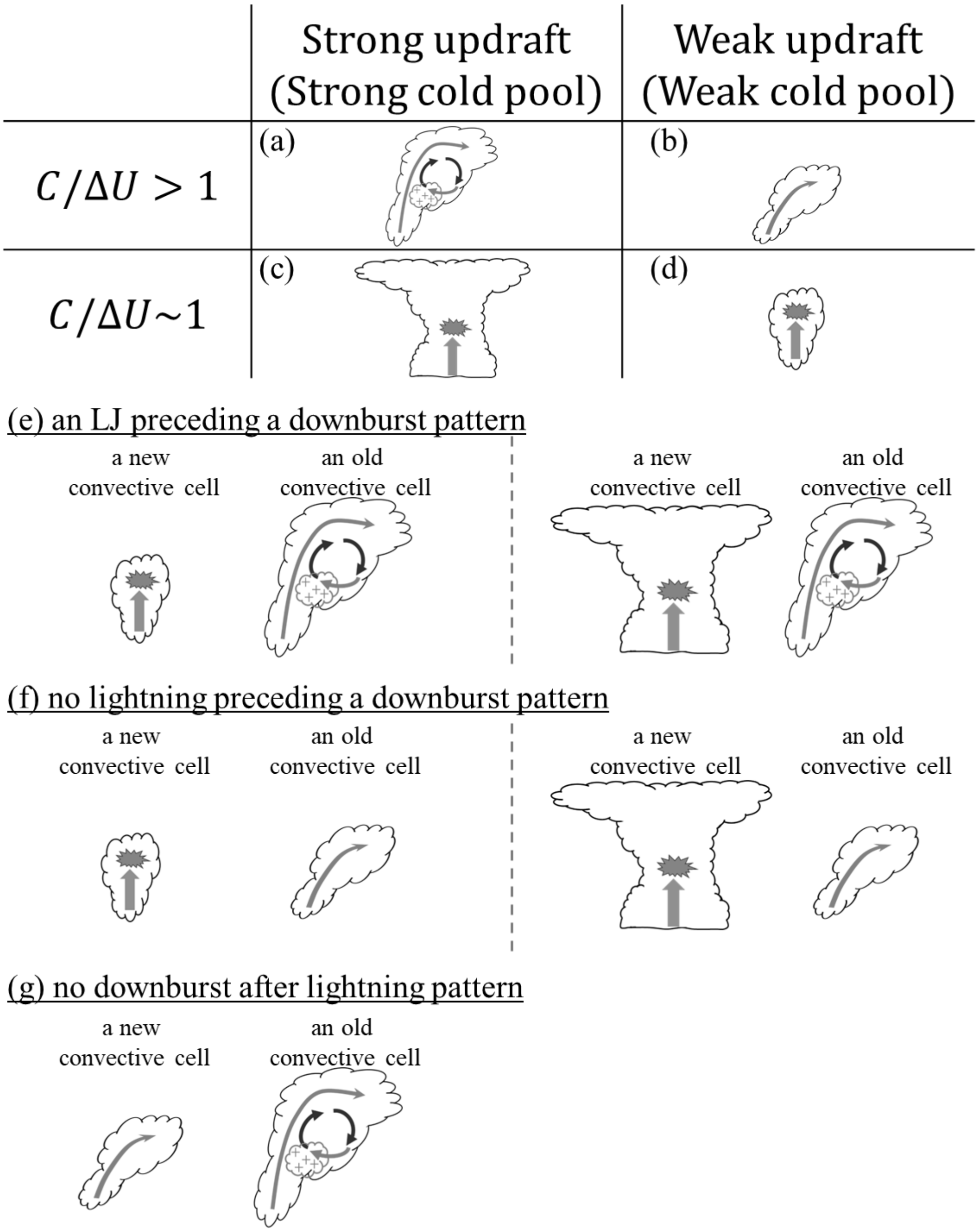

Fig. 4.12. Schematics of convective cells determined by $C/\Delta U$ and updrafts: (a) tilted convection with strong updrafts; (b) tilted convection with relatively weak updrafts; (c) upright convection with strong updrafts; and (d) upright convection with relatively weak updrafts. (e–g) diagram whether an LJ occurs preceding a downburst, driven by the regeneration of individual convective cells determined by $C/\Delta U$ and updrafts. (e) Represents a pattern where an LJ occurs preceding a downburst; (f) a downburst occurs without preceding lightning activity; and (g) lightning occurs without resulting in a downburst.

While the transitions in the mixed-phase area present in this study require verification through observations of both graupel and snow in mixed-phase clouds, indirect validation could be possible by observing the reflectivity core and wind circulations within convective clouds. This requires the need for further studies and combined observations of hydrometeor identification and wind velocity fields to fully understand the complexities of mixed-phase transitions in convective clouds. In addition, treating them as a more-sophisticated index of weather warnings (e.g., Schultz et al., 2009) requires an understanding of the lead time preceding LJ occurrence, which still poses a challenge.

4.6. Appendix

4.6.A. Snapshots of precipitation and model bottom wind speed

To confirm the general characteristics of the simulated convective clouds, the distribution of precipitation and winds were represented (Fig. 4.A1).

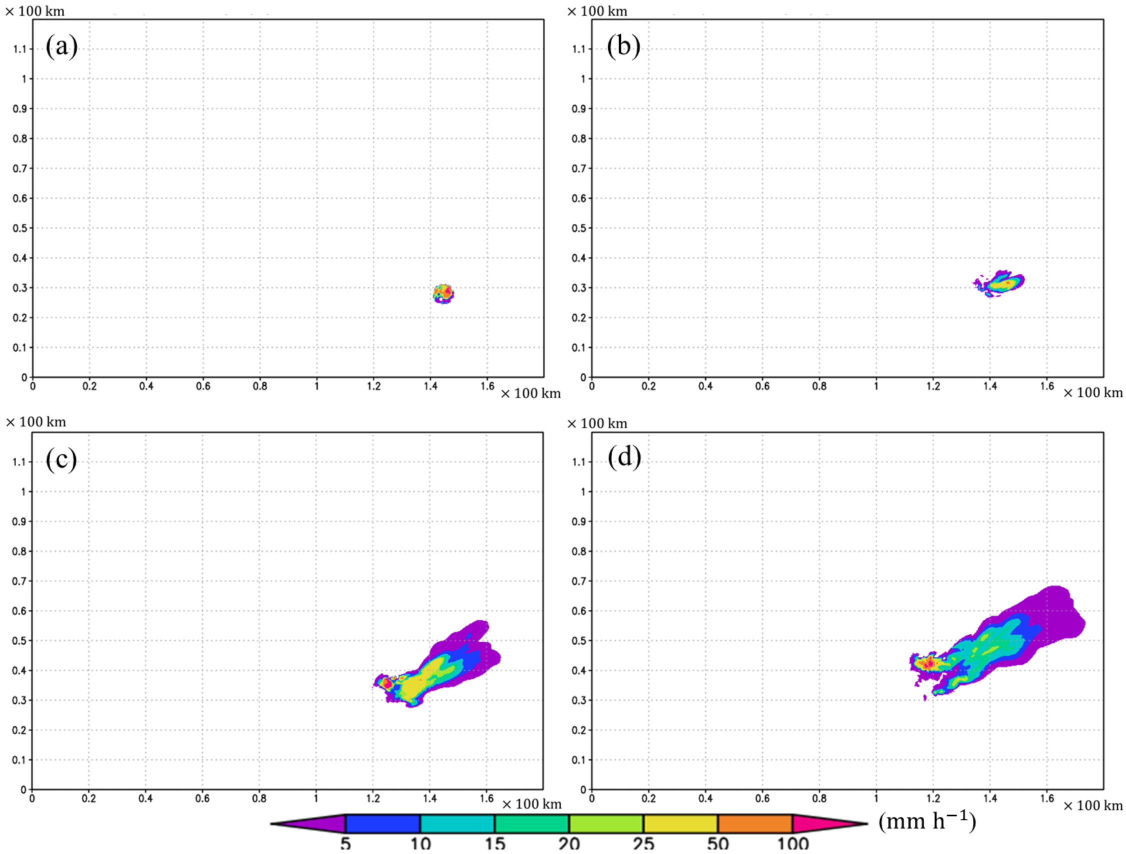

Fig. 4.A1. Snapshots of precipitation (shaded area) and wind speed in the model bottom layer (counter). The snapshot time are (a) 27 min, (b) 34 min, (c) 47 min, and (d) 60 min from the initial time.

4.6.B. Zero-dimensional Collection Process and Box Model

To understand the characteristics of the environments suitable for the growth of graupel by riming and charge separation by riming electrification within mixed-phase areas, we conducted zero-dimensional collection experiments using a zero-dimensional box model. The model was constructed by using only the scheme for calculating the collection processes, including riming and aggregation of the cloud microphysics scheme used in this study (Seiki and Nakajima, 2014). Using this model, the variation of each hydrometeor's category can be calculated by only the collection process.

The initial values for the experiments were created from the output of the zero-dimensional box model in a grid box within the mixed-phase area, and the output values were adjusted to simple ones to make the sensitivity experiments easier. As given in Table 4A1, the output values of density and the mass mixing ratio and number concentration of graupel, snow, and cloud ice were those at x = 141 km, y = 31 km, and z = 7000 m at the time of active charge separation in the CTL experiment (at 33.3 min) to test the rebound between graupel and snow as a means of riming electrification. The output values of the other variables were those at x = 141 km, y = 38 km, and z =5000 m at the time of active production of heavy graupel in the CTL experiment (at 40.0 min) to test the riming growth. Note that the influence of the selection of density and pressure on these sensitivity experiments was negligible (figure not shown). The sensitivity experiments were conducted by sweeping the temperature and the number concentration of snow/ice, and for this we selected the temperature range of active charge separation (−15 °C) in Fig. 4.3a and active graupel production (−5 °C) in Fig. 4.3b in Section 4.3.2. Additionally, experiments were conducted to investigate the influence of solid-particle supply on charge separation and graupel growth. For the experiments, the values for ice and snow were set to zero or present, and the values for rain and cloud water were set to fixed values. The experiments were named as given in Table 4.B2.

Fig. 4.B1 shows the time series of each variable. For the graupel mixing ratio

(Fig. 4.B1a), its rate of increase was temperature dependent, but the graupel mixing ratio increasing with time was a common feature of all four experiments. Meanwhile, the mean graupel weight increased when the number concentration decreased and vice versa (Figs. 4.B1b and 4.B1c). When ice and snow were present (i.e., experiments -5SI and -15SI), particles rebounded actively during graupel–snow collisions when the temperature was low (Fig. 4.B1d). In addition, the number of graupel particles decreased more effectively in the experiments with higher temperature (Fig. 4.B1e), suggesting that the smaller number of graupel particles resulted in fewer particles rebounded by collisions in warmer temperatures. Thus, collisions and rebounds between graupel and snow, which are critical for riming electrification, become more active at low temperatures because of the low sticking efficiency.

In contrast, when the temperature was high, the number of rebounding particles was small (Fig. 4.B1d). In such conditions, the graupel particles tend to stick more effectively, and so they become heavy (Fig. 4.B1c) and their number concentration becomes small (Figs. 4.B1b and 4.B1e).

Without snow and ice (i.e., experiments -5noSI and -15noSI), the graupel number and weight were small and large, respectively (Figs. 4.B1b and 4.B1c), and the graupel easily became heavy (Fig. 4.B1c).

The results outlined above suggest that heavy graupel particles tend to be produced when the temperature is higher and the supply of snow particles is limited, while lower temperature and active supply of ice and snow particles result in increased charge separation.

Table 4.B1. Initial values for sensitivity experiments using zero-dimensional collection process.

Variable	Value	Unit
Temperature	−15 / −5	°C
Density (ρ)	0.708	kg m^{-3}
Pressure	548	hPa
ρQ_g	6.372×10^{-3}	kg m^{-3}
ρQ_s	1.070×10^{-5} / 0.0	kg m^{-3}
ρQ_i	4.404×10^{-5} / 0.0	kg m^{-3}
ρQ_r	2.266×10^{-3}	kg m^{-3}
ρQ_c	3.394×10^{-3}	kg m^{-3}
N_g	5133.0	m^{-3}
N_s	4248.0 / 0.0	m^{-3}
N_i	62304 / 0.0	m^{-3}
N_r	19824.0	m^{-3}
N_c	198240.0	m^{-3}

Table 4.B2. Names of all zero-dimensional experiments.

	Snow and cloud ice	No snow and cloud ice
High temperature (−5 °C)	-5SI	-5noSI
Low temperature (−15 °C)	-15SI	-15noSI

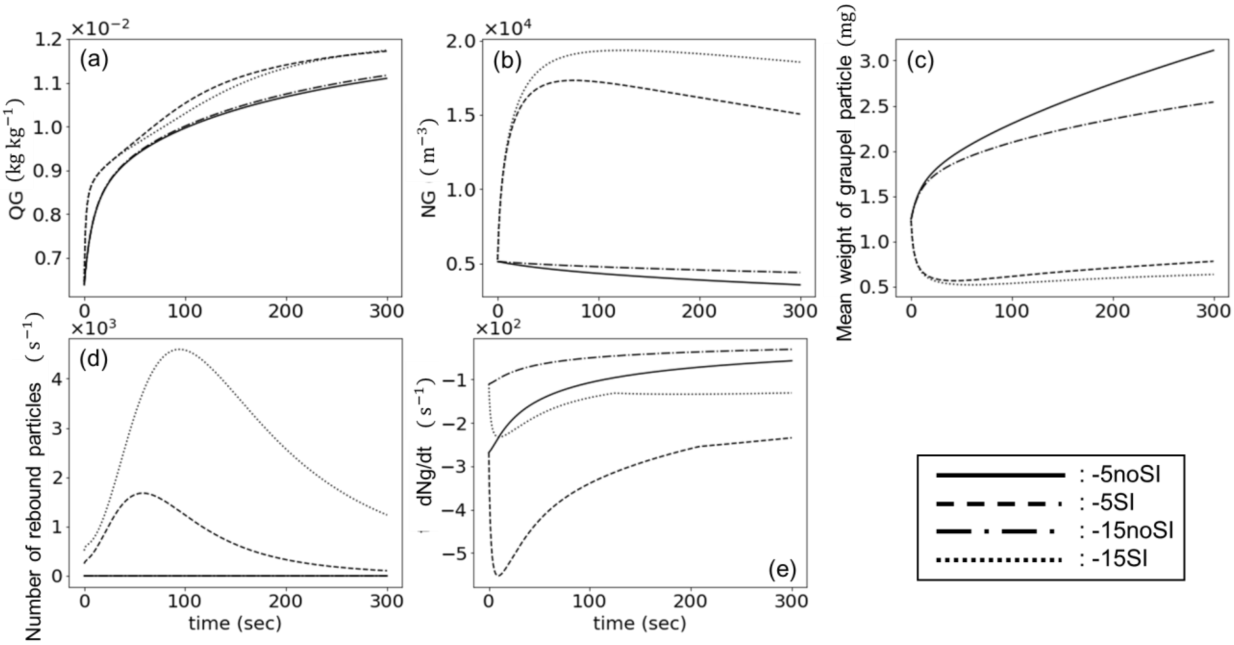

Fig. 4.B1. Time series of each variable in experiments involving zero-dimensional collection process: (a) graupel mass mixing ratio; (b) number of graupel particles; (c) mean weight of graupel particles; (d) number of rebounding particles after collision between graupel and snow in unit time; (e) variation of graupel collision number. Solid, dashed, dash-dotted, and dotted lines represent the experiments with no snow/ice particles at −5 °C (experiment -5noSI), snow/ice particles at −5 °C (experiment -5SI), no snow/ice particles at −5 °C (experiment -15noSI), and snow/ice particles at −15 °C (experiment -15SI), respectively.

Chapter 5. General Summary

In this doctoral dissertation, idealized numerical experiments were conducted using a meteorological model coupled with a bulk lightning model (BLM) that explicitly calculates lightning processes to investigate the mechanism of the rapid increase of lightning activity preceding downbursts in mixed-phase clouds. The results of the simulation indicate that the transition of the dominant cloud microphysical process in each convection cell, depending on the characteristics of the tilt of the convection, is important for the mechanism (Chapter 4). To evaluate the cloud microphysics schemes, which have an important role in occurrences of lightning and downbursts, the model was evaluated through comparisons with observational data, including in situ measurement by disdrometers and satellite observation (Chapter 2). To extend the evaluation using disdrometer observation data for one winter season i.e., 3 months, an automated classification method for types of precipitation particles based on *v-D* distribution was developed utilizing machine learnings (Chapter 3).

In Chapter 2, three microphysics schemes were evaluated through comparison with observational data, including in situ observations from a disdrometer: VSVD, focusing on snowfall in Hokkaido. The results showed that the 2-moment bulk scheme, which is usually used for BLM, accurately reproduced the observed values.

In Chapter 3, we developed an objective evaluation method using a machine learning approach to classify precipitation particle types based on particle size-fall velocity data observed by the disdrometers used in Chapter 2. This method was applied to *v-D* data observed during the winter season in Hokkaido. Following KI20, we first used the EM algorithm to estimate a single or a mixed probability density function (PDF) from the size-fall velocity data with the *v-D* relationship. The estimated *v-D* relationship was used as input vectors to create a SOM map. The SOM map enabled the classification of graupel and snow from the observational data. The evaluation of the cloud microphysics scheme in Chapters 2 and 3 showed that the 2-moment bulk scheme well-reproduced mixed-phase clouds.

Chapter 4 aimed to investigate the mechanisms and necessary conditions for the increase in lightning activity preceding downbursts in multicell convective clouds by focusing on riming growth and riming electrification, which are required for downbursts and lightning, respectively. To achieve this, idealized experiments using a meteorological model coupled with BLM were conducted. The results successfully simulated the precursor lightning increase (PLI), which corresponds to a lightning jump before the downburst. When lightning activity increased preceding a downburst, strong updrafts generated by a strong cold pool resulted in the tilted convection, leading to the development of horizontal winds from the rear of the convective cell. The horizontal wind from the rear side supplies solid particles, such as snow and ice, in the mixed-phase area of the convective cell. This influx of solid particles formed an environment in which graupel, liquid water, and snow coexist, thereby establishing conditions conducive to charge separation through the riming electrification, and active lightning. If the upright convection, suitable for the downburst, is generated after the tilted convection with active lightning, the downburst occurs after the rapid increase of the lightning. This transition is observed as lightning increase preceding downburst. We therefore revealed that the transition of convection cells from tilted to upright convection under specific vertical wind shear and cold pool intensity conditions is important for the rapid increase in lightning activity preceding downbursts.

The transition of convective tilts influence changes in the dominant cloud microphysical processes within the mixed-phase regions of convective cells. The changes provides valuable insights into the mechanisms driving the increase in lightning activity preceding severe weather events such as strong winds, hail, and heavy rainfall. In future works, the relationship between the convective environment and the microphysical properties in the mixed-phase area of multicell convective clouds, as derived from this numerical study, could be validated through observational studies. For example, particle classification using radar observations (e.g., Hydrometeor Classification Algorithm; Liu and Chandrasekar, 2000; Park et al., 2009; Kouketsu et al., 2015) and three-dimensional wind field measurements (e.g., Gao et al., 2004; Cha and Bell, 2023) have the potential usage for validation.

Moreover, the evaluation of simulations and their comparison with observations, as conducted in Chapters 2 and 3, is crucial for the utilization of meteorological models. The evaluation of cloud microphysics schemes using in-situ observational data, including disdrometer data, conducted in Chapter 2 is particularly important. Cloud microphysics schemes are also used in the global cloud-system resolving model or convective permitting model such as Nonhydrostatic ICosahedral Atmospheric Model (NICAM: Tomita and Satoh, 2004; Satoh et al., 2014), ICOsahedral Nonhydrostatic (ICON: Giorgetta et al., 2018; Zängl et al., 2015), and Model for Prediction Across Scales (MPAS: Skamarock et al., 2012). Therefore, the evaluation of cloud microphysics schemes across different climatic zones and cloud systems is important in global cloud-resolving simulations (Roh and Satoh, 2014; Roh et al., 2020; Seiki and Roh, 2020). For further improvement in the accuracy of the models, it is necessary to conduct further evaluation focusing on the variations in cloud microphysical properties at higher spatiotemporal resolution and across diverse precipitation systems.

The novel precipitation particle classification method developed in Chapter 3, which combines the EM algorithm and SOM, is useful for evaluating the cloud microphysical properties in diverse precipitation systems. This new method enables the automatic classification of precipitation particles from disdrometer data, even without prior datasets of the *v-D* relationship. In future studies, with sufficient and long-term *v-D* data (e.g., Multidisciplinary drifting Observatory for the Study of Arctic Climate expedition; Matrosov et al., 2022), it will be possible to create a comprehensive SOM reference map. Therefore, by applying this method to disdrometer data from around the world, including traditional disdrometers such as 2DVD (Kruger and Krajewski, 2002), LPM (Angulo-Martínez et al., 2018), and PARSIVEL (Löffler-Mang and Joss, 2000; Battaglia et al., 2010), it will become possible to automatically evaluate the characteristics of precipitation particles across different regions and seasons. This will enhance the understanding of precipitation patterns and could contribute to the improvement of meteorological models. Such applications are feasible because the same results can be obtained regardless of the disdrometer used if particle size and fall velocity are accurately measured.

This doctoral dissertation indicates that numerical studies using meteorological models can promote the analysis of cloud microphysical characteristics in mixed-phase clouds, and more robust analyses can be achieved by integrating observational studies. Future studies are expected to provide a deeper understanding of the microphysical properties of mixed-phase clouds through high spatiotemporal resolution numerical simulations that represent both homogeneous and heterogeneous mixing of liquid and solid particles (Korolev and Milbrandt, 2022). Additionally, from the perspective of various types of solid particles, more advanced cloud microphysics schemes have been developed (e.g., the Predicted Particle Properties (P3) bulk microphysics scheme; Morrison and Milbrandt, 2015), which express solid particles as a single category by explicitly calculating prognostic variables related to solid particle shapes, such as riming fraction and aspect ratio. Thus, to more deeply understand the microphysical and electrical properties involved in the mixing of liquid and solid particles in various mixed-phase clouds, further development of meteorological models and bulk lightning models is necessary.

Acknowledgments

I would like to express my gratitude thanks to Dr. Yousuke Sato, who is the chief referee of my doctoral dissertation, for supporting this study and suggesting valuable comments and discussions. I also deeply thank all associate referees, Prof. Masaru Inatsu, Prof. Shosihro Minobe, Dr. Yoshinori Sasaki, and Dr. Akihiro Hashimoto. I would like to thank Dr. Yuta Katsuyama, Dr. Sho Kawazoe, and Dr. Akihiro Hashimoto for giving me many suggestions for my work about snowfall. I thank Dr. Takumi Honda, Prof. Tetsuya Takemi, Dr. Atsushi Hamada, Dr. Satoru Yoshida, Dr. Syugo Hayashi, and Mr. Akihito Umehara for giving me many suggestions for my work about downburst and lightning. I thank Ms. Atsuko Kobayashi and Ms. Choko Maeda for supporting office procedures and thank the other laboratory members for giving me a great time. I would also like to express my deep gratitude to the Tsutsu-Uraura young meteorologists, with whom I have deepened my connections both academically and personally. Additionally, I am sincerely grateful to the Kishou Natsu no Gakkou, which paved the way for my journey in meteorology. I hope that these connections and the opportunities that foster them will continue into the future. Finally, I really thank my parents for encouraging me to continue a doctoral course.

This research is supported by Grant Number JP20H04196, JP21H04571, JP20H05729, and JP23KJ0037, JST SPRING Grant Number JPMJSP2119, the Moonshot R&D program of the JST (Grant Number JPMJMS2286). This research is also supported by the Research Field of Hokkaido Weather Forecast and Technology Development (endowed by Hokkaido Weather Technology Center Co. Ltd.), Support Program for Next Generation Supercomputer, Information Initiative Center of Hokkaido University, the

Cooperative Research Activities of Collaborative Use of Computing Facility (JURCAOSCFS23-02) of the Atmosphere and Ocean Research Institute, the University of Tokyo, the SECOM Science and Technology Foundation. We thank Prof. Keiji Wada and Dr. Tomohiko Sekiguchi of Hokkaido University of Education, Prof. Yasushi Fujiyoshi, Dr. Masayuki Kawashima of Hokkaido University, and Dr. Seika Tanji of Kyoto University for their support for the disdrometer observation. We also thank Dr. Tempei Hashino of Kochi University of Technology for his comments about Joint-simulator, Dr. Sho Kawazoe for his useful comments about the SOM map, and Prof. Hiroshi Niino of the University of Tokyo for supplying the sounding data and for his useful comments.

References

Abd-Elaal, E. S., Mills, J. E., Ma, X., 2018: A review of transmission line systems under downburst wind loads. *Journal of Wind Engineering and Industrial Aerodynamics*, 179, 503–513. https://doi.org/10.1016/J.JWEIA.2018.07.004

Akinduko, A. A., E. M. Mirkes, A. N. Gorban, 2016: SOM: Stochastic initialization versus principal components. *Information Sciences (Ny).*, 364–365, 213–221, https://doi.org/10.1016/J.INS.2015.10.013.

Angulo-Martínez, M., S. Beguería, B. Latorre, M. Fernández-Raga, 2018: Comparison of precipitation measurements by OTT Parsivel2 and Thies LPM optical disdrometers. *Hydrology and Earth System Sciences,* 22, 2811–2837, https://doi.org/10.5194/hess-22-2811-2018.

Bader, M. J., S. A. Clough, G. P. Cox, 1987: Aircraft and dual polarization radar observations of hydrometeors in light stratiform precipitation. *Quarterly Journal of the Royal Meteorological Society*, 113, 491–515, https://doi.org/10.1002/QJ.49711347605.

Bailey, M., J. Hallett, 2004: Growth rates and habits of ice crystals between 20 and 70C. *Journal of the Atmospheric Sciences*, 514–544 pp. https://doi.org/10.1175/1520-0469(2004)061<0514:GRAHOI>2.0.CO;2

Barthe, C., Chong, M., Pinty, J. P., Bovalo, C., Escobar, J., 2012: CELLS v1.0: Updated and parallelized version of an electrical scheme to simulate multiple electrified clouds and flashes over large domains. *Geoscientific Model Development*, 5(1), 167–184. https://doi.org/10.5194/GMD-5-167-2012

Battaglia, A., E. Rustemeier, A. Tokay, U. Blahak, C. Simmer, 2010: PARSIVEL snow observations: A critical assessment. *Journal of Atmospheric and Oceanic Technology*, 27, 333–344, https://doi.org/10.1175/2009JTECHA1332.1.

Beljaars, A. C. M., A. A. M. Holtslag, 1991: Flux parameterization over land surfaces for atmospheric models. *Journal of Applied Meteorology*, 30, 327–341, https://doi.org/10.1175/1520-0450(1991)030<0327:FPOLSF>2.0.CO;2.

Bennetts, D.A., Rawlins, F., 1981: Parametrization of the ice-phase in a model of mid-latitude cumulonimbus convection and its influence on the simulation of cloud development. *Quarterly Journal of the Royal Meteorological Society*, 107, 477–502. https://doi.org/10.1002/QJ.49710745302

Bernauer, F., Hürkamp, K., Rühm, W., & Tschiersch, J., 2016: Snow event classification with a 2D video disdrometer—A decision tree approach. *Atmospheric Research*, 172, 186-195. https://doi.org/10.1016/j.atmosres.2016.01.001

Bessho, K., Coauthors, 2016: An introduction to Himawari-8/9 - Japan's new-generation geostationary meteorological satellites. *Journal of the Meteorological Society of Japan*, 94, 151–183, https://doi.org/10.2151/jmsj.2016-009.

Boussaton, M. P., S. Coquillat, S. Chauzy, F. Gangneron, 2004: A new videosonde with a particle charge measurement device for in situ observation of precipitation particles. *Journal of Atmospheric and Oceanic Technology*, 21, 1519–1531, https://doi.org/10.1175/1520-0426(2004)021<1519:ANVWAP>2.0.CO;2.

Brdar, S., Seifert, A., 2018: McSnow: A Monte-Carlo Particle Model for Riming and Aggregation of Ice Particles in a Multidimensional Microphysical Phase Space. *Journal of Advances in Modeling Earth Systems,* 10, 187–206.

https://doi.org/10.1002/2017MS001167

Brook, M., Nakano, M., Krehbiel, P., Takeuti, T., 1982: The electrical structure of the hokuriku winter thunderstorms. *Journal of Geophysical Research: Oceans,* 87, 1207–1215. https://doi.org/10.1029/JC087IC02P01207

Cha, T. Y., Bell, M. M., 2023: Three-Dimensional Variational Multi-Doppler Wind Retrieval over Complex Terrain. *Journal of Atmospheric and Oceanic Technology*, 40(11), 1381–1405. https://doi.org/10.1175/JTECH-D-23-0019.1

Chang, K., Bench, J., Brege, M., Cantrell, W., Chandrakar, K., Ciochetto, D., Mazzoleni, C., Mazzoleni, L. R., Niedermeier, D., & Shaw, R. A. 2016: A Laboratory Facility to Study Gas–Aerosol–Cloud Interactions in a Turbulent Environment: The Π Chamber. *Bulletin of the American Meteorological Society*, 97(12), 2343–2358. https://doi.org/10.1175/BAMS-D-15-00203.1

Chen, Z., Qie, X., Yair, Y., Liu, D., Xiao, X., Wang, D., Yuan, S., 2020: Electrical evolution of a rapidly developing MCS during its vigorous vertical growth phase. *Atmospheric Research*, 246, 105201. https://doi.org/10.1016/J.ATMOSRES.2020.105201

Chern, J. D., W. K. Tao, S. E. Lang, T. Matsui, J. L. F. Li, K. I. Mohr, G. M. Skofronick-Jackson, C. D. Peters-Lidard, 2016: Performance of the Goddard multiscale modeling framework with Goddard ice microphysical schemes. *Journal of Advances in Modeling Earth Systems*, 8, 66–95, https://doi.org/10.1002/2015MS000469.

Clark, S., S. A. Sisson, A. Sharma, 2016: A dimension range representation (DRR) measure for self-organizing maps. *Pattern Recognition*, 53, 276–286, https://doi.org/10.1016/J.PATCOG.2015.11.002.

Colle, B. A., D. Stark, S. E. Yuter, 2014: Surface microphysical observations within East Coast winter storms on Long Island, New York. *Monthly Weather Review*, 142, 3126–3146, https://doi.org/10.1175/MWR-D-14-00035.1.

Deierling, W., Petersen, W.A., Latham, J., Ellis, S., Christian, H.J., 2008. The relationship between lightning activity and ice fluxes in thunderstorms. *Journal of Geophysical Research: Atmospheres*, 113, 15210. https://doi.org/10.1029/2007JD009700

Dennis, E.J., Kumjian, M.R., 2017: The Impact of Vertical Wind Shear on Hail Growth in Simulated Supercells. *Journal of the Atmospheric Sciences*, 74, 641–663. https://doi.org/10.1175/JAS-D-16-0066.1

Dobber, M., J. Grandell, 2014: Meteosat Third Generation (MTG) Lightning Imager (LI) instrument performance and calibration from user perspective. Proc. 23rd Conf. on Characterization and Radiometric Calibration for Remote Sensing (CALCON), Logan, UT, Utah State University, 13 pp., https://digitalcommons.usu.edu/cgi/viewcontent.cgi?filename=0&article=1088&context=calcon&type=additional.

Dolan, B., Rutledge, S. A., Lim, S., Chandrasekar, V., Thurai, M., 2013: A robust C-band hydrometeor identification algorithm and application to a long-term polarimetric radar dataset. *Journal of Applied Meteorology and Climatology*, 52(9), 2162–2186. https://doi.org/10.1175/JAMC-D-12-0275.1

Dye, J.E., Jones, J.J., Winn, W.P., Cerni, T.A., Gardiner, B., Lamb, D., Pitter, R.L., Hallett, J., Saunders, C.P.R., 1986: Early electrification and precipitation development in a small, isolated Montana cumulonimbus. *Journal of Geophysical Research: Atmospheres*, 91, 1231–1247. https://doi.org/10.1029/JD091ID01P01231

Emersic, C., Heinselman, P.L., MacGorman, D.R., Bruning, E.C., 2011: Lightning Activity in a Hail-Producing Storm Observed with Phased-Array Radar. *Monthly Weather Review,* 139, 1809–1825. https://doi.org/10.1175/2010MWR3574.1

Erdmann, F., Poelman, D. R. 2023: Automated Lightning Jump (LJ) Detection from Geostationary Satellite Data. *Journal of Applied Meteorology and Climatology*, 62(11), 1573–1590. https://doi.org/10.1175/JAMC-D-22-0144.1

Fabry, F., W. Szyrmer, 1999: Modeling of the Melting Layer. Part II: Electromagnetic. *Journal of the Atmospheric Sciences*, 56, 3593–3600, https://doi.org/10.1175/1520-0469(1999)056%3C3593:MOTMLP%3E2.0.CO;2

Fan, J., Han, B., Varble, A., Morrison, H., North, K., Kollias, P., Chen, B., Dong, X., Giangrande, S. E., Khain, A., Lin, Y., Mansell, E., Milbrandt, J. A., Stenz, R., Thompson, G., Wang, Y. 2017: Cloud-resolving model intercomparison of an MC3E squall line case: Part I—Convective updrafts. *Journal of Geophysical Research: Atmospheres*, 122(17), 9351–9378. https://doi.org/10.1002/2017JD026622

Farnell, C., Rigo, T., Pineda, N. 2017: Lightning jump as a nowcast predictor: Application to severe weather events in Catalonia. *Atmospheric Research*, 183, 130–141. https://doi.org/10.1016/J.ATMOSRES.2016.08.021

Farnell, C., T. Rigo, 2020: The lightning jump algorithm for nowcasting convective rainfall in Catalonia. *Atmosphere*, 11, 397, https://doi.org/10.3390/ATMOS11040397.

Ferrier, B. S., 1994: A double-moment multiple-phase four-class bulk ice scheme. Part I: description. *Journal of the Atmospheric Sciences*, 51, 249–280.

Fierro, A. O., Mansell, E. R., Macgorman, D. R., Ziegler, C. L. 2013: The implementation of an explicit charging and discharge lightning scheme within the WRF-ARW model: Benchmark simulations of a continental squall line, a tropical cyclone, and a winter storm. *Monthly Weather Review*, 141(7), 2390–2415. https://doi.org/10.1175/MWR-D-12-00278.1

Fovell, R.G., Ogura, Y., 1988: Numerical Simulation of a Midlatitude Squall Line in Two Dimensions. *Journal of the Atmospheric Sciences* 45, 3846–3879. https://doi.org/10.1175/1520-0469(1988)045

Fujita, 1992: The mystery of severe storms. WRL Research Paper 239, University of Chicago, 298 pp.

Fujita, T. T., 1985: The downburst: Microburst and macroburst. University of Chicago SMRP Research Paper 210, 122 pp.

Fujita, T. T., H. R. Byers, 1977: Spearhead echo and downburst in the crash of an airliner. *Monthly Weather Review*, 105, 129–146, https://doi.org/10.1175/1520-0493(1977)105<0129:SEADIT>2.0.CO;2.

Fukuta, N., Takahashi, T., 1999: The Growth of Atmospheric Ice Crystals: A Summary of Findings in Vertical Supercooled Cloud Tunnel Studies. *Journal of the Atmospheric Sciences*, 56(12), 1963–1979. https://doi.org/10.1175/1520-0469(1999)056

Gao, J-D., M. Xue, K. Brewster, K. K. Droegemeier, 2004: A three-dimensional variational data analysis method with recursive filter for Doppler radars. *Journal of Atmospheric and Oceanic Technology*, 21 , 457–469. https://doi.org/10.1175/1520-0426(2004)021%3C0457:ATVDAM%3E2.0.CO;2

Gatlin, P. N., S. J. Goodman, 2010: A total lightning trending algorithm to identify severe thunderstorms. *Journal of Atmospheric and Oceanic Technology*, 27, 3–22, https://doi.org/10.1175/2009JTECHA1286.1.

Gharaylou, M., Pegahfar, N., Farahani, M. M., 2020: Influence of tilting effect on charge structure and lightning flash density in two different convective environments. *Meteorological Applications*, 27(5), e1957. https://doi.org/10.1002/MET.1957

Gilmore, M.S., Straka, J.M., Rasmussen, E.N., 2004: Precipitation Uncertainty Due to Variations in Precipitation Particle Parameters within a Simple Microphysics Scheme. *Monthly Weather Review,* 132, 2610–2627. https://doi.org/10.1175/MWR2810.1

Giorgetta, M. A., Brokopf, R., Crueger, T., Esch, M., Fiedler, S., Helmert, J., Hohenegger, C., Kornblueh, L., Köhler, M., Manzini, E., Mauritsen, T., Nam, C., Raddatz, T., Rast, S., Reinert, D., Sakradzija, M., Schmidt, H., Schneck, R., Schnur, R., … Stevens, B. (2018). ICON-A, the Atmosphere Component of the ICON Earth System Model: I. Model Description. *Journal of Advances in Modeling Earth Systems*, 10(7), 1613–1637. https://doi.org/10.1029/2017MS001242

Goodman, S. J., Blakeslee, R. J., Koshak, W. J., Mach, D., Bailey, J., Buechler, D., Carey, L., Schultz, C., Bateman, M., McCaul, E., Stano, G., 2013: The GOES-R Geostationary Lightning Mapper (GLM). *Atmospheric Research*, 125–126, 34–49. https://doi.org/10.1016/J.ATMOSRES.2013.01.006

Goodman, S. J., Buechler, D. E., Wright, P. D., Rust, W. D., 1988: Lightning and precipitation history of a microburst-producing storm. *Geophysical Research Letters*, 15(11), 1185–1188. https://doi.org/10.1029/GL015I011P01185

Goodman, S.J., Blakeslee, R., Christian, H., Koshak, W., Bailey, J., Hall, J., McCaul, E., Buechler, D., Darden, C., Burks, J., Bradshaw, T., Gatlin, P., 2005: The North Alabama Lightning Mapping Array: Recent severe storm observations and future prospects. *Atmospheric Research*, 76, 423–437. https://doi.org/10.1016/J.ATMOSRES.2004.11.035

Grabowski, W. W., 1998: Toward cloud resolving modeling of large-scale tropical circulations: A simple cloud microphysics parameterization. *Journal of the Atmospheric Sciences*, 55, 3283–3298, https://doi.org/10.1175/1520-0469(1998)055%3C3283:TCRMOL%3E2.0.CO;2.

Grazioli, J., Tuia, D., Monhart, S., Schneebeli, M., Raupach, T., Berne, A., 2014: Hydrometeor classification from two-dimensional video disdrometer data. *Atmospheric Measurement Techniques*, 7(9), 2869-2882. https://doi.org/10.5194/amt-7-2869-2014

Guo, X., Niino, H., Guo, X., Kimura, R., 1999: Numerical modeling on a hazardous microburst-producing hailstorm. Science Press.

Hall, M. P. M., J. W. F. Goddard, S. M. Cherry, 1984: Identification of hydrometeors and other targets by dual-polarization radar. *Radio Science*, 19, 132–140, https://doi.org/10.1029/RS019I001P00132.

Hara, Y., Suzuki, K., Kawano, T., 2024: Quantitative Evaluation of Graupel Shape Observed by New Particle Imaging Radiosonde, Rainscope – A Case Study of a Convective Cloud on 25 June 2022. *Scientific Online Letters on the Atmosphere*, 20(0), 184–190. https://doi.org/10.2151/SOLA.2024-025

Harimaya, T., 1976: The embryo and formation of graupel. *Journal of the Meteorological Society of Japan Ser. II,* 54, 42–51, https://doi.org/10.2151/jmsj1965.54.1_42.

Harimaya, T., Kanemura, N., 1995: Comparison of the Riming Growth of Snow Particles between Coastal and Inland Areas. *Journal of the Meteorological Society of Japan*, 73(1), 25–36. https://doi.org/10.2151/JMSJ1965.73.1_25

Hashino, T., M. Satoh, Y. Hagihara, T. Kubota, T. Matsui, T. Nasuno, H. Okamoto, 2013: Evaluating cloud microphysics from NICAM against CloudSat and CALIPSO. *Journal of Geophysical Research: Atmospheres*, 118, 7273–7292, https://doi.org/10.1002/jgrd.50564.

Heckman, S., 2014: ENTLN status update. In XV International Conference on Atmospheric Electricity, 15-20 June 24, Norman, Oklahoma.

Heymsfield, A. J., A. Bansemer, S. Lewis, J. Iaquinta, M. Kajikawa, C. Twohy, M. R. Poellot, L. M. Miloshevich, 2002: A general approach for deriving the properties of cirrus and stratiform ice cloud particles. *Journal of the Atmospheric Sciences*, 59, 3–29. https://doi.org/10.1175/1520-0469(2002)059<0003:AGAFDT>2.0.CO;2

Hjelmfelt, M. R., 1988: Structure and life cycle of microburst outflows observed in Colorado. *Journal of Applied Meteorology and Climatology*, 27, 900–927, https://doi.org/10.1175/1520-0450(1988)027<0900:SALCOM>2.0.CO;2.

Hou, T., Lei, H., Yang, J., Hu, Z., Feng, Q., 2016: Investigation of riming within mixed-phase stratiform clouds using Weather Research and Forecasting (WRF) model. *Atmospheric Research*, 178–179, 291–303. https://doi.org/10.1016/J.ATMOSRES.2016.04.007

Iguchi, T., T. Matsui, J. J. Shi, W.-K. Tao, A. P. Khain, A. Hou, R. Cifelli, A. Heymsfield, A. Tokay, 2012: Numerical analysis using WRF-SBM for the cloud microphysical structures in the C3VP field campaign: Impacts of supercooled droplets and resultant riming on snow microphysics. *Journal of Geophysical Research Atmospheres*, 117, 1–22, https://doi.org/10.1029/2012JD018101.

Iguchi, T., T. Nakajima, A. P. Khain, K. Saito, T. Takemura, H. Okamoto, T. Nishizawa, W. K. Tao, 2012: Evaluation of cloud microphysics in JMA-NHM simulations using bin or bulk microphysical schemes through comparison with cloud radar observations. *Journal of the Atmospheric Sciences*, 69, 2566–2586, https://doi.org/10.1175/JAS-D-11-0213.1.

Inatsu, M., S. Tanji, Y. Sato, 2020: Toward predicting expressway closures due to blowing snow events. *Cold Regions Science and Technology*, 177, https://doi.org/10.1016/j.coldregions.2020.103123.

Ishii, K., Hayashi, S., Fujibe, F., 2014: Statistical analysis of temporal and spatial distributions of cloud-to-ground lightning in Japan from 2002 to 2008. *Journal of Atmospheric Electricity*, 34(2), 79–86. https://doi.org/10.1541/JAE.34.79

Ishizaka, M., H. Motoyoshi, S. Nakai, T. Shiina, T. Kumakura, K. I. Muramoto, 2013: A new method for identifying the main type of solid hydrometeors contributing to snowfall from measured size-fall speed relationship. *Journal of the Meteorological Society of Japan*, 91, 747–762, https://doi.org/10.2151/jmsj.2013-602.

Japan Meteorological Agency (JMA), 2019: Outline of the operational numeircal weather prediction at the Japan Meteorological Agency https://www.jma.go.jp /jma/jma-eng/jma-center/nwp/outline2019-nwp/index.htm (Accessed on Jan 21st, 2021)

Jayaratne, E.R., Saunders, C.P.R., 2016: The interaction of ice crystals with hailstones in wet growth and its possible role in thunderstorm electrification. *Quarterly Journal of the Royal Meteorological Society*, 142, 1809–1815.

https://doi.org/10.1002/QJ.2777

Jewell, R., Brimelow, J., 2009: Evaluation of Alberta hail growth model using severe hail proximity soundings from the United States. *Weather and Forecasting*, 24(6), 1592–1609. https://doi.org/10.1175/2009WAF2222230.1

Jessup, S. M., Burke, A. L., 2018: Predicting microbursts in the northeastern U.S. using lightning flash rates and simple radar parameters. *Advances in Meteorology*, 2018. https://doi.org/10.1155/2018/3639215

Katsuyama Y. M. Inatsu 2021:Advantage of volume scanning video disdrometer in solid-precipitation observation, *Scientific Online Letters on the Atmosphere*, 17, 35-40, https://doi.org/10.2151/sola.2021-006.

Katsuyama, Y., M. Inatsu, 2020: Fitting precipitation particle size–velocity data to mixed joint probability density function with an expectation maximization algorithm. *Journal of Atmospheric and Oceanic Technology.*, 37, 911–925, https://doi.org/10.1175/JTECH-D-19-0150.1.

Katsuyama, Y., M. Inatsu, 2021: Advantage of volume scanning video disdrometer in solid-precipitation observation. *Scientific Online Letters on the Atmosphere*., 17, 35–40, https://doi.org/10.2151/SOLA.2021-006.

Kawazoe, S., Fujita, M., Sugimoto, S., Okada, Y., Watanabe, S., 2020: Projected Changes of Extremely Cool Summer Days over Northeastern Japan Simulated by 20 km-mesh Large Ensemble Experiment. *Journal of the Meteorological Society of Japan. Ser. II*, 98(6), 1305–1319. https://doi.org/10.2151/JMSJ.2020-067

Keith Wilson, D., 2001: An alternative function for the wind and temperature gradients in unstable surface layers. *Boundary-Layer Meteorology*, 99, 151–158, https://doi.org/10.1023/A:1018718707419.

Kessler, E., 1969: On the distribution and continuity of water substance in atmospheric circulations. *American Meteorological Society*, 84 pp.

Kikuchi, K., T. Kameda, K. Higuchi, and A. Yamashita, 2013: A global classification of snow crystals, ice crystals, and solid precipitation based on observations from middle latitudes to polar regions. *Atmospheric Research*., 132–133, 460–472, https://doi.org/10.1016/j.atmosres.2013.06.006.

Knight, C. A., N. C. Knight, 1973: Conical graupel. *Journal of the Atmospheric Sciences*, 30. 118-124, https://doi.org/10.1175/1520-0469(1973)030%3C0118:CG%3E2.0.CO;2

Knupp, K.R., Murphy, T.A., Coleman, T.A., Wade, R.A., Mullins, S.A., Schultz, C.J., Schultz, E. V., Carey, L., Sherrer, A., McCaul, E.W., Carcione, B., Latimer, S., Kula, A., Laws, K., Marsh, P.T., Klockow, K., 2014: Meteorological Overview of the Devastating 27 April 2011 Tornado Outbreak. *Bulletin of the American Meteorological Society*. 95, 1041–1062. https://doi.org/10.1175/BAMS-D-11-00229.1

Kohonen, T., 2013: Essentials of the self-organizing map. *Neural Networks*, 37, 52–65. https://doi.org/10.1016/J.NEUNET.2012.09.018

Kohonen, T., 1995: Self-Organizing Maps. *Springer Series in Information Sciences*. Vol. 30, Springer-Verlag, 362 p.

Kondo, M., Y. Sato, M. Inatsu, Y. Katsuyama, 2021: Evaluation of cloud microphysical schemes for winter snowfall events in Hokkaido: A case study of snowfall by winter monsoon. *Scientific Online Letters on the Atmosphere*, 17, 74–80, https://doi.org/10.2151/sola.2021-012.

Kondo, M., Y. Sato, M. Inatsu, Y. Katsuyama, 2024: Development of an evaluation method for precipitation particle types by using disdrometer data. *Journal of Atmospheric and Oceanic Technology*, **41**, 1229–1246, https://doi.org/10.1175/JTECH-D-23-0089.1

Kondo, M., Y. Sato, 2024: Transition of Dominant Cloud Microphysical Processes for Increasing Lightning Preceding Downbursts in Multi-cell Convective Clouds, in revision

Korolev, A., 2007: Limitations of the Wegener–Bergeron–Findeisen Mechanism in the Evolution of Mixed-Phase Clouds. *Journal of the Atmospheric Sciences*, 64, 3372–3375. https://doi.org/10.1175/JAS4035.1

Korolev, A., McFarquhar, G., Field, P. R., Franklin, C., Lawson, P., Wang, Z., Williams, E., Abel, S. J., Axisa, D., Borrmann, S., Crosier, J., Fugal, J., Krämer, M., Lohmann, U., Schlenczek, O., Schnaiter, M., Wendisch, M., 2017: Mixed-Phase Clouds: Progress and Challenges. *Meteorological Monographs*, 58(1), 5.1-5.50. https://doi.org/10.1175/AMSMONOGRAPHS-D-17-0001.1

Korolev, A., Milbrandt, J., 2022: How Are Mixed-Phase Clouds Mixed? *Geophysical Research Letters*, 49(18), e2022GL099578. https://doi.org/10.1029/2022GL099578

Korolev, A. V., Isaac, G. A., Cober, S. G., Strapp, J. W., Hallett, J., 2003: Microphysical characterization of mixed-phase clouds. *Quarterly Journal of the Royal Meteorological Society*, 129(587), 39–65. https://doi.org/10.1256/QJ.01.204

Koshak, W.J., Solakiewicz, R.J., Blakeslee, R.J., Goodman, S.J., Christian, H.J., Hall, J.M., Bailey, J.C., Krider, E.P., Bateman, M.G., Boccippio, D.J., Mach, D.M., McCaul, E.W., Stewart, M.F., Buechler, D.E., Petersen, W.A., Cecil, D.J., 2004: North Alabama Lightning Mapping Array (LMA): VHF source retrieval algorithm and error analyses. *Journal of Atmospheric and Oceanic Technology,* 21, 543 – 558., https://doi.org/10.1175/1520-0426(2004)021%3C0543:NALMAL%3E2.0.CO;2

Kouketsu, T., Uyeda, H., Ohigashi, T., Oue, M., Takeuchi, H., Shinoda, T., Tsuboki, K., Kubo, M., Muramoto, K. ichiro., 2015: A Hydrometeor Classification Method for X-Band Polarimetric Radar: Construction and Validation Focusing on Solid Hydrometeors under Moist Environments. *Journal of Atmospheric and Oceanic Technology*, 32(11), 2052–2074. https://doi.org/10.1175/JTECH-D-14-00124.1

Krehbiel, P.R., Thomas, R.J., Rison, W., Hamlin, T., Harlin, J., Davis, M., 2000: GPS-based mapping system reveals lightning inside storms. Eos, T*ransactions American Geophysical Union*, 81, 21–25. https://doi.org/10.1029/00EO00014

Kruger, A., W. F. Krajewski, 2002: Two-dimensional video disdrometer: A description. *Journal of Atmospheric and Oceanic Technology*, 19, 602–617, https://doi.org/10.1175/1520-0426(2002)019<0602:TDVDAD>2.0.CO;2.

Kumjian, M.R., Deierling, W., 2015: Analysis of Thundersnow Storms over Northern Colorado. *Weather and Forecast*, 30, 1469–1490. https://doi.org/10.1175/WAF-D-15-0007.1

Kumjian, M.R., Ryzhkov, A. V., 2008: Polarimetric Signatures in Supercell Thunderstorms. *Journal of Applied Meteorology and Climatology,* 47, 1940–1961. https://doi.org/10.1175/2007JAMC1874.1

Kusaka, H., H. Kondo, Y. Kikegawa, F. Kimura, 2001: A simple single-layer urban canopy model for atmospheric models: Comparison with multi-layer and slab models. *Boundary-Layer Meteorology*, 101, 329–358, https://doi.org/10.1023/A:1019207923078.

Lawson, R. P., Gettelman, A., 2014: Impact of Antarctic mixed-phase clouds on climate. *Proceedings of the National Academy of Sciences of the United States of America*, 111(51), 18156–18161. https://doi.org/10.1073/PNAS.1418197111/ASSET/5F718243-1022-4A37-B4E4-F9E6416CF14D/ASSETS/GRAPHIC/PNAS.1418197111FIG04.JPEG

Lebo, Z. J., Morrison, H., 2014: Dynamical effects of aerosol perturbations on simulated idealized squall lines. *Monthly Weather Review*, 142(3), 991–1009. https://doi.org/10.1175/MWR-D-13-00156.1

Lee, J. E., Jung, S. H., Park, H. M., Kwon, S., Lin, P. L., Lee, G., 2015: Classification of precipitation types using fall velocity-diameter relationships from 2D-video disdrometer measurements. *Advances in Atmospheric Sciences*, 32, 1277-1290. https://doi.org/10.1007/s00376-015-4234-4

Lin, Y. L., Farley, R. D., Orville, H. D., 1983: Bulk parameterization of the snow field in a cloud model. *Journal of Climate and Applied Meteorology,* 22(6), 1065–1092. https://doi.org/10.1175/1520-0450(1983)022<1065:BPOTSF>2.0.CO;2

Lin, Y., Kumjian, M. R., 2022: Influences of CAPE on hail production in simulated supercell storms. *Journal of the Atmospheric Sciences*, 79(1), 179–204. https://doi.org/10.1175/JAS-D-21-0054.1

List, R., 1961: Physical Methods and Instruments for Characterizing Hailstones. *Bulletin of the American Meteorological Society,* 42, 452–466. https://doi.org/10.1175/1520-0477-42.7.452

List, R., J. Hallett, J. Warner, and R. Reinking, 1986: The future of laboratory research and facilities for cloud physics and cloud chemistry: Report on a technical workshop held in Boulder, Colorado, 20–22 March 1985. *Bulletin of the American Meteorological Society*, 67, 1389–1397, https://doi.org/10.1175/1520-0477-67.11.1389.

List, R., 1990: Physics of supercooling of thin water skins covering gyrating hailstones. *Journal of the Atmospheric Sciences*, 47, 1919–1925, https://doi.org/10.1175/1520-0469(1990)047%3C1919:POSOTW%3E2.0.CO;2.

List, R., 2014: New Hailstone Physics. Part I: Heat and Mass Transfer (HMT) and Growth. *Journal of the Atmospheric Sciences*, 71, 1508–1520. https://doi.org/10.1175/JAS-D-12-0164.1

Liu, H., Chandrasekar, V., 2000: Classification of hydrometeors based on polarimetric radar measurements: Development of fuzzy logic and neuro-fuzzy systems, and in situ verification. *Journal of Atmospheric and Oceanic Technology*, 17, 140–164. https://doi.org/10.1175/1520-0426(2000)017<0140:COHBOP>2.0.CO;2

Locatelli, J. D., P. V. Hobbs, 1974: Fall speeds and masses of solid precipitation particles. *Journal of Geophysical Research*, 79, 2185–2197, https://doi.org/10.1029/jc079i015p02185.

Löffler-Mang, M., J. Joss, 2000: An optical disdrometer for measuring size and velocity of hydrometeors. *Journal of Atmospheric and Oceanic Technology*, 17, 130–139, https://doi.org/10.1175/1520-0426(2000)017<0130:AODFMS>2.0.CO;2.

Luque, M. Y., Bürgesser, R. E., Ruiz, J. J., 2023: Study of the correlation between electrical activity and the microphysics and dynamics of a real severe event using the WRF-ELEC model. *Quarterly Journal of the Royal Meteorological Society*, 149(753), 1520−1539. https://doi.org/10.1002/QJ.4471

MacGorman, D. R., W. D. Rust, 1998: The Electrical Nature of Storms, Oxford Univ. Press, New York, 422 pp.

MacGorman, D.R., Rust, W.D., Krehbiel, P., Rison, W., Bruning, E., Wiens, K., 2005: The Electrical Structure of Two Supercell Storms during STEPS. *Monthly Weather Review,* 133, 2583–2607. https://doi.org/10.1175/MWR2994.1

Macklin, W. C., 1962: The density and structure of ice formed by accretion. *Quarterly Journal of the Royal Meteorological Society*, 88, 30–50. https://doi.org/10.1002/qj.49708837504

Magono, C., C. Lee, 1966: Meteorological classification of natural snow crystals. Meteorological classification of natural snow crystals. *Journal of the Faculty of Science, Hokkaido University, Ser. VII 4*, 321–335 (with Plates 27) II.

Magono, C., K. Kikuchi, T. Kimura, S. Tazawa, T. Kasal, 1966: A study on the snowfall in the winter monsoon season in Hokkaido with special reference to low land snowfall (Investigation of natural snow crystals VI). *Journal of the Faculty of Science, Hokkaido University Ser. 7*, 11, 287–308.

Makihara, Y., N. Uekiyo, A. Tabata, Y. Abe, 1996: Accuracy of radar-AMeDAS precipitation. *IEICE Transactions on Communications*, E79-B, 751-762.

Marzano, F. S., D. Scaranari, M. Montopoli, G. Vulpiani, 2008: Supervised classification and estimation of hydrometeors from C-band dual-polarized radars: A Bayesian approach. *IEEE Transactions on Geoscience and Remote Sensing*, 46, 85–98, https://doi.org/10.1109 / TGRS.2007.906476.

Matrosov, S. Y., Shupe, M. D., Uttal, T., 2022: High temporal resolution estimates of Arctic snowfall rates emphasizing gauge and radar-based retrievals from the MOSAiC expedition. *Elementa*, 10(1). https://doi.org/10.1525/ELEMENTA.2021.00101/124572

Milbrandt, J. A., A. Glazer, D. Jacob, 2012: Predicting the snow-to-liquid ratio of surface precipitation using a bulk microphysics scheme. *Monthly Weather Review*, 140, 2461–2476, https://doi.org/10.1175/MWR-D-11-00286.1.

Minda, H., N. Tsuda, and Y. Fujiyoshi, 2017: Three-Dimensional Shape and Fall Velocity Measurements of Snowflakes Using a Multiangle Snowflake Imager. *Journal of Atmospheric and Oceanic Technology*, 34, 1763–1781, https://doi.org/10.1175/JTECH-D-16-0221.1.

Mitchell, D. L., 1996: Use of mass- and area-dimensional power laws for determining precipitation particle terminal velocities. *Journal of the Atmospheric Sciences*, 53, 1710–1723, https://doi.org/10.1175/1520-0469(1996)053<1710:UOMAAD>2.0.CO;2.

Mitchell, D. L., A. J. Heymsfield, 2005: The treatment of ice particle terminal velocities, highlighting aggregates. J*ournal of the Atmospheric Sciences*, 62, 1637–1644. https://doi.org/10.1175/JAS3413.1

Miyamoto, Y., 2021: Effects of Number Concentration of Cloud Condensation Nuclei on Moist Convection Formation. *Journal of the Atmospheric Sciences,* 78, 3401–3413. https://doi.org/10.1175/JAS-D-21-0058.1

Mizuno, H., 1992: Statistical characteristics of graupel precipitation over the Japan

Islands. *Journal of the Meteorological Society of Japan*, 70, 115–121, https://doi.org/10.2151/JMSJ1965.70.1_115.

Molthan, A. L., B. A. Colle, 2012: Comparisons of single- and double-moment microphysics schemes in the simulation of a synoptic-scale snowfall event. *Monthly Weather Review*, 140, 2982–3002, https://doi.org/10.1175/MWR-D-11-00292.1.

Molthan, A. L., B. A. Colle, S. E. Yuter, D. Stark, 2016: Comparisons of modeled and observed reflectivities and fall speeds for snowfall of varied riming degrees during winter storms on long Island, New York. *Monthly Weather Review*, 144, 4327–4347, https://doi.org/10.1175/MWR-D-15-0397.1.

Morrison, H, and Coauthors, 2020: Confronting the challenge of modeling cloud and precipitation microphysics. *Journal of Advances in Modeling Earth Systems*, https://doi.org/10.1029/2019MS001689.

Morrison, H., J. A. Curry, V. I. Khvorostyanov, 2005: A new double-moment microphysics parameterization for application in cloud and climate models. Part I: Description. *Journal of the Atmospheric Sciences*, 62, 1665–1677, https://doi.org/10.1175/JAS3446.1.

Morrison, H., De Boer, G., Feingold, G., Harrington, J., Shupe, M. D., Sulia, K., 2011: Resilience of persistent Arctic mixed-phase clouds. *Nature Geoscience*, 5(1), 11–17. https://doi.org/10.1038/ngeo1332

Morrison, H., Milbrandt, J. A., 2015: Parameterization of Cloud Microphysics Based on the Prediction of Bulk Ice Particle Properties. Part I: Scheme Description and Idealized Tests. *Journal of the Atmospheric Sciences*, 72(1), 287–311. https://doi.org/10.1175/JAS-D-14-0065.1

Murakami, M., T. Matsuo, 1990: Development of the Hydrometeor Videosonde. *Journal of Atmospheric and Oceanic Technology*, 7, 613-620, https://doi.org/10.1175/1520-0426(1990)007<0613:DOTHV>2.0.CO;2

Murakami, M., 2019: Inner structures of snow clouds over the Sea of Japan observed by instrumented aircraft: A Review. *Journal of the Meteorological Society of Japan*, 97, 5–38, https://doi.org/10.2151/JMSJ.2019-009.

Muramoto, K., T. Shiina, T. Endo, H. Konishi, K. Kitano, 1989: Measurement of snowflake size and falling velocity by image processing. *Proceedings of the NIPR Symposium on Polar Meteorology and Glaciology*, 2, 54. https://doi.org/10.15094/00003563

Nakajima, T., M. Tanaka, 1986: Matrix formulations for the transfer of solar radiation in a plane-parallel scattering atmosphere. *Journal of Quantitative Spectroscopy and Radiative Transfer*, 35, 13–21, https://doi.org/10.1016/0022-4073(86)90088-9.

Nakajima, T., M. Tanaka, 1988: Algorithms for radiative intensity calculations in moderately thick atmospheres using a truncation approximation. *Journal of Quantitative Spectroscopy and Radiative Transfer,* 40, 51–69, https://doi.org/10.1016/0022-4073(88)90031-3.

Nakanishi, M., H. Niino, 2004: An improved Mellor-Yamada Level-3 model with condensation physics: Its design and verification. *Boundary-Layer Meteorology*, 112, 1–31, https://doi.org/10.1023/B:BOUN.0000020164.04146.98.

Nakanishi, M., Niino, H., 2009: Development of an Improved Turbulence Closure Model for the Atmospheric Boundary Layer. *Journal of the Meteorological Society of Japan*, 87(5), 895–912. https://doi.org/10.2151/JMSJ.87.895

Nelson, S.P., 1987: The hybrid multicellular–supercellular storm — an efficient hail producer. Part II: general characteristics and implications for hail growth. *Journal of the Atmospheric Sciences*, 44, 2060–2073, https://doi.org/10.1175/1520-0469(1987)044%3C2060:THMSEH%3E2.0.CO;2

Ni, X., Huang, F., Hui, W., Xiao, H., 2023: Lightning Evolution in Hailstorms From the Geostationary Lightning Mapper Over the Contiguous United States. *Journal of Geophysical Research: Atmospheres*, 128, e2023JD038578. https://doi.org/10.1029/2023JD038578

Nishiyama, K., Endo, S., Jinno, K., Bertacchi Uvo, C., Olsson, J., Berndtsson, R., 2007: Identification of typical synoptic patterns causing heavy rainfall in the rainy season in Japan by a Self-Organizing Map. *Atmospheric Research*, 83(2–4), 185–200. https://doi.org/10.1016/J.ATMOSRES.2005.10.015

Nishizawa, S., H. Yashiro, Y. Sato, Y. Miyamoto, H. Tomita, 2015: Influence of grid aspect ratio on planetary boundary layer turbulence in large-eddy simulations. *Geoscientific Model Development*, 8, 3393–3419, https://doi.org/10.5194/gmd-8-3393-2015.

Nixon, C. J., Allen, J. T., Taszarek, M., 2023: Hodographs and skew Ts of hail-producing storms. *Weather and Forecasting*, 38(11), 2217–2236. https://doi.org/10.1175/WAF-D-23-0031.1

Nowotarski, C. J., Jensen, A. A. 2013: Classifying Proximity Soundings with Self-Organizing Maps toward Improving Supercell and Tornado Forecasting. *Weather and Forecasting*, 28(3), 783–801. https://doi.org/10.1175/WAF-D-12-00125.1

Oraltay, R. G., Hallett, J., 1989: Evaporation and melting of ice crystals: A laboratory study. *Atmospheric Research*, 24(1–4), 169–189. https://doi.org/10.1016/0169-8095(89)90044-6

Orville, R. E., 2008: Development of the National Lightning Detection Network. *Bulletin of the American Meteorological Society*, 89, 180–190, https://doi.org/10.1175/BAMS-89-2-180.

Park, H. S., Ryzhkov, A. V., Zrnić, D. S., Kim, K. E., 2009: The Hydrometeor Classification Algorithm for the Polarimetric WSR-88D: Description and Application to an MCS. *Weather and Forecasting*, 24(3), 730–748. https://doi.org/10.1175/2008WAF2222205.1

Pettersen, C., Bliven, L. F., Kulie, M. S., Wood, N. B., Shates, J. A., Anderson, J., Mateling, M. E., Petersen, W. A., von Lerber, A., Wolff, D. B., 2021: The Precipitation Imaging Package: Phase Partitioning Capabilities. *Remote Sensing*, 13, 2183, https://doi.org/10.3390/RS13112183.

Pettersen, C., Bliven, L. F., Von Lerber, A., Wood, N. B., Kulie, M. S., Mateling, M. E., Moisseev, D. N., Munchak, S. J., Petersen, W. A., & Wolff, D. B.Coauthors, 2020a: The Precipitation Imaging Package: Assessment of Microphysical and Bulk Characteristics of Snow. *Atmosphere*, 11, 785, https://doi.org/10.3390/ATMOS11080785.

Pettersen, C., M. S. Kulie, L. F. Bliven, A. J. Merrelli, W. A. Petersen, T. J. Wagner, D. B. Wolff, and N. B. Wood, 2020b: A Composite Analysis of Snowfall Modes from Four Winter Seasons in Marquette, Michigan. *Journal of Applied Meteorology and Climatology*, 59, 103–124, https://doi.org/10.1175/JAMC-D-19-0099.1.

Pflaum, J., H. R. Pruppacher., 1979: A wind tunnel investigation of the growth of graupel initiated from frozen drops. *Journal of Atmospheric Sciences*, 680–689. https://doi.org/10.1175/1520-0469(1979)036<0680:AWTIOT>2.0.CO;2

Phillips, V. T. J., Formenton, M., Bansemer, A., Kudzotsa, I., Lienert, B., 2015: A Parameterization of Sticking Efficiency for Collisions of Snow and Graupel with Ice Crystals: Theory and Comparison with Observations. *Journal of the Atmospheric Sciences*, 72(12), 4885–4902. https://doi.org/10.1175/JAS-D-14-0096.1

Phillips, V. T. J., Formenton, M., Kanawade, V. P., Karlsson, L. R., Patade, S., Sun, J., Barthe, C., Pinty, J. P., Detwiler, A. G., Lyu, W., Tessendorf, S. A., 2020: Multiple Environmental Influences on the Lightning of Cold-Based Continental Cumulonimbus Clouds. Part I: Description and Validation of Model. *Journal of the Atmospheric Sciences*, 77(12), 3999–4024. https://doi.org/10.1175/JAS-D-19-0200.1

Praz, C., Y. A. Roulet, and A. Berne, 2017: Solid hydrometeor classification and riming degree estimation from pictures collected with a Multi-Angle Snowflake Camera. *Atmospheric Measurement Techniques*, 10, 1335–1357, https://doi.org/10.5194/AMT-10-1335-2017.

Proctor de., 1971: A hyperbolic system for obtaining VHF radio pictures of lightning. *Journal of Geophysical Research*, 76(6), 1478–1489. https://doi.org/10.1029/JC076I006P01478

Pruppacher, H. R., J. D. Klett, 1997: Microphysics of clouds and precipitation. 2nd Edition. Kluwer Academic, 954 pp.

Reusch, D. B., Alley, R. B., Hewitson, B. C. 2007: North Atlantic climate variability from a self-organizing map perspective. *Journal of Geophysical Research: Atmospheres*, 112(D2). https://doi.org/10.1029/2006JD007460

Ribaud, J. F., O. Bousquet, S. Coquillat, H. Al-Sakka, D. Lambert, V. Ducrocq, E. Fontaine, 2016: Evaluation and application of hydrometeor classification algorithm outputs inferred from multi-frequency dual-polarimetric radar observations collected during HyMeX. *Quarterly Journal of the Royal Meteorological Society,* 142, 95–107, https://doi.org/10.1002/QJ.2589.

Richard Rotunno, Joseph B. Klemp, Morris L. Weisman., 1988: A theory for strong, long-lived squall lines. *Journal of the Atmospheric Sciences*, 45, 463–485. https://doi.org/10.1175/1520-0469(1988)045<0463:ATFSLL>2.0.CO;2

Rigo, T., Farnell, C., 2022: Characterisation of thunderstorms with multiple lightning jumps. *Atmosphere*, 13(2), 171. https://doi.org/10.3390/ATMOS13020171

Roh, W., M. Satoh, 2014: Evaluation of precipitating hydrometeor parameterizations in a single-moment bulk microphysics scheme for deep convective systems over the tropical central Pacific. *Journal of the Atmospheric Sciences*, 71, 2654–2673, https://doi.org/10.1175/JAS-D-13-0252.1.

Roh, W., Satoh, M., Hashino, T., Okamoto, H., Seiki, T., 2020: Evaluations of the Thermodynamic Phases of Clouds in a Cloud-System-Resolving Model Using CALIPSO and a Satellite Simulator over the Southern Ocean. *Journal of the Atmospheric Sciences*, 77(11), 3781–3801. https://doi.org/10.1175/JAS-D-19-0273.1

Rotunno, R., Klemp, J.B., Weisman, M.L., 1988: A theory for strong, long-lived squall lines. *Journal of the Atmospheric Sciences*, 45, 463–485, https://doi.org/10.1175/1520-0469(1988)045<0463:ATFSLL>2.0.CO;2.

Rust, W. D., 1989: Utilization of a mobile laboratory for storm electricity measurements. *Journal of Geophysical Research: Atmospheres,* 94(D11), 13305–13311. https://doi.org/10.1029/JD094ID11P13305

Rutledge, S. A., P. V. Hobbs, 1984: The mesoscale and microscale structure and organization of clouds and precipitation in midlatitude cyclones. XII: A diagnostic modeling study of precipitation development in narrow cold-frontal rainbands. *Journal of the Atmospheric Sciences*, 41, 2949–2972, https://doi.org/10.1175/1520-0469(1984)041<2949:TMAMSA>2.0.CO;2.

Saito, K., T. Fujita, Y. Yamada, J. Ishida, Y. Kumagai, K. Aranami, S. Ohmori, R. Nagasawa, S. Kumagai, C. Muroi, T. Kato, H. Eito and Y. Yamazaki, 2006: The Operational JMA Nonhydrostatic Mesoscale Model. *Monthly Weather Review*, 134, 1266–1298, https://doi.org/10.1175/MWR3120.1.

Salinas, V., Bruning, E. C., Mansell, E. R., 2022: Examining the kinematic structures within which lightning flashes are initiated using a cloud-resolving model. *Journal of the Atmospheric Sciences*, 79(2), 513–530. https://doi.org/10.1175/JAS-D-21-0132.1

Sato, Y., Hayashi, S., Hashimoto, A., 2022: Difference in the lightning frequency between the July 2018 heavy rainfall event over central Japan and the 2017 northern Kyushu heavy rainfall event in Japan. *Atmospheric Science Letters* 23, e1067. https://doi.org/10.1002/ASL.1067

Sato, Y., Miyamoto, Y., Tomita, H., 2019: Large dependency of charge distribution in a tropical cyclone inner core upon aerosol number concentration. *Progress in Earth and Planetary Science*, 6(1), 1–13. https://doi.org/10.1186/S40645-019-0309-

7/FIGURES/9

Sato, Y., Nishizawa, S., Yashiro, H., Miyamoto, Y., Kajikawa, Y., Tomita, H., 2015: Impacts of cloud microphysics on trade wind cumulus: which cloud microphysics processes contribute to the diversity in a large eddy simulation? *Progress in Earth and Planetary Science*, 2(1). https://doi.org/10.1186/s40645-015-0053-6

Satoh, M., Tomita, H., Yashiro, H., Miura, H., Kodama, C., Seiki, T., Noda, A. T., Yamada, Y., Goto, D., Sawada, M., Miyoshi, T., Niwa, Y., Hara, M., Ohno, T., Iga, S. ichi, Arakawa, T., Inoue, T., Kubokawa, H., 2014: The Non-hydrostatic Icosahedral Atmospheric Model: description and development. *Progress in Earth and Planetary Science*, 1(1), 1–32. https://doi.org/10.1186/S40645-014-0018-1/TABLES/3

Saunders, C.P.R., Keith, W.D., Mitzeva, R.P., 1991: The effect of liquid water on thunderstorm charging. *Journal of Geophysical Research: Atmospheres* 96, 11007–11017. https://doi.org/10.1029/91JD00970

Schultz, C. J., Carey, L. D., Schultz, E. V., Blakeslee, R. J., 2015: Insight into the kinematic and microphysical processes that control lightning jumps. *Weather and Forecasting*, 30(6), 1591–1621. https://doi.org/10.1175/WAF-D-14-00147.1

Schultz, C. J., Carey, L. D., Schultz, E. V., Blakeslee, R. J., 2017: Kinematic and Microphysical Significance of Lightning Jumps versus Nonjump Increases in Total Flash Rate. *Weather and Forecasting*, 32(1), 275–288. https://doi.org/10.1175/WAF-D-15-0175.1

Schultz, C. J., Petersen, W. A., Carey, L. D., 2009: Preliminary development and evaluation of lightning jump algorithms for the real-time detection of severe weather. *Journal of Applied Meteorology and Climatology*, 48(12), 2543–2563.

https://doi.org/10.1175/2009JAMC2237.1

Schultz, C. J., Petersen, W. A., Carey, L. D., 2011: Lightning and severe weather: A comparison between total and cloud-to-ground lightning trends. *Weather and Forecasting*, 26(5), 744–755. https://doi.org/10.1175/WAF-D-10-05026.1

Seifert, A., K. D. Beheng, 2006: A two-moment cloud microphysics parameterization for mixed-phase clouds. Part 1: Model description. *Meteorology and Atmospheric Physics*, 92, 45–66, https://doi.org/10.1007/s00703-005-0112-4.

Seiki, T., T. Nakajima, 2014: Aerosol effects of the condensation process on a convective cloud simulation. *Journal of the Atmospheric Sciences*, 71, 833–853, https://doi.org/10.1175/JAS-D-12-0195.1.

Seiki, T., W. Roh, 2020: Improvements in super-cooled liquid water simulations of low-level mixed-phase clouds over the Southern Ocean using a single-column model. *Journal of the Atmospheric Sciences*, 77, 3803-3819, doi.org/10.1175/jas-d-19-0266.1.

Sekiguchi, M., T. Nakajima, 2008: A k-distribution-based radiation code and its computational optimization for an atmospheric general circulation model. *Journal of Quantitative Spectroscopy and Radiative Transfer*, 109, 2779–2793, https://doi.org/10.1016/j.jqsrt.2008.07.013.

Skamarock, W. C., Klemp, J. B., Duda, M. G., Fowler, L. D., Park, S. H., & Ringler, T. D., 2012: A Multiscale Nonhydrostatic Atmospheric Model Using Centroidal Voronoi Tesselations and C-Grid Staggering. *Monthly Weather Review*, 140(9), 3090–3105. https://doi.org/10.1175/MWR-D-11-00215.1

Smagorinsky, J., 1963: General circulation experiments with the primitive equations I.

The basic experiment. *Monthly Weather Review*, 91(3), 99–164. https://doi.org/10.1175/1520-0493(1963)091<0099:GCEWTP>2.3.CO;2

Smith, R. B., I. Barstad, 2004: A linear theory of orographic precipitation. *Journal of the Atmospheric Sciences*, 61, 1377–1391, https://doi.org/10.1175/1520-0469(2004)061<1377:ALTOOP>2.0.CO;2.

Solari, G., 2020: Thunderstorm Downbursts and Wind Loading of Structures: Progress and Prospect. *Frontiers in Built Environment*, 6, 519250. https://doi.org/10.3389/FBUIL.2020.00063

Suzuki, K., K. Nakagawa, T. Kawano, S. Mori, M. Katsumata, F. Syamsudin, K. Yoneyama, 2018: Videosonde-observed graupel in different rain systems during Pre-YMC Project. *Scientific Online Letters on the Atmosphere*, 14, 148–152, https://doi.org/10.2151/SOLA.2018-026.

Suzuki, K., Hara, Y., Sugidachi, T., Shimizu, K., Fujiwara, M., 2023: Development of a New Particle Imaging Radiosonde with Particle Fall Velocity Measurements in Clouds. *Scientific Online Letters on the Atmosphere*, 19(0), 261–268. https://doi.org/10.2151/SOLA.2023-034

Takahashi, T., 1978: Riming electrification as a charge generation mechanism in thunderstorms. *Journal of the Atmospheric Sciences*, 35(8), 1536–1548. https://doi.org/10.1175/1520-0469(1978)035<1536:reaacg>2.0.co;2

Takahashi, T., K. Suzuki, M. Orita, M. Tokuno, R. de la Mar, 1995: Videosonde observations of precipitation processes in equatorial cloud clusters. *Journal of the Meteorological Society of Japan*, 73, 509–534, https://doi.org/10.2151/JMSJ1965.73.2B_509.

Takahashi, T., S. Sugimoto, T. Kawano, K. Suzuki, 2019: Microphysical structure and lightning initiation in Hokuriku winter clouds. *Journal of Geophysical Research: Atmospheres*, 124, 13156–13181, https://doi.org/10.1029/2018JD030227.

Takahashi, T., Tajiri, T., Sonoi, Y., 1999: Charges on graupel and snow crystals and the electrical structure of winter thunderstorms. *Journal of the Atmospheric Sciences*, 56, 1561–1578. https://doi.org/10.1175/1520-0469(1999)056%3C1561:COGASC%3E2.0.CO;2

Takayama, H., Niino, H., Watanabe, S., Sugaya, J., Studies, M. of T. A. P., 1997: Downbursts in the northwestern part of Saitama Prefecture on 8 September 1994. *Journal of the Meteorological Society of Japan*, 75(4), 885–905. https://doi.org/10.2151/JMSJ1965.75.4_885

Takemi, T., 2006: Impacts of moisture profile on the evolution and organization of midlatitude squall lines under various shear conditions. *Atmospheric Research*, 82(1–2), 37–54. https://doi.org/10.1016/J.ATMOSRES.2005.01.007

Tapiador, F. J., J. L. Sánchez, E. García-Ortega, 2019: Empirical values and assumptions in the microphysics of numerical models. *Atmospheric Research*, 215, 214–238, https://doi.org/10.1016/j.atmosres.2018.09.010.

Thompson, G., P. R. Field, R. M. Rasmussen, W. D. Hall, 2008: Explicit forecasts of winter precipitation using an improved bulk microphysics scheme. Part II: Implementation of a new snow parameterization. *Monthly Weather Review*, 136, 5095–5115, https://doi.org/10.1175/2008MWR2387.1.

Tomita, H., 2008: New microphysical schemes with five and six categories by diagnostic generation of cloud ice. *Journal of the Meteorological Society of Japan*, 86A, 121–

142, https://doi.org/10.2151/jmsj.86A.121.

Tomita, H., H. Miura, S. Iga, T. Nasuno, M. Satoh, 2005: A global cloud-resolving simulation: Preliminary results from an aqua planet experiment. *Geophysical Research Letters*, 32, 1–4, https://doi.org/10.1029/2005GL022459.

Tomita, H., Satoh, M., 2004: A new dynamical framework of nonhydrostatic global model using the icosahedral grid. *Fluid Dynamics Research*, 34(6), 357–400. https://doi.org/10.1016/J.FLUIDDYN.2004.03.003/XML

Tsuchiya, K., T. Fujita, 1967: A Satellite Meteorological Study of Evaporation and Cloud Formation over the Western Pacific under the Influence of the Winter Monsoo. *Journal of the Meteorological Society of Japan*, 45, 232–250, https://doi.org/10.2151/JMSJ1965.45.3_232.

Ushio, T., Heckman, S. J., Christian, H. J., Kawasaki, Z.-I., 2003: Vertical development of lightning activity observed by the LDAR system: Lightning bubbles. *Journal of Applied Meteorology and Climatology*, 42(2), 165–174. https://doi.org/10.1175/1520-0450(2003)042

Vignon, N. Besic, N. Jullien, J. Gehring, A. Berne, 2019: Microphysics of Snowfall Over Coastal East Antarctica Simulated by Polar WRF and Observed by Radar. *Journal of Geophysical Research: Atmospheres*, 124, 11452–11476, https://doi.org/10.1029/2019JD031028.

Von Blohn, N., K. Diehl, S. K. Mitra, S. Borrmann, 2009: Riming of graupel: wind tunnel investigations of collection kernels and growth regimes. *Journal of the Atmospheric Sciences.*, 66, 2359–2366, https://doi.org/10.1175/2009JAS2969.1.

Wakimoto, R. M., 1985: Forecasting dry microburst activity over the High Plains.

Monthly Weather Review, 113, 1131–1143, https://doi.org/10.1175/1520-0493(1985)113<1131:FDMAOT>2.0.CO;2.

Wang, H., Easter, R. C., Rasch, P. J., Wang, M., Liu, X., Ghan, S. J., Qian, Y., Yoon, J.-H., Ma, P.-L., Vinoj, V., 2013: Sensitivity of remote aerosol distributions to representation of cloud–aerosol interactions in a global climate model. *Geoscientific Model Development*, 6(3), 765–782. https://doi.org/10.5194/GMD-6-765-2013

Watanabe, R., K. Suzuki, T. Kawano, S. Sugimoto, 2014: Microphysical structures of early-winter snow clouds during a cold air outbreak of December 23-25, 2010. *Scientific Online Letters on the Atmosphere*, 10, 62–66, https://doi.org/10.2151/SOLA.2014-013.

Waugh, S. M., C. L. Ziegler, D. R. MacGorman, S. E. Fredrickson, D. W. Kennedy, and W. David Rust, 2015: A Balloonborne Particle Size, Imaging, and Velocity Probe for in Situ Microphysical Measurements. *Journal of Atmospheric and Oceanic Technology*, 32, 1562–1580, https://doi.org/10.1175/JTECH-D-14-00216.1.

Weisman, M. L., Rotunno, R., 2004: "A theory for strong long-lived squall lines" revisited. *Journal of the Atmospheric Sciences*, 61(4), 361–382. https://doi.org/10.1175/1520-0469(2004)061

Wendisch, Manfred., Brenguier, J.-Louis., 2013: Airborne measurements for environmental research : methods and instruments. 689.

Williams, E., Boldi, B., Matlin, A., Weber, M., Hodanish, S., Sharp, D., 1999: The behavior of total lightning activity in severe Florida thunderstorms. *Atmospheric Research*, 51(3–4), 245–265. https://doi.org/10.1016/S0169-8095(99)00011-3

Wilson, D., K., 2001: An alternative function for the wind and temperature gradients in unstable surface layers. *Boundary-Layer Meteorology*, 99, 151–158, https://doi.org/10.1023/A:1018718707419.

Wilson, J. W., R. M. Wakimoto, 2001: The discovery of the downburst: T. T. Fujita's contribution. *Bulletin of the American Meteorological Society*, 82, 49–62, https://doi.org/10.1175/1520-0477(2001)082<0049:TDOTDT>2.3.CO;2.

Wilson, J.W., Roberts, R.D., Kessinger, C., McCarthy, J., 1984: Microburst Wind Structure and Evaluation of Doppler Radar for Airport Wind Shear Detection, *Journal of Climate and Applied Meteorology*. American Meteorological Society. https://doi.org/10.1175/1520-0450(1984)023<0898:MWSAEO>2.0.CO;2

Woods, C. P., M. T. Stoelinga, J. D. Locatelli, 2007: The IMPROVE-1 storm of 1-2 February 2001. Part III: Sensitivity of a mesoscale model simulation to the representation of snow particle types and testing of a bulk microphysical scheme with snow habit prediction. *Journal of the Atmospheric Sciences*, 64, 3927–3948, https://doi.org/10.1175/2007JAS2239.1.

Yamamoto, Y., K. Ichii, A. Higuchi, H. Takenaka, 2020: Geolocation accuracy assessment of himawari-8/AHI imagery for application to terrestrial monitoring. *Remote Sensing*, 12, 1372, https://doi.org/10.3390/RS12091372.

Yang, J., Zhang, Z., Wei, C., Lu, F., Guo, Q., 2017: Introducing the New Generation of Chinese Geostationary Weather Satellites, Fengyun-4. *Bulletin of the American Meteorological Society*, 98(8), 1637–1658. https://doi.org/10.1175/BAMS-D-16-0065.1

Yoshida, S., Wu, T., Ushio, T., Kusunoki, K., Nakamura, Y., 2014: Initial results of LF sensor network for lightning observation and characteristics of lightning emission in

LF band. *Journal of Geophysical Research: Atmospheres*, 119(21), 12,034-12,051. https://doi.org/10.1002/2014JD022065

Yoshimi, K., Wada, M., Hiraoka, Y., 2021: Study on Water Level Prediction Using Observational Data from a Multi-Parameter Phased Array Weather Radar. *Journal of Disaster Research*, 16(3), 410–414. https://doi.org/10.20965/JDR.2021.P0410

Zängl, G., Reinert, D., Rípodas, P., Baldauf, M., 2015: The ICON (ICOsahedral Non-hydrostatic) modelling framework of DWD and MPI-M: Description of the non-hydrostatic dynamical core. *Quarterly Journal of the Royal Meteorological Society*, 141(687), 563–579. https://doi.org/10.1002/QJ.2378

Zhang, D., Wang, Z., Liu, D., 2010: A global view of midlevel liquid-layer topped stratiform cloud distribution and phase partition from CALIPSO and CloudSat measurements. *Journal of Geophysical Research: Atmospheres*, 115, D00H13, https://doi.org/10.1029/2009JD012143

Zheng, D., Wang, D., Zhang, Y., Wu, T., Takagi, N., 2019: Charge Regions Indicated by LMA Lightning Flashes in Hokuriku's Winter Thunderstorms. *Journal of Geophysical Research: Atmospheres* 124, 7179–7206. https://doi.org/10.1029/2018JD030060